MICROCOPY RESOLUTION TEST CHART

NATIONAL BUREAU OF STANDARDS 1963 A

AD-A149 268

AFOSR-TR· ⠂ ⠂ 1 1 7 3

④

AMRC-R-614
Copy ⠄⠅⠂

ANNUAL REPORT: VIRTUAL CATHODE OSCILLATOR STUDY

November 1984

D. J. Sullivan
D. E. Voss
R. J. Adler
W. M. Bollen
R. H. Jackson
E. A. Coutsias*

Prepared for: Air Force Office of Scientific Research
                     Physics Directorate
                     Bolling Air Force Base, D.C. 20332

Under Contract   F49620-82-C-0014

Prepared by: MISSION RESEARCH CORPORATION
                     1720 Randolph Rd., SE
                     Albuquerque, NM 87106

DTIC FILE COPY

*University of New Mexico

84   12   1⠂   092

REPORT DOCUMENTATION PAGE	READ INSTRUCTIONS BEFORE COMPLETING FORM

1. REPORT NUMBER AFOSR-TR- 8 4 - 1 1 7 3	2. GOVT ACCESSION NO.	3. RECIPIENT'S CATALOG NUMBER

4. TITLE (and Subtitle) REPORT: VIRTUAL CATHODE OSCILLATOR STUDY	5. TYPE OF REPORT & PERIOD COVERED *Annual*
	6. PERFORMING ORG. REPORT NUMBER AMRC-R-614

7. AUTHOR(s) D. J. Sullivan (MRC) W. M. Bollen (MRC) D. E. Voss (MRC) R. H. Jackson (MRC) R. J. Adler (MRC) E. A. Coutsias (UNM)	8. CONTRACT OR GRANT NUMBER(s) F49620-82-C-0014

9. PERFORMING ORGANIZATION NAME AND ADDRESS Air Force Office of Scientific Research Bolling Air Force Base Washington, DC 20332	10. PROGRAM ELEMENT PROJECT TASK AREA & WORK UNIT NUMBERS 61102F 2301/A8

11. CONTROLLING OFFICE NAME AND ADDRESS MISSION RESEARCH CORPORATION 1720 Randolph Road, S.E. Albuquerque, New Mexico 87106	12. REPORT DATE November 1984
	13. NUMBER OF PAGES

14. MONITORING AGENCY NAME & ADDRESS(if different from Controlling Office)	15. SECURITY CLASS (of this report) UNCLASSIFIED
	15a. DECLASSIFICATION DOWNGRADING SCHEDULE

16. DISTRIBUTION STATEMENT (of this Report)

APPROVED FOR PUBLIC RELEASE; DISTRIBUTION UNLIMITED

17. DISTRIBUTION STATEMENT (of the abstract entered in Block 20, if different from Report)

18. SUPPLEMENTARY NOTES

19. KEY WORDS (Continue on reverse side if necessary and identify by block number)

Virtual Cathode	Space-Charge Limit
Virtual Anode	Space-Charge Limiting Current
Virtual Cathode Oscillator	Bifurcation
VIRCATOR	Millimeter Microwaves
	Spectrometer

20. ABSTRACT (Continue on reverse side if necessary and identify by block number)

The theory of a virtual cathode oscillator (VIRCATOR) has been pre-viously described (AMRC-R-451, 1983). It is found that second order analy-tical approximations give an accurate value for the space-charge limiting current of an electron beam in cylindrical geometry. The same Green's function approach could be used on other geometries as well. Exceeding the space-charge limiting current is the necessary condition for virtual elec-trode formation. However, it does not explain the nature of the (cont.)

DD FORM 1473 EDITION OF 1 NOV 65 IS OBSOLETE

space-charge limit instability. The oscillatory stable state of the virtual cathode is found to originate at the bifurcation point of several stable and unstable electron beam states. An analysis of the nonlinear growth rate of the instability is derived.

The virtual cathode is in effect a relaxation oscillator. The advantage of the vircator over a reflex klystron is that the virtual cathode moves opposite to the electron beam propagation direction during the bunching phase resulting in enhanced electron densitites unobtainable otherwise. The periodic time-dependent nature of the bunching results in efficient microwave generation. Experimental efficiencies of 12% have been obtained in previous work and theoretical efficiencies of 20% have been obtained in the work described here. The microwave frequency scales as the relativistic beam plasma frequency. This can be adjusted via an externally applied axial magnetic field. The result is an oscillator which is frequency agile over an order of magnitude without externally changing the physical configuration. Output powers of from kilowatts to gigawatts are obtainable based on the power source. Experimental results are reviewed and explained. The rationale for using a foilless diode as the electron beam source is given.

A detailed mechanical and electrical design has been presented in previous reports (AMRC-R-451, 1983). It entails placing the vircator in a high vacuum vessel with flexibility for further development. The electrical power is pulse formed using a lumped artificial Blumlein line. The axial magnetic field is critically damped for component safety and circuit design simplicity. The beam source is a foilless diode with an annular limiter for collimation and prevention of electrons reflexing into the diode.

Several important technical developments have come to a successful conclusion during the period of work covered by this report. The multi-Tesla magnetic field coil, critically important for achieving the high electron densities necessary for driving millimeter wavelenghts, has been designed, and successfully tested. Secondly, a millimeter wavelength spectrometer, necessary for diagnosing the time history and spectral content of the vircator emission, has been designed and calibrated over a wide band from 35 to 110 GHz. Measured frequency selectivity was typically of order 5% or better, i.e., $\Delta f/f_0 \leq .05$. A unique cathode material has been investigated, yielding fast field-emission turn on and low gap closure rates. Details of these results are presented in the main section of this report.

ACKNOWLEDGEMENT

TABLE OF CONTENTS

LIST OF ILLUSTRATIONS

LIST OF ILLUSTRATIONS (continued)

LIST OF ILLUSTRATIONS (continued)

4

LIST OF ILLUSTRATIONS (continued)

LIST OF PHOTOGRAPHS

LIST OF TABLES

SECTION I
INTRODUCTION

The main thrust of research in the second year of this program has
been experimental. This report summarizes the progress made in developing
the hardware for a millimeter wavelength virtual cathode microwave oscil-
lator (Vircator). Fabrication, testing, and calibration of two critical
components, the solenoidal magnet and the millimeter microwave spectrom-
eter, is complete. Data summary and complete documentation of the testing
of the magnetic field coil at the 30 kG level, is presented in Section II.
Calibration data for the spectrometer, covering the entire 35 to 100 GHz
frequency range, is presented in Section III. Section IV describes the
successful operation of the electron beam pulse power system, based on an
artificial Blumlein design. A unique cathode material is described which
allows fast turn on of electron field emission, at field strengths of
approximately 50 kV/cm and very slow anode-cathode gap closure rates, less
than 1 cm/μsec. Our work in this area is further supplemented by reprints
of articles compiled in Appendix B.

SECTION II
MAGNET DESIGN

The main criteria for the vircator magnet design are:

(1) Peak magnetic field of 60 kG;

(2) Field homogeneity in the anode-cathode gap region of $\Delta B/B < 1\%$.

(3) Accessibility to the high magnetic field region for grids, elec-
trodes, diagnostics, and their connecting cables and mechanical
support structure.

In support of the vircator magnet design, a useful computational tool
has been developed for calculating the field line configuration for
arbitrary solenoidal geometries. The computer code uses a two step
process. Radial and axial components of the magnetic field are calculated
on a two dimensional rectangular grid by summing the weighted contribution
from each circular current loop making up the solenoid. Bilinear
interpolation is then used to follow field line trajectories which are
launched from the center of the solenoid.

The magnetic field for an arbitrary solenoidal configuration follows
from the weighted superposition of the fields from the elemental circular
current loops, with the neglect of helicity and finite-current cross-
section effects. Eddy current effects are also neglected; this is a good
assumption since the skin penetration time through the high resistance
stainless steel casing, approximately 10 microseconds, is small relative to
the 570 microsecond field rise-time. With these approximations, the radial
and axial components of the magnetic field, B_r and B_z, at an arbitrary
point r,z, due to a circular current loop of radius a centered at the
origin of a cylindrical coordinate system (see Figure 1) can be calculated
(in mks units) as[1]:
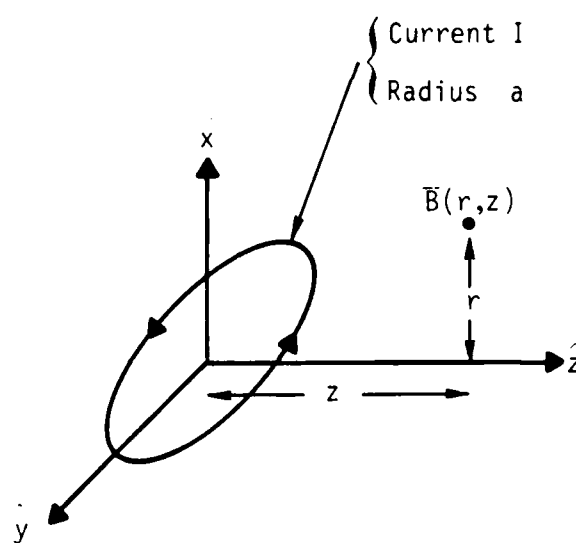
Figure 1. Relation of the cylindrical co-ordinate system to the
circular current loop. The center of the loop and the
origin of co-ordinates are coincident, and the z axis
and the normal to the loop are coincident.

11

$$B_r = \frac{\mu_0 I}{2\pi} \frac{z}{r\left[(a+r)^2 + z^2\right]^{1/2}} \left[-K(k) + \frac{a^2 + r^2 + z^2}{(a-r)^2 + z^2} E(k)\right] \quad , \quad (1)$$

$$B_z = \frac{\mu_0 I}{2\pi} \frac{1}{\left[(a+r)^2 + z^2\right]^{1/2}} \left[K(k) + \frac{a^2 - r^2 - z^2}{(a-r)^2 + z^2} E(k)\right] \quad , \quad (2)$$

where

$$k^2 \equiv 4 \, ar \Big/ \left[(a+r)^2 + z^2\right] \quad\quad (3)$$

and $K(k)$ and $E(k)$ are the complete elliptic integrals of the first and second kind, respectively. It is straightforward to evaluate the elliptic integrals numerically, and sum over the windings of the solenoid to produce a B_r and B_z matrix representing the calculated magnetic field. The first part of the field line plotting carries out these calculations, and is based on a code provided by John Freeman of Sandia National Laboratories.[2] Run time is approximately 30 seconds on a VAX 11/780 for an 84 point (12x7) grid and a 156 turn solenoid.

Field line plots are produced from the $\overline{B}$ field matrix using a shooting technique. Field lines are launched from the center of the solenoid in the $\hat{x}$-$\hat{y}$ plane, nominally a uniform field region, and the trajectory incremented by step sizes which are small relative to the $\overline{B}$ field grid points. Bilinear interpolation allows calculation of B_r and B_z between grid points with second order accuracy.[3]

In order to verify accurate operation of the code, a cross check has been carried out with an analytical calculation of a field line trajectory near the magnet center. The magnetic field in the central zone of a uniform current density, cylindrically symmetric solenoid can be written as a power series with terms of the form

12

$$\left(r^2 + z^2\right)^n P_{2n} (\cos \theta) \quad , \tag{4}$$

with P_{2n} the even Legendre ploynominals.[4-7] To second order, the $\overline{B}$ field is:

$$B_z = B_0 \left[1 + E_2 \left(\frac{\rho}{a}\right)^2 \; \frac{1}{2} \; \left(3u^2 - 1\right)\right] \tag{5}$$

$$B_r = B_0 \left[\frac{-E_2}{3} \; \left(\frac{\rho}{a}\right)^2 \; 3 \, u \, u'\right] \tag{6}$$

where

$$u \equiv \frac{z}{\sqrt{r^2 + z^2}} \tag{7}$$

$$u' \equiv \frac{r}{\sqrt{r^2 + z^2}} \tag{8}$$

$$\rho^2 \equiv r^2 + z^2 \tag{9}$$

$$E_2 = \frac{1}{2\beta^2} \; \frac{C_1^{\frac{3}{2}} - C_3^{\frac{3}{2}}}{\ln\left[\dfrac{\alpha + \sqrt{\alpha^2 + \beta^2}}{1 + \sqrt{1 + \beta^2}}\right]} \tag{10a}$$

$$\approx -\frac{3}{2} \; \frac{1}{\beta^4} \qquad \text{for} \quad \alpha - 1 \ll 1 \tag{10b}$$

13

$$C_1 \equiv \frac{1}{1 + \beta^2} \tag{11}$$

$$C_3 \equiv \frac{\alpha^2}{\alpha^2 + \beta^2} \tag{12}$$

$$\alpha \equiv \frac{\text{solenoid outer radius}}{\text{solenoid inner radius}} \tag{13}$$

$$\beta \equiv \frac{1}{2} \frac{\text{solenoid length}}{\text{solenoid inner radius}} \tag{14}$$

$$B_0 = J_0 a \; \frac{4\pi\beta}{10} \; \ln\left\{ \frac{\alpha + \sqrt{\alpha^2 + \beta^2}}{1 + \sqrt{1 + \beta^2}} \right\} \tag{15}$$

where J_0, the average solenoid current density, has units of amps/cm^2, magnet radius a is in cm, and B_0 is in gauss. The equation defining the field line trajectory in two-dimensional space can be written:

$$\frac{dr}{B_r} = \frac{dz}{B_z} \; . \tag{16}$$

Keeping only the first term in the $\overline{B}$ field expansion and integrating the resulting differential equation gives the equation for the field line trajectories near the center of solenoid:

$$r = r_0 \; e^{-E_2 z^2 / 2a^2} \tag{17}$$

For the case of a 10 cm radius, 100 cm long solenoid wound with a single 251 turn layer ($\alpha = 1$, $\beta = 5$, $E_2 = -0.0024$), the code calculation shows that a field line launched from $(r,z) = (0.90000, 0)$ cm intersects a point

(0.90095, 9.375) cm. Taking $r_0 = 0.9$ in Equation (17) yields $(r,z) = (0.9009497, 9.375$ cm), which agrees with the numerical calculation to within a fraction of one percent. In addition, the $\overline{B}$ field intensity at the center of the magnet for 1 amp current is calculated numerically as 3.081 Gauss, in excellent agreement with an analytical calculation[8] yielding 3.0806 G for this geometry. These cross-checks indicate that both the $\overline{B}$ field and the field line trajectory calculations are working correctly for the case of interest, i.e., near the center of a long solenoid.

The magnetic field code has been the primary tool used in design of the vircator magnet. End windings were used to yield a homogeneous central field. Optimization was carried out by iterating on a base design using the interactive capabilities of the VAX 11/780. A listing of the FORTRAN source code is given in Appendix A. Table I summarizes the final magnet design parameters, and Table II gives the radial and axial magnetic field components over a central region 3 cm in diameter and 8 cm long. Homogeneity in this region is $\Delta B/B_0 \le 0.008$, $B_r/B_0 \le 0.007$, with B_0 the field at the center of the magnet.

The magnet overall length is 21.4 cm with a usable inside diameter of 4.6 cm. The magnet is wound with 156 turns of 1 mm diameter wire in 5 layers, yielding an inductance of 0.7 mH and a current of 5.7 kA for the full 60 kG field. Self-forces tending to squeeze the magnet axially are taken up by the copper windings and an epoxy binder. Radial expansion forces are taken up by an encapsulating cylindrical stainless steel tube and the epoxy binder. With the assumption that half the radial expansion forces are borne by the epoxy and half by the encapsulating stainless steel, the stress in the 1.9 mm thick, 11.4 cm O.D. stainless shell is 23,100 psi for a 60 kG field. Since the yield strength of type 304 stainless steel exceeds 40,000 psi, the design provides an acceptable safety factor.

TABLE I. VIRCATOR MAGNET CONFIGURATION

Shell Number	Conductor Radius (cm)	Conductor Axial Coordinate Range (cm)	Number of Windings Distributed in Shell	Description
1	2.80	-7.41 to -4.94	7	Inner end-correction winding, left side.
2	2.80	+4.94 to +7.41	7	Inner end-correction winding, right side.
3	3.27	-7.41 to -0.41	17	Outer end-correction, left side.
4	3.27	+0.41 to +7.41	17	Outer end-correction, right side.
5	3.73	-7.41 to +7.41	36	Main winding.
6	4.20	-7.41 to +7.41	36	Main winding.
7	4.66	-7.41 to +7.41	36	Main winding.

Design Magnetic Field .... 60 kG

Total Number of Turns 156

Drive Current for 60 kG Field at Center .... 5.7 kA

Magnet Inductance .... 0.7 mH

Field Energy at Full Current .... 11.4 kJ

TABLE II. MAGNET COMPUTATION REGION DATA

```
RADIUS=    1.500E+00     LENGTH=    4.000E+00    DR=    5.000E-01
     DZ=   1.000E+00     NR=  4     NZ=  5
```

COIL DATA

R= 2.80E+00	ZL=-7.41E+00	ZR=-4.94E+00	TURNS= 7.00E+00	CURRENT= 5.71E+03
R= 2.80E+00	ZL= 4.94E+00	ZR= 7.41E+00	TURNS= 7.00E+0u	CURRENT= 5.71E+03
R= 3.27E+00	ZL=-7.41E+00	ZR=-4.12E-01	TURNS= 1.70E+01	CURRENT= 5.71E+03
R= 3.27E+00	ZL= 4.12E-01	ZR= 7.41E+00	TURNS= 1.70E+01	CURRENT= 5.71E+03
R= 3.73E+00	ZL=-7.41E+00	ZR= 7.41E+00	TURNS= 3.60E+01	CURRENT= 5.71E+03
R= 4.20E+00	ZL=-7.41E+00	ZR= 7.41E+00	TURNS= 3.60E+01	CURRENT= 5.71E+03
R= 4.66E+00	ZL=-7.41E+00	ZR= 7.41E+00	TURNS= 3.60E+01	CURRENT= 5.71E+03

RADIAL MESH LINE LOCATIONS
```
0.00000E+00   5.00000E-01   1.00000E+00   1.50000E+00
```

AXIAL MESH LINE LOCATIONS
```
0.00000E+00   1.00000E+00   2.00000E+00   3.00000E+00   4.00000E+00
```

$\text{THETA} = \text{ARCTAN}(BR/BZ)$ (degrees)

LISTING OF BR AND BZ OVER THE COMPUTATIONAL GRID

K	L	R	Z	BR(K,L)	BZ(K,L)	B(K,L)	BR/BZ	THETA
1	1	0.00000	0.0000	0.000	60000.031	60000.031	0.000E+00	0.0000
1	2	0.00000	1.0000	0.000	60017.418	60017.418	0.000E+00	0.0000
1	3	0.00000	2.0000	0.000	59966.418	59966.418	0.000E+00	0.0000
1	4	0.00000	3.0000	0.000	59726.496	59726.496	0.000E+00	0.0000
1	5	0.00000	4.0000	0.000	59156.402	59156.402	0.000E+00	0.0000

K	L	R	Z	BR(K,L)	BZ(K,L)	B(K,L)	BR/BZ	THETA
2	1	0.50000	0.0000	0.000	59995.840	59995.840	6.835E-10	0.0000
2	2	0.50000	1.0000	-4.416	60021.887	60021.887	-7.357E-05	-0.0042
2	3	0.50000	2.0000	33.265	59978.754	59978.762	5.546E-04	0.0318
2	4	0.50000	3.0000	87.598	59743.328	59743.391	1.466E-03	0.0840
2	5	0.50000	4.0000	214.361	59216.949	59217.336	3.620E-03	0.2074

K	L	R	Z	BR(K,L)	BZ(K,L)	B(K,L)	BR/BZ	THETA
3	1	1.00000	0.0000	0.001	59978.680	59978.680	1.345E-08	0.0000
3	2	1.00000	1.0000	-18.919	60036.184	60036.184	-3.151E-04	-0.0181
3	3	1.00000	2.0000	65.006	60017.195	60017.230	1.083E-03	0.0621
3	4	1.00000	3.0000	166.902	59787.082	59787.316	2.792E-03	0.1599
3	5	1.00000	4.0000	365.696	59381.059	59382.184	6.158E-03	0.3528

K	L	R	Z	BR(K,L)	BZ(K,L)	B(K,L)	BR/BZ	THETA
4	1	1.50000	0.0000	0.000	59929.898	59929.898	4.424E-09	0.0000
4	2	1.50000	1.0000	-58.797	60064.949	60064.977	-9.789E-04	-0.0561
4	3	1.50000	2.0000	96.956	60087.793	60087.871	1.614E-03	0.0925
4	4	1.50000	3.0000	241.009	59839.746	59840.230	4.028E-03	0.2308
4	5	1.50000	4.0000	391.128	59583.676	59584.961	6.564E-03	0.3761

Encapsulation of the magnet is completed by a 1.6 mm thick inner wall and two 1.6 mm thick end plates. The stainless shell and its relation to the coil windings is shown in Figure 2. The inner stainless cylinder acts to shield the magnet winding from electron and x-ray bombardment which would otherwise reduce the magnet turn-to-turn voltage standoff. Since the highest operating voltage for the vircator is 100 kV, the inner stainless shield provides complete shielding from electron bombardment (50 electron ranges at 100 kV) and better than a factor of 10 attenuation (2.4 mean free paths for 50 kV x-rays) for the most energetic x-rays of interest. Flux penetration constraints do not allow the wall thickness to be substantially increased beyond 2 mm, corresponding to a magnetic field penetration time of approximately 10 microseconds.

Fabrication prints for the stainless steel magnet housing are shown in Figures 3-5. Fabrication prints for the PVC insulators are shown in Figures 6-9, and the assembled magnet is shown in Photo 1. The purpose of the insulator assembly is to provide high voltage standoff between the multi-kV magnet windings and the grounded stainless steel magnet housing. PVC wall thickness is 5.7 mm on the outer wall and 24.9 mm on the side walls, providing voltage standoff to well above the 10 kV required. No PVC is required at the inner radius since the inner-most magnetic winding is relatively close to ground potential.

The cylindrical magnet is held in place by encapsulation between the upper and lower PVC brackets shown in Figure 10. Brackets attach to the upper plate of Figure 11 which is positioned with respect to the lower plate of Figures 12 and 13 by 3 bolts. These bolts provide 3 degrees of freedom for aligning the magnet with the cathode. An additional two degrees of freedom is allowed by positioning the lower plate of Figure 12 relative to the stainless steel mounting brackets which are welded inside the vacuum vessel; both of these pieces have racetrack-type slots for adjustment. Thus, full 5 degree-of-freedom flexibility is allowed by the magnet alignment system. Photo 2 shows the vircator magnet and the assembled alignment system.

18
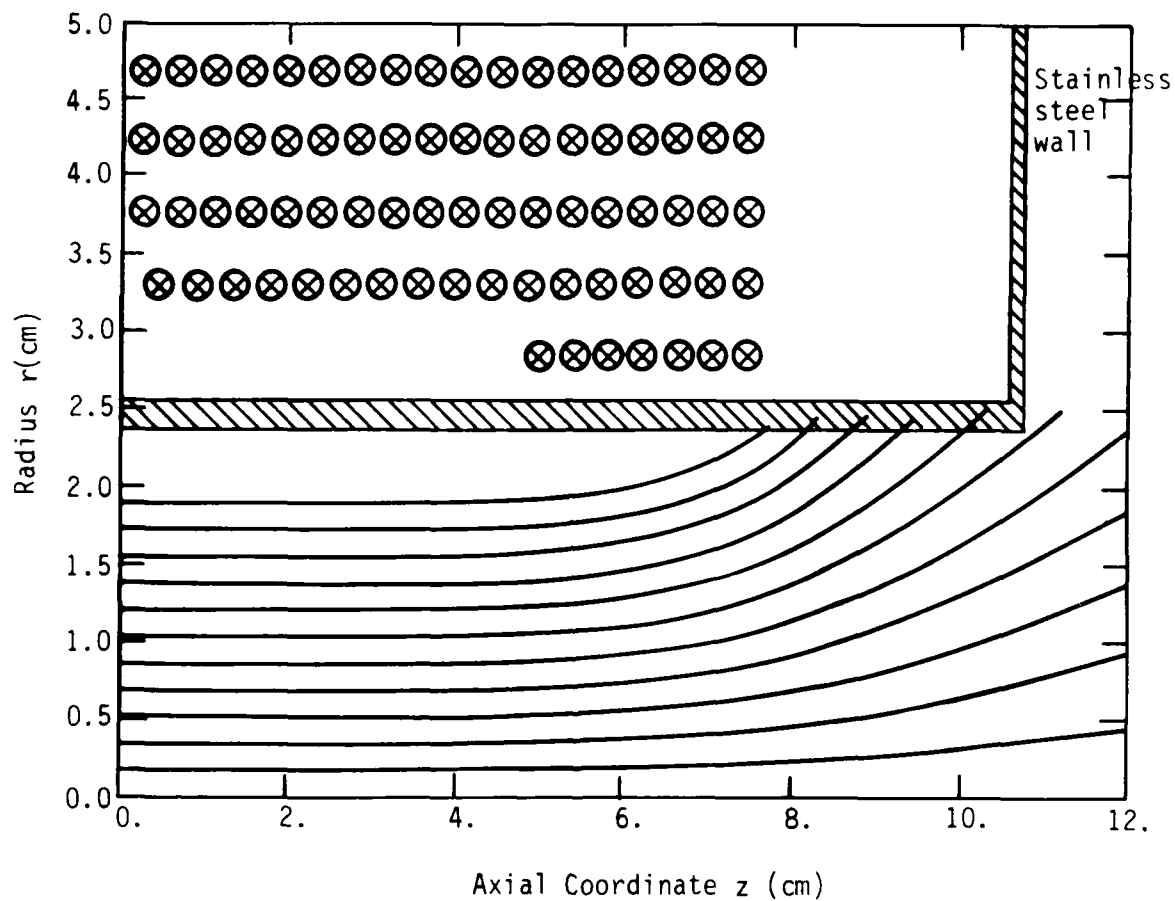
Figure 2. Relationship between the stainless steel encapsulating shell and the coil windings. Usable inside diameter of the magnet is 4.6 cm. The calculated magnetic field lines are shown as solid lines and each winding for the right side is shown as an x.

STAINLESS STEEL PIPE

Drill and tap eight (8) #2-56 thru holes, equally spaced

Drill and tap eight (8) #2-56 thru holes, equally spaced

.251 Radius

.722

.503

.200

8.020

8.420

$22\frac{1}{2}$

4.500 OD

4.351 ID

(Turn ID so that PVC tube is a snug fit in ID)
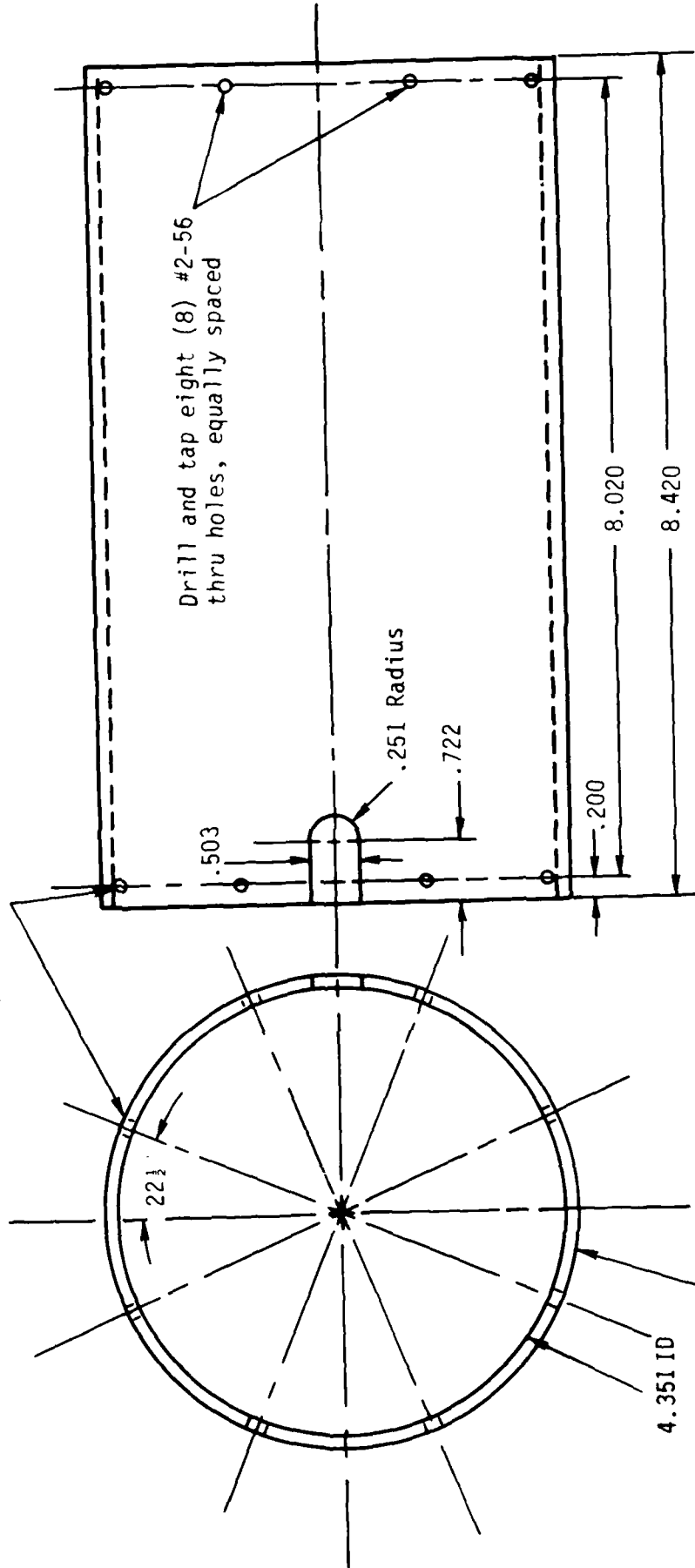
Material: 300 series stainless steel tube (not provided)

Quantity: One (1)

Figure 3. Fabrication print of the magnet outer shell used to take up the radial stresses induced by the 60 kG magnetic field.

20

INNER PIPE

Drill and tap eight (8) #2-56 thru holes at each end, equally spaced.

8.020

8.620

.400

2.000 OD
Tube (provided)

45

1.870 ID

Material: 300 series stainless (provided)
Quantity: One (1)
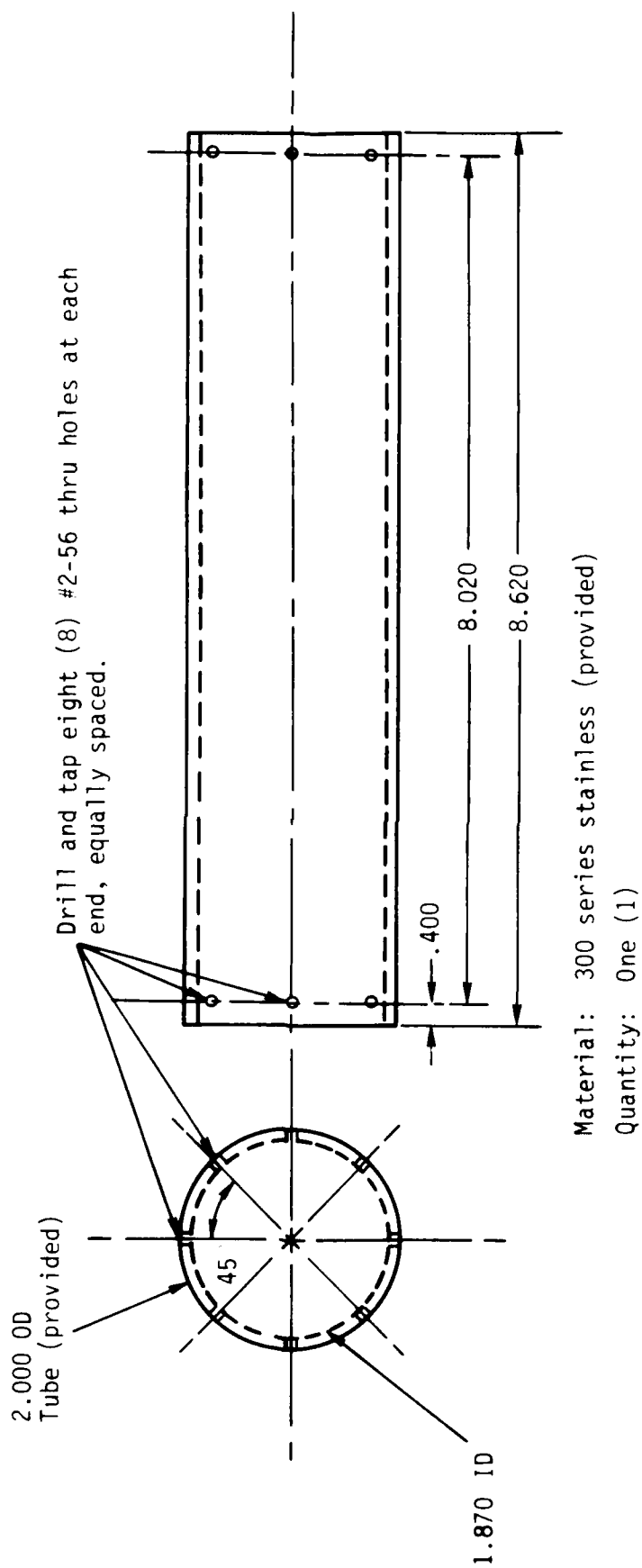
Figure 4. Fabrication print of the magnet inner shell used to reduce electron and photon bombardment of the inner windings.

21

.065

ENDPIECE #4

Drill thru hole .550 ID

.065 Thick

1.600

2.001 ID (Adjust ID to be snug fit on the 2" OD Stainless inner pipe.)

4.350 (Adjust OD to be snug fit in 4.50" OD Stainless Steel pipe.)

ENDPIECE #3

Material: 300 Series Stainless (not provided)
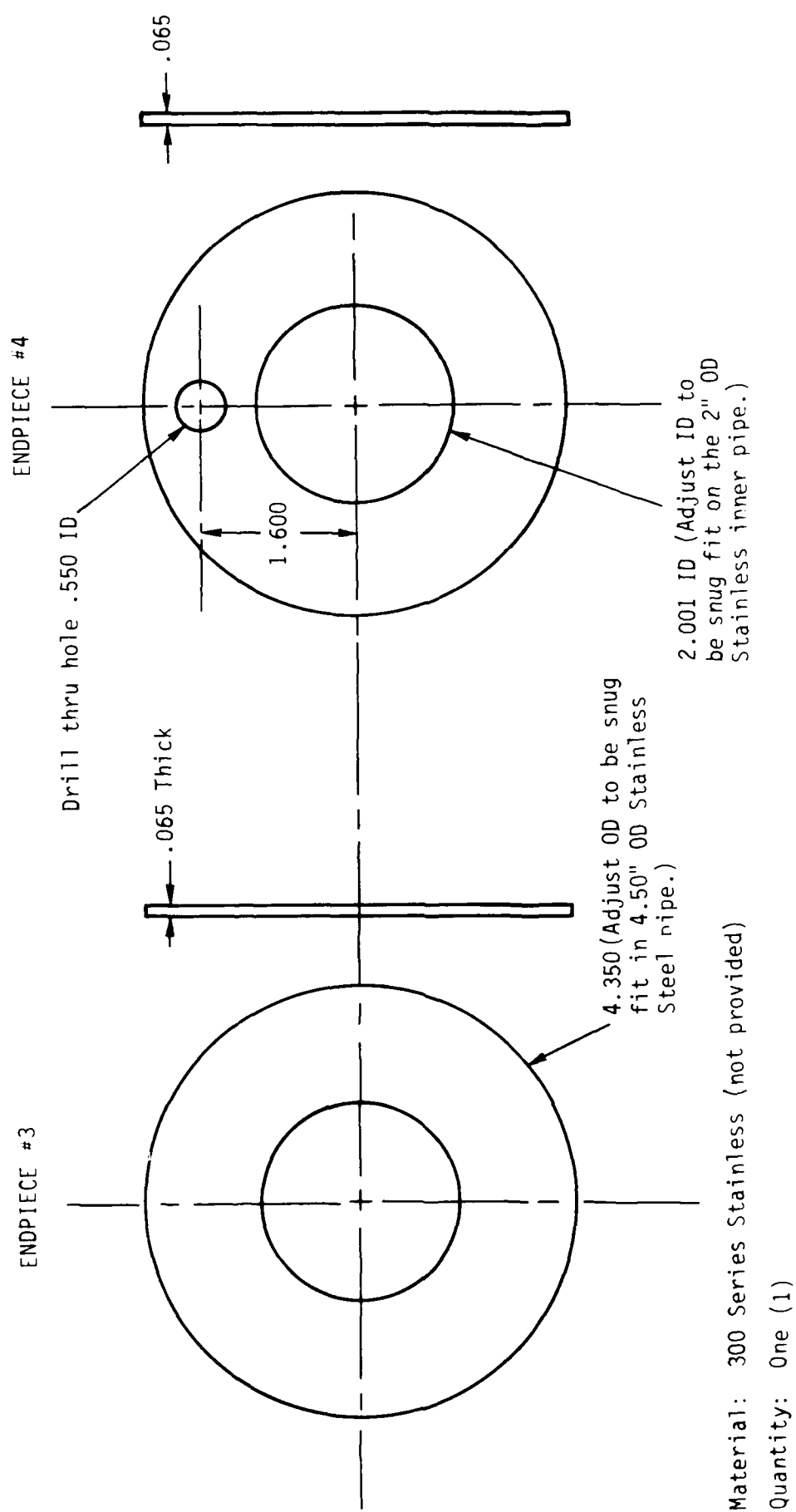
Quantity: One (1)

Figure 5. Fabrication print of the magnet end caps.

22

PVC PIPE

7.957

.251 Radius

.492

.503
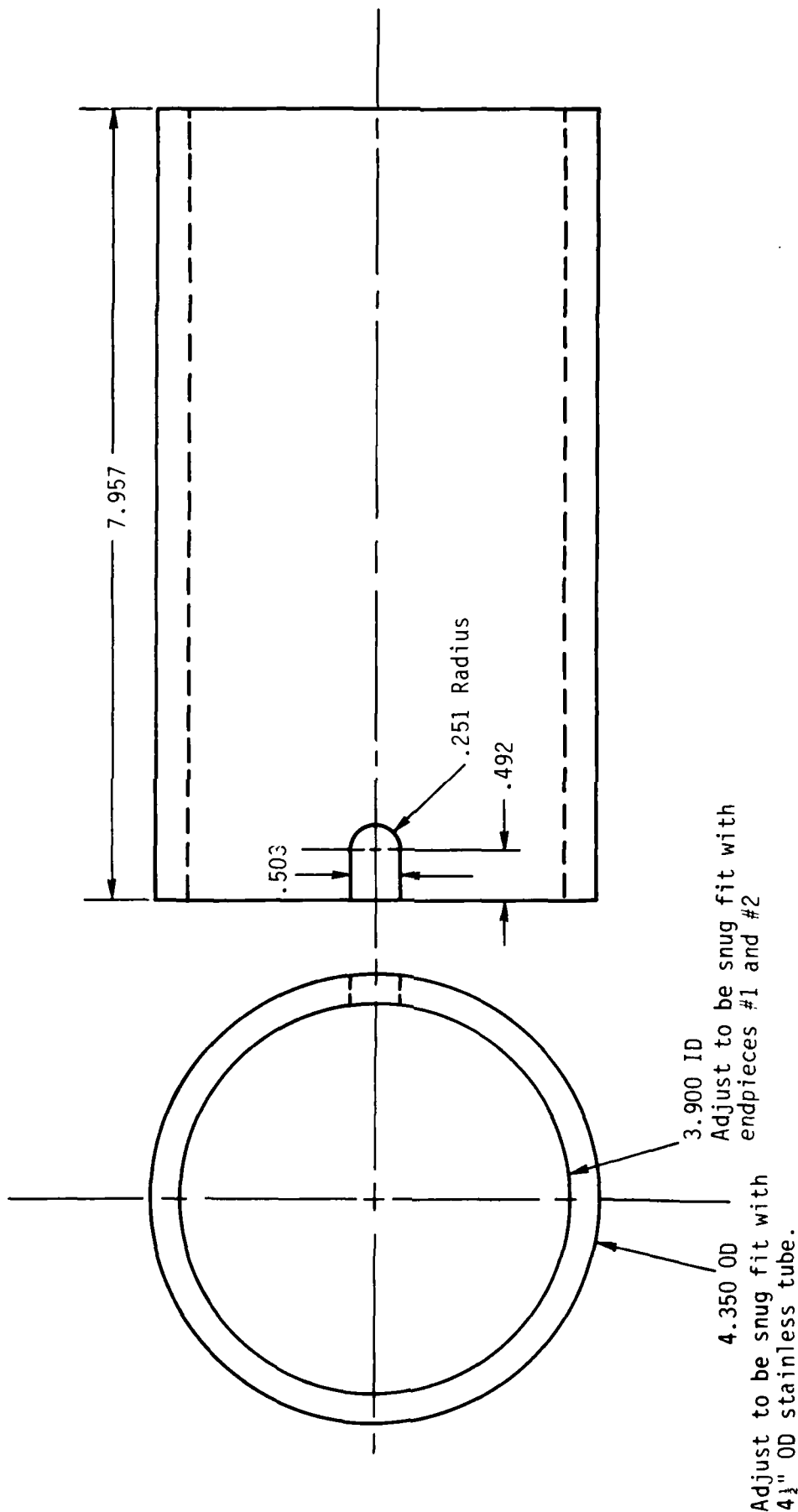
3.900 ID
Adjust to be snug fit with
endpieces #1 and #2

4.350 OD

Adjust to be snug fit with
4½" OD stainless tube.

Material: PVC Plastic (provided)
Quanity: One (1)

Figure 6. Fabrication print of the outer PVC shell used to insulate the high
voltage outer magnet windings from the grounded case.

PLUG #1

.498 OD
(Snug fit to hole in endpiece #1)

.175 ID

2.600

Material: DuPont Vespel (provided)
Quantity: One (1)

ENDPIECE #1

Drill thru hole, .500 ID

.085 Radius

.980

.490

.170

2.050 ID

3.898 OD
(Snug fit to 4.350 OD PVC Pipe)

Material: PVC plastic (provided)
Quantity: One (1)
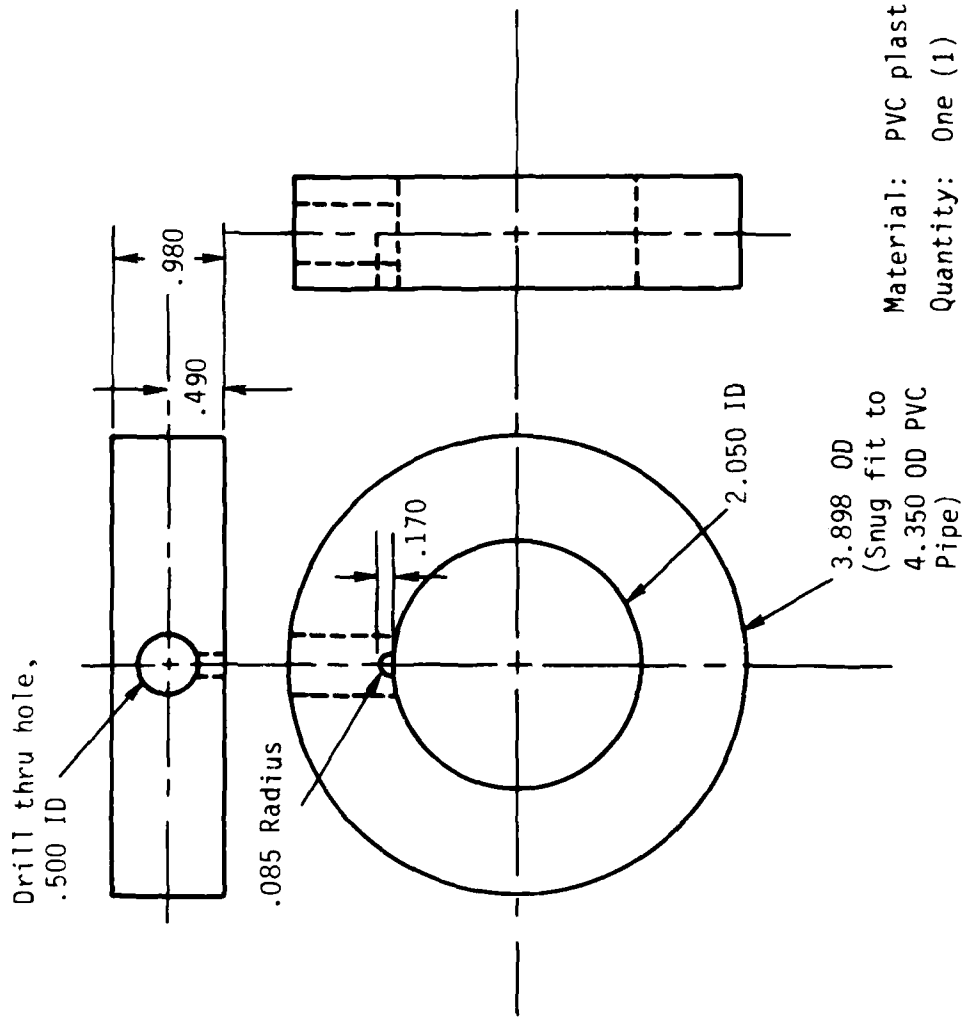
Note: Critical dimension is OD - adjust so that it is a snug fit in ID of 4.350 OD PVC pipe
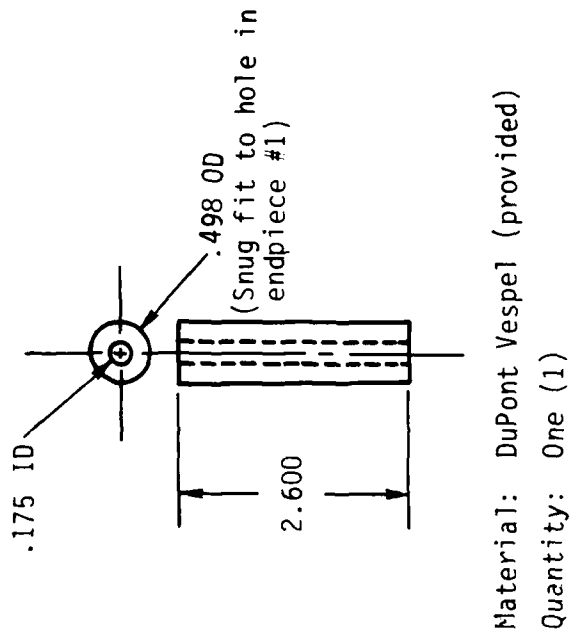
Figure 7. Fabrication print of the left PVC endcap and the polyimide insulated feedthrough used to feed the inner windings of the magnet.

24

PLUG #2

.498 OD
(Snug fit to hole in
endpiece #2)

.175 ID

2.600

Material: DuPont Vespel (provided)
Quantity: One (1)

ENDPIECE #2

Drill thru hole, .500 ID

.980

3.898 OD

2.050 ID

1.600

(Snug fit to 4.35 OD PVC Pipe)

Material: PVC Plastic (provided)
Quantity: One (1)
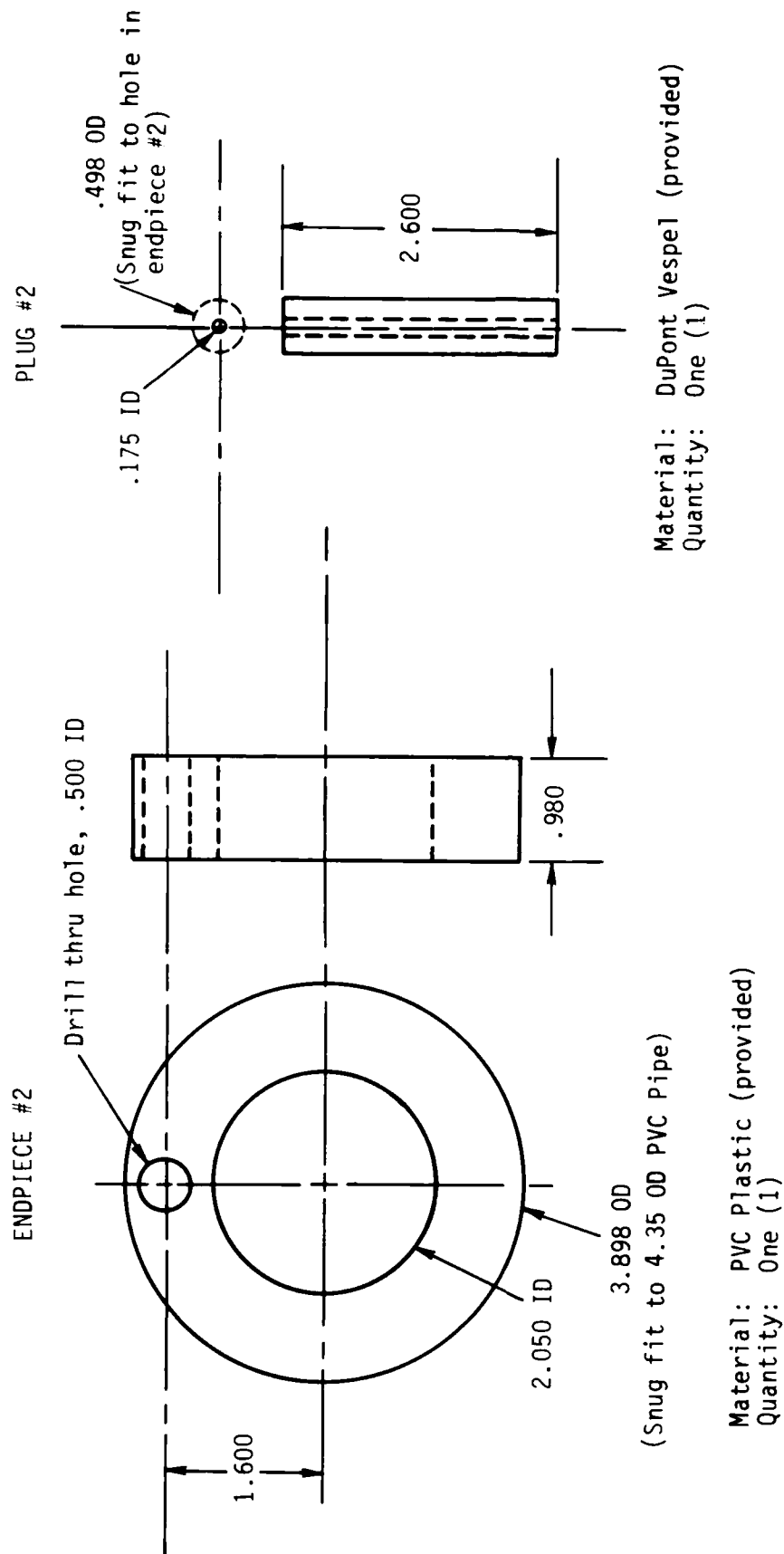
Note: Critical dimension is OD-adjust so that it is
a snug fit in ID of the 4.350 OD PVC pipe.

Figure 8. Fabrication print of the right PVC endcap and the polyimide insulated
feedthrough used to feed the outer windings of the magnet.

SPACER

.164 Slot Width

3.730

2.360
2.050
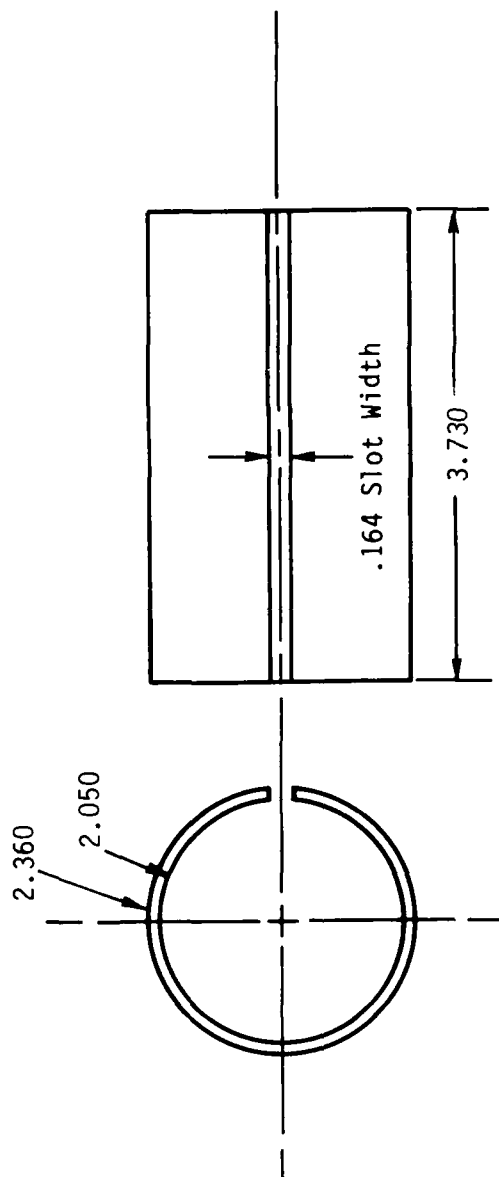
Material: PVC plastic (provided)
Quantity: One (1)

Figure 9. Fabrication print of the PVC spacer separating the left and right inner correction windings.

26
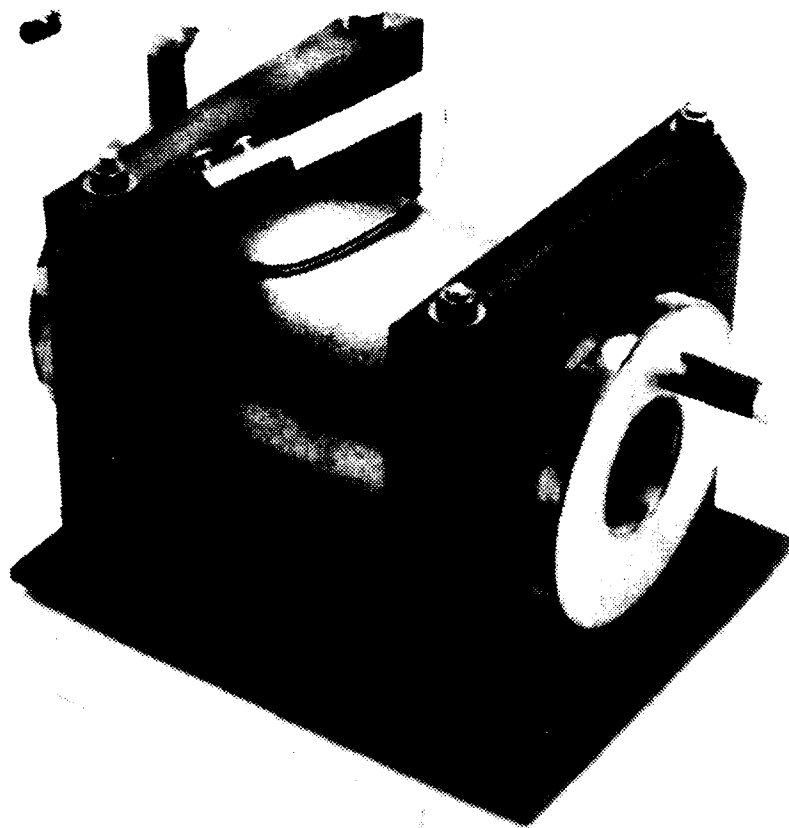
Photograph 1.   Vircator magnet assembly. The cylindrical magnet housing
                is attached to the PVC baseplate with four stainless steel rods.

27

UPPER BRACKET

0.020

2.251 Radius

3.500
2.800

3.500
2.800

3.300

1.000 .500

Drill two (2) thru holes, of diameter .248
These should line up with the holes in the
lower bracket so that 1/4" rod can be
inserted through the two pieces.

Material: PVC Plastic (provided)
Quantity: Two (2)

LOWER BRACKET

3.300
1.000
.500

.020

2.900 1.000

Drill two (2) Through holes,
.248 diameter, to mate with
holes in upper bracket and
upper plate.

3.500
2.800
2.000

1.000
1.000

3.500
2.800
2.000

2.251 Radius

1/2"

3/4"

Drill and tap two (2) 1/4" holes,
1/2" deep, as shown. These mate
with holes in upper plate.

Drill and tap two (2) 1/4" holes,
3/4" deep. These should mate with
holes in upper plate.

Material: PVC Plastic (provided)
Quantity: Two (2)

Figure 10. Fabrication prints for the magnet brackets. The cylindrical magnet is
encapsulated between the two brackets and attached to the upper plate
of Figure 11.

UPPER PLATE
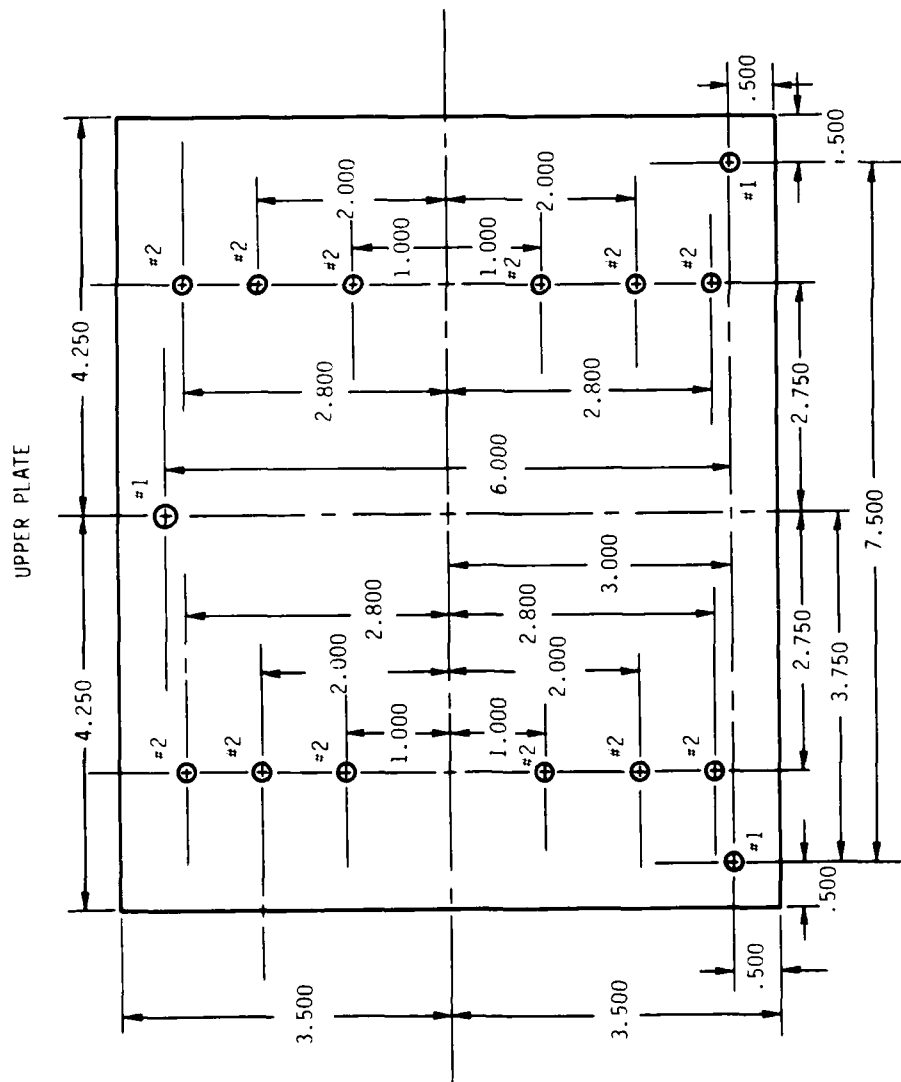
Material: 1/4" thick PVC (provided)
Quantity: One (1)

Drill a total of 15 through holes, according to the number of each as follows:

#1: Diameter of these three holes is .285. These three holes should be accurately located relative to each other, as the dimensions indicate.

#2: Diameter of these 12 holes is .250. These holes should accurately line up with the holes drilled and tapped in the lower bracket pieces. They should accept a 1/4" hex head bolt (provided).

4.250

4.250

2.000

2.000

1.000

1.000

2.800

2.800

6.000

3.000

2.800

2.800

2.000

2.000

1.000

1.000

2.750

2.750

7.500

3.750

.500

.500

.500

.500

3.500

3.500

.500

.500

Figure 11. Fabrication print of the PVC upper plate which provides a rigid mount for the magnet.

29

LOWER PLATE

Material: 1/4" thick
PVC (provided)

Quantity: One (1)

Drill three (3) thru holes,
.248 diameter at positions
shown. These should line up
accurately with the holes in
the upper plate piece.

Mill eight (8) slots in position shown,
all are same shape. Slot size is .265
wide by 1.50 long. Top slots are in
same position as bottom slots, relative
to center line.

Drill six (6) thru
holes, diameter .250,
at positions shown

3.70

3.75

1.80

1.80

3.75

1.80

6.000

3.000

11.60

3.750

1.500

1.500

7.500

4.650

.265

1.50

3.75

1.80

3.75

Figure 12.   Fabrication print of the lower plate. Bolts are inserted through the three
0.248 inch diameter holes to provide 3 point alignment of the magnet with
the cathode.

30

STIFFENER for LOWER PLATE

1.50
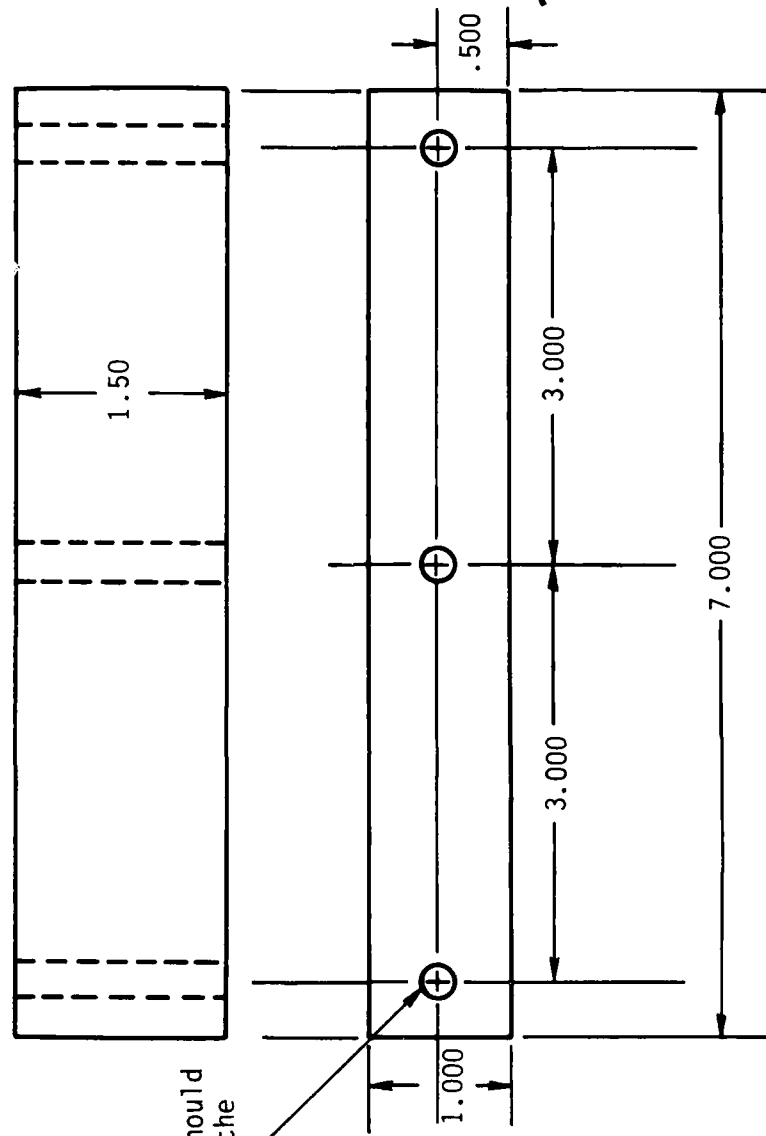
Drill three (3) holes,
.250 diameter. These should
mate with the holes in the
lower plate piece.

.500

3.000

7.000

3.000

1.000

Material: PVC plastic
Quantity: Two (2) required

Figure 13. Fabrication print of the PVC pieces used to
stiffen the lower plate structure.

31

Photograph of the vircator magnet and the five degree-of-freedom positioning assembly for aligning the magnet with the high voltage cathode.

A schematic for the circuit which drives the magnetic field coil is shown in Figure 14. A 366 microfarad energy storage capacitor bank is discharged into the magnetic field coil through a series resistance which is chosen so that the circuit is strongly, but not critically, damped. Since the current reversal is slight, the lifetime of both the capacitors and the magnetic field coil are increased. The price paid is an increase by a factor of approximately 2 in the required bank capacitance relative to an undamped circuit. The same result could be achieved by crowbaring the current at peak field with an ignitron, and eliminating the series resistance. Since the cost of the increased capacitance is small compared to the cost of the ignitron and its driving and control circuits, the former option was chosen.

The magnet energizing circuit of Figure 14 operates as follows. A 20 kV, 10 mA power supply (Del Electronics #RIU-20-10) charges the 366 microfarad capacitor bank to its charge voltage, about 8 kV for a 30 kilogauss field. A krytron gas tube switch is command triggered to discharge a 1 microfarad capacitor charged to 2.5 kV into the ignitor terminals of a mercury ignitron (General Electric #GL-7703). The triggered ignitron then discharges the main capacitor bank into the inductive load through a 1.8 ohm series resistor. The peak magnetic field occurs at 570 microseconds. A time delay generator (California Avionics #113CR) command fires the spark gap to initiate the electron beam at peak magnetic field time.

Testing of the vircator magnet has been carried out to the 30 kG level using two 183 μF, 8 kV rated capacitors configured in parallel as the energy source. No attempt has been made to exceed this field level, although design calculations indicate reliable operation to 60 kG. Time dependence of the magnetic field has been measured with the probe assembly shown in Photo 3. A 100 turn coil, inside diameter 9.538 mm, outside diameter 11.15 mm, and overall length 3.17 mm, is wound on a PVC rod to
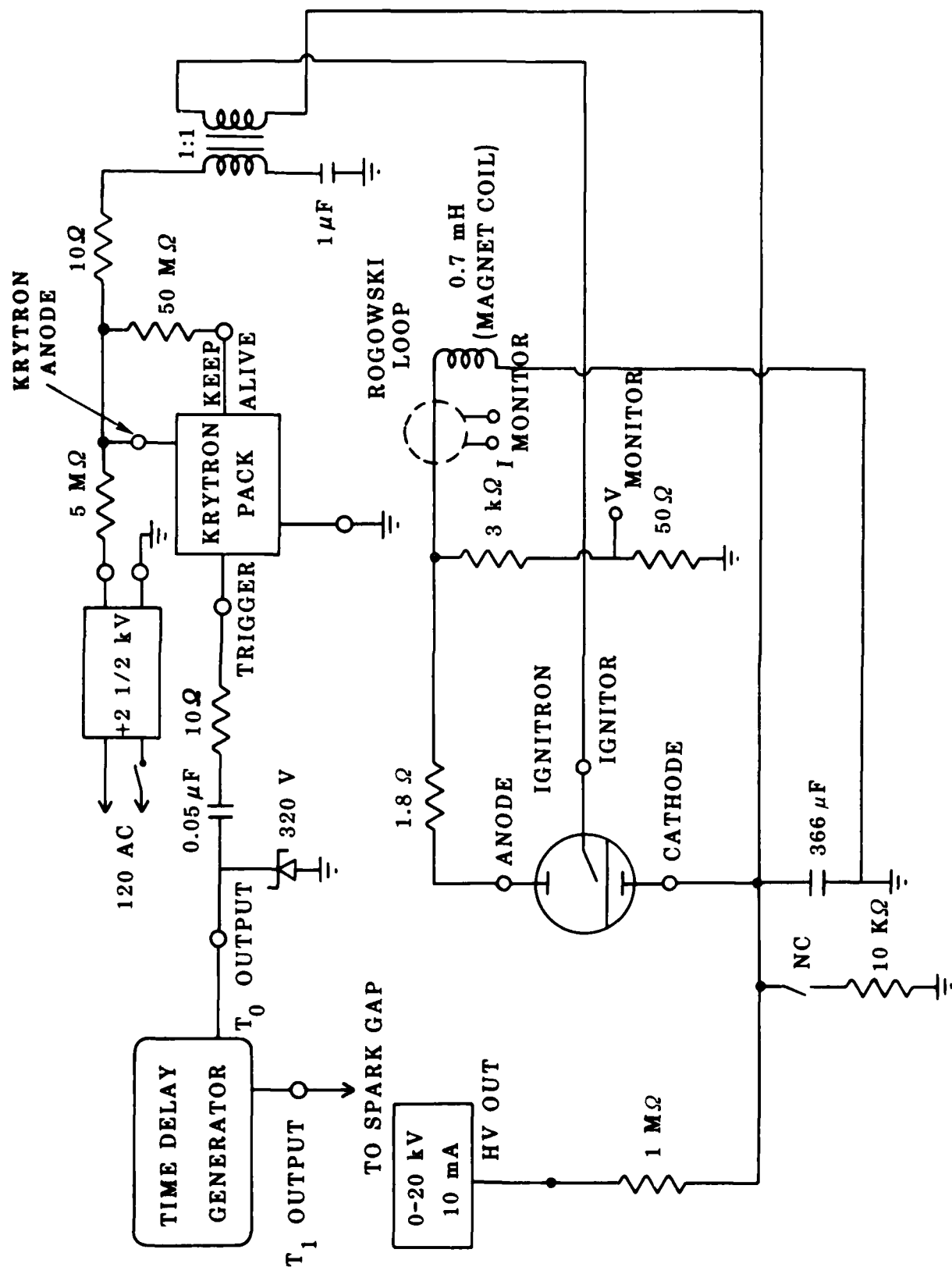
Figure 14. Schematic of the pulse power circuit which drives the vircator magnet coil. The series 1.8 Ω resistor strongly damps the magnet RLC circuit to minimize current reversal.

34
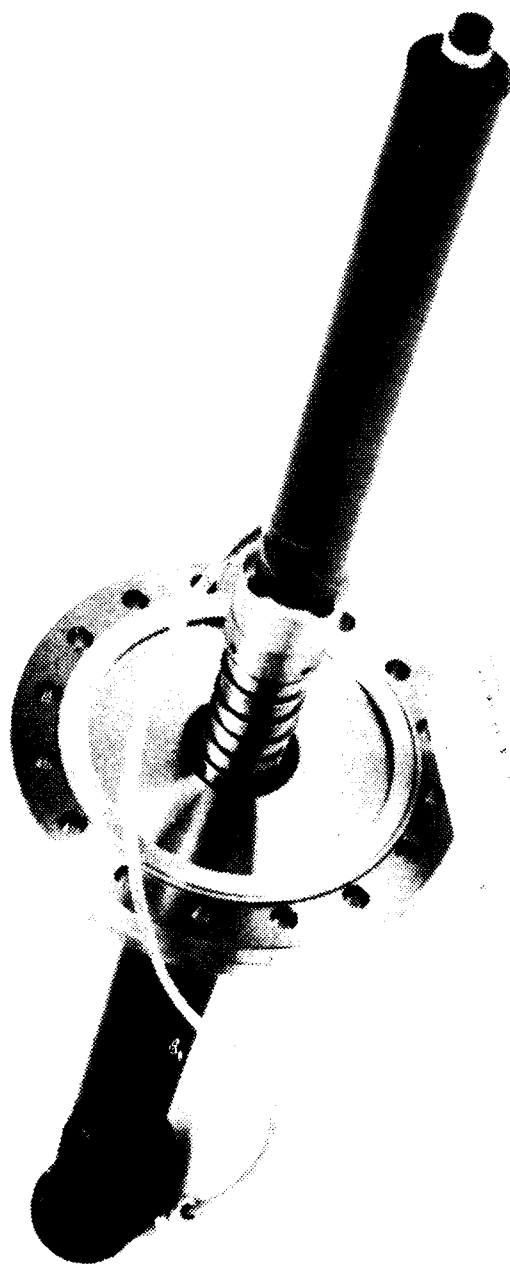
Photograph 3. B probe used to measure magnetic field amplitude and risetime. The 100 turn coil is at the far right. Measured values are consistent with the elementary RLC circuit theory described in the text. The probe axial stroke is 6 inches.

sample the B_z field. Because of the slow field rise time and low probe inductance, the probe is not self integrating and produces a B_z signal. The peak B_z field follows from the stored voltage output versus time $V(t)$ according to:

$$B_z(t) = 1.19 \times 10^6 \int_0^t dt'V(t') \quad .\tag{18}$$

The probe can be positioned anywhere along the axis of the magnet using the vacuum manipulator of Photo 3 (Huntington Mechanical Laboratories linear motion feedthrough #VF-158). A typical probe output oscilloscope trace is shown in Figure 15 for a 4.0 kV capacitor charge voltage with the probe located on axis. The magnetic field peaks at 570 µsec, and carrying out the areal integral in the above equation yields a peak field of 14.62 kG. The measured field level and risetime can be compared with analytical calculations[9] based on a simple series RLC circuit. These calculations show that for a capacitor C initially charged to a voltage V_0 and discharged at time t=0 into an underdamped series load of inductance L and resistance R (mks units), the current peaks at time t_0 at a value I_{max} given by:

$$t_0 = \frac{1}{\omega} \tan^{-1} \left(\frac{2\omega L}{R} \right) ,\tag{19}$$

$$I_{max} = \frac{V_0}{\sqrt{L/C}} \ \epsilon \quad ,\tag{20}$$

where

$$\omega^2 \equiv \frac{1-d}{LC} \quad ,\tag{21}$$

$$d \equiv \frac{R^2 C}{4L} \quad ,\tag{22}$$

and
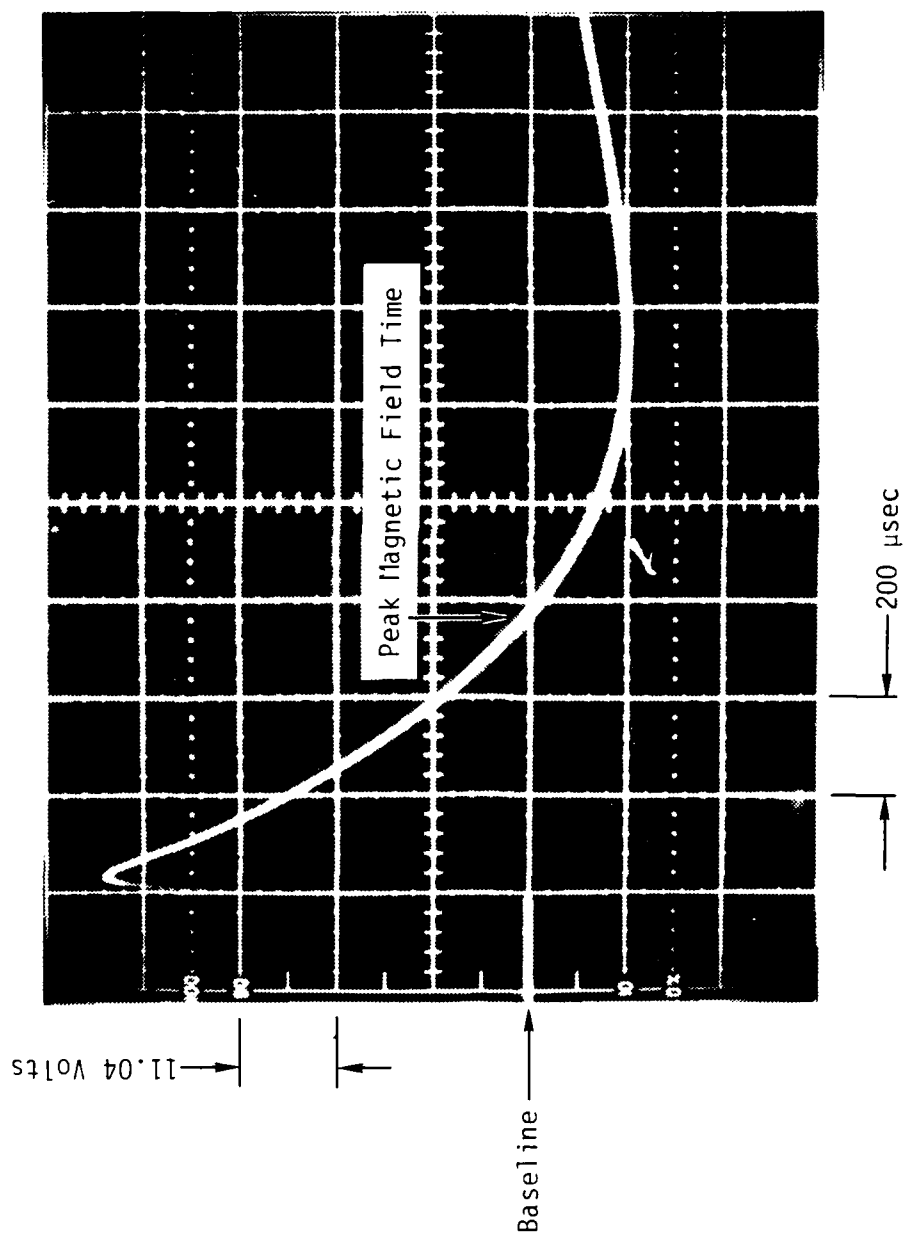
Figure 15. Output voltage versus time from the 100 turn 10.35 mm diameter $\dot{B}$ coil. Area under the curve is 5.565 div² yielding a peak magnetic field of 14.62 kG at 570 μsec.

$$\epsilon \equiv \exp\left[-\sqrt{\frac{d}{1-d}}\ \tan^{-1}\sqrt{\frac{1-d}{d}}\right]\ . \tag{23}$$

Substituting the system impedances for the vircator magnet ($R = 1.8\ \Omega$, $L = 0.7$ mH, $C = 366\ \mu F$, charge voltage $V_0 = 4$ kV) yields $t_0 = 575\ \mu sec$ and $I_{max} = 1.381$ kA. The series resistor in this circuit is a copper sulfate based liquid type with the capacity to dissipate 20 kJ with less than a 20°C temperature increase. The resistance value is determined by a piston type plunger and was not accurately measured; the 1.8 Ω value used here was chosen to give good agreement with experiment. The magnetic field at the center of the magnet B_0 is linearly proportional to the series current I_0 according to (Table II shows $B_0 = 60$ kG for $I_0 = 5.71$ kA):

$$B_0 = 10.51\ I_0(kA) \qquad kG. \tag{24}$$

Thus, for 4 kV charge voltage, the calculated field is 14.51 kG, and the risetime 575 μsec. These values are in good agreement with the measured values of 14.62 kG and 570 μsec, indicating the magnet operation is well characterized by a strongly damped series RLC circuit.

SECTION III
CALIBRATION OF THE 35-110 GHz VIRCATOR SPECTROMETER

A useful device for characterizing the intensity and wavelength of electromagnetic radiation is the spectrometer. Although Fabry-Perot interferometry and Fourier transform spectroscopy are commonly used in the UV, visible, and IR regions of the spectrum, diffraction grating spectroscopy carries over conveniently to microwave frequencies. The fast response of crystal detectors which can easily be coupled to a microwave grating spectrometer makes this a good choice for monitoring radiation from pulsed sources. A grating spectrometer specifically designed to monitor millimeter waves has been fabricated. The design philosophy has been previously described.[10,11] Spectrometer calibration is described here.

The main tool used in calibrating the vircator spectrometer is a Micro-Now Model #705B millimeter wave sweeper system with appropriate heads for B-band (35-50 GHz), V-band (50-75 GHz), and W-band (75-110 GHz) frequencies. The manufacturer provided calibration curves in frequency and power for each head are given in Figures 16-18. The sweeper system was lent to MRC by Dan Hunt of White Sands Missile Range Office OMEW/P2. His assistance has been invaluable. Each of the three millimeter bands covered by the spectrometer has its own set of detectors, 3 each for B and V-bands, and 6 for W-band. Type 1N53 crystal detectors have been chosen for all 3 bands, due to their low cost and good availability. The crystal housings are Baytron #4-22-200 for B band, Baytron #4-15-2000 for V band, and Baytron #4-10-200 for W band. Each channel also has its own pair of gratings which have been optimized for use at that particular wavelength window. The spectrometer operates in only one band at a time with only one set of detectors being used at a time. In each band a nominal 25 dB standard gain horn is used as the input to the spectrometer in order to increase the signal. Calibration curves for the horns in each band are presented in Figures 19-21. Calibration of each band for frequency response and sensitivity is carried out separately.

39
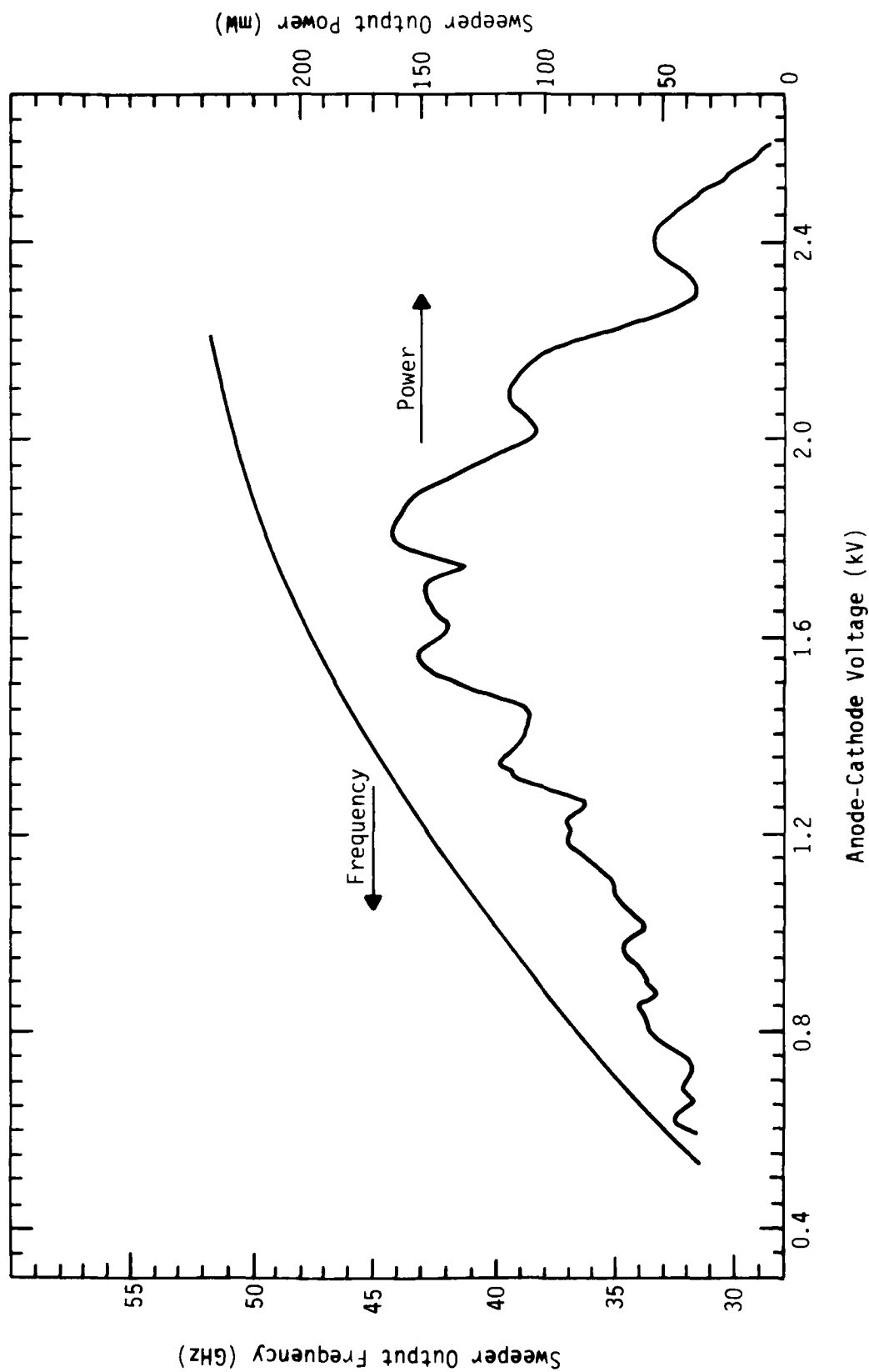
Figure 16. Manufacturer provided calibration curve of B-band sweeper power and frequency output as a function of oscillator head anode-cathode voltage (Micro-Now Model #705B mainframe and Model #729 BWO head). The sweeper drives the spectrometer and oscilloscope in the configuration of Figures 22 and 23 to produce the calibration data shown in Figures 24 through 35.
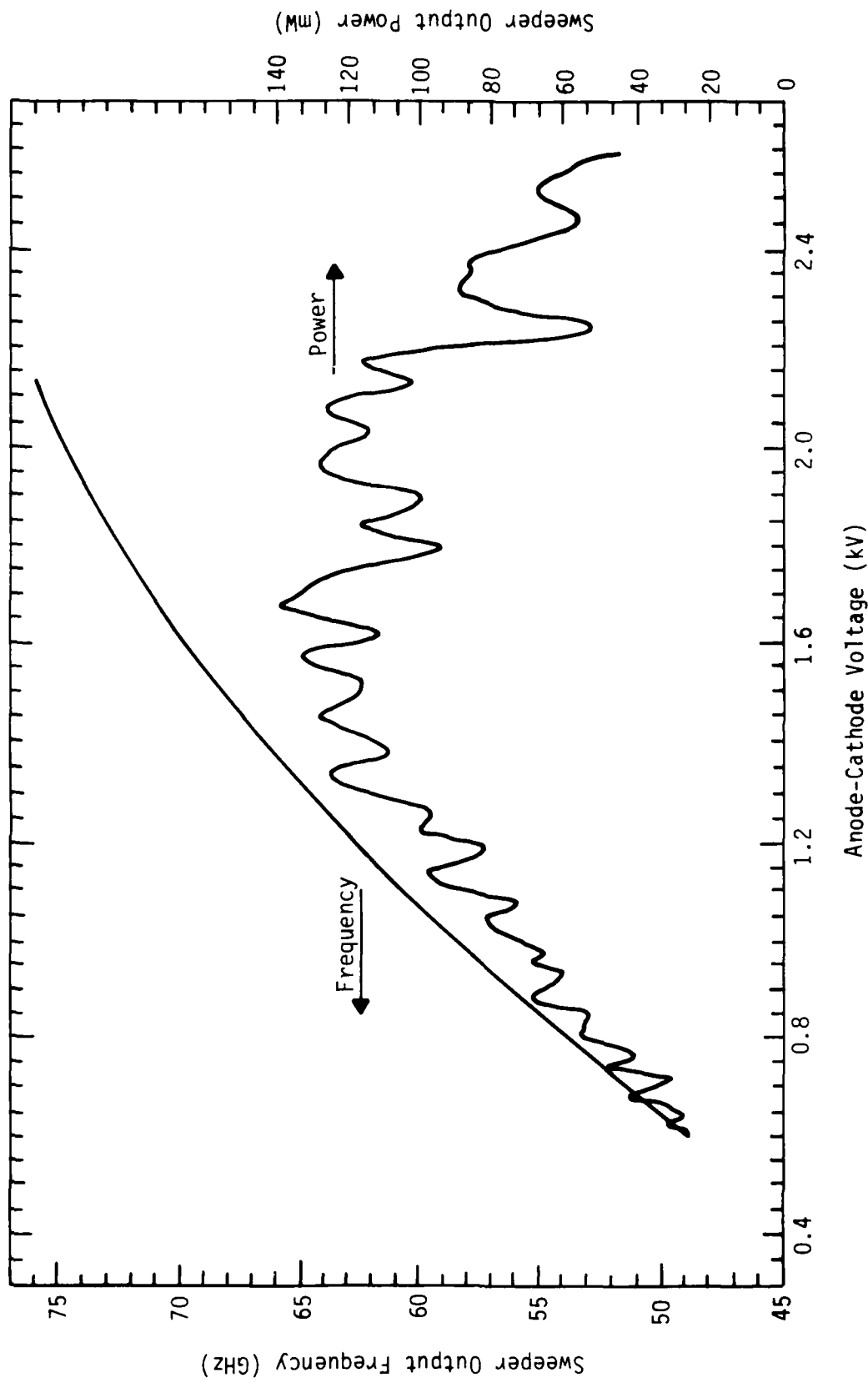
Figure 17. Manufacturer provided calibration curve of V-band sweeper power and frequency output as a function of oscillator head anode-cathode voltage (Micro-Now Model #705B mainframe and Model #725 BWO head).

41
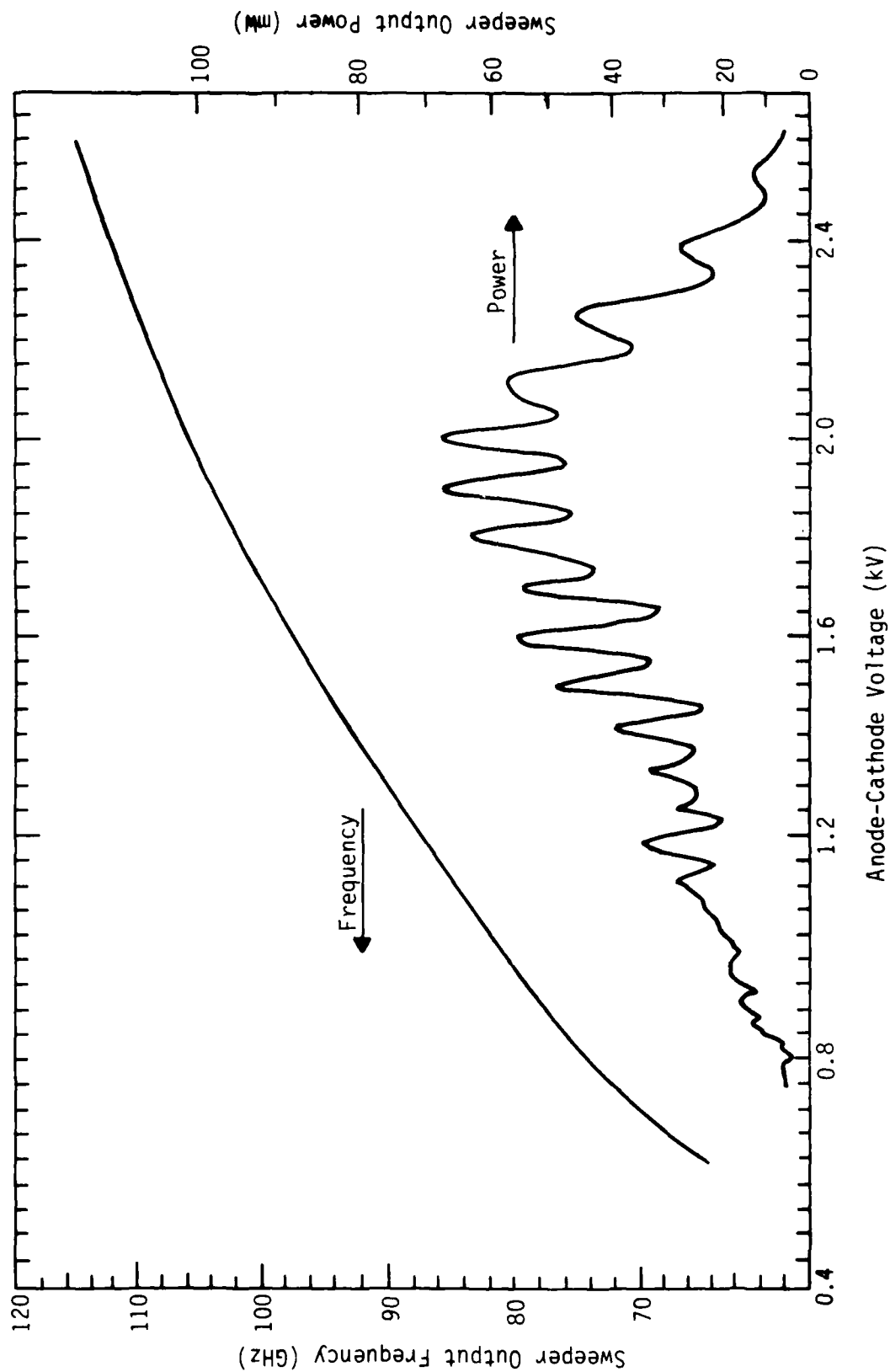
Figure 18. Manufacturer provided calibration curve of W-band sweeper power and frequency output as a function of oscillator head anode-cathode voltage (Micro-Now Model #705B mainframe and Model #728 BWO head).
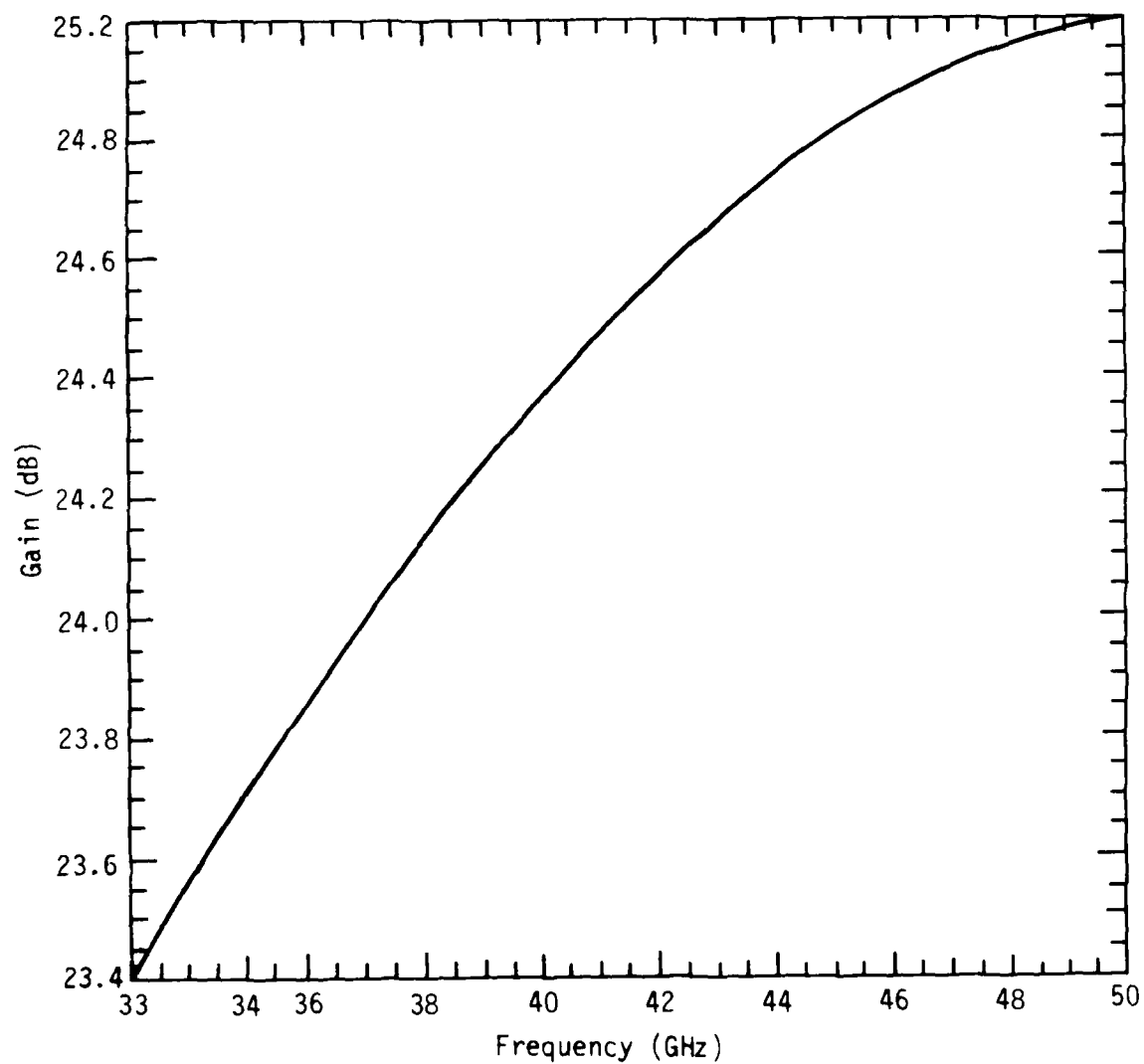
Figure 19. Manufacturer provided calibration curve for the B-band (35-50 GHz) 25 dB standard gain horn used in spectrometer calibration (TRG Model #B861).
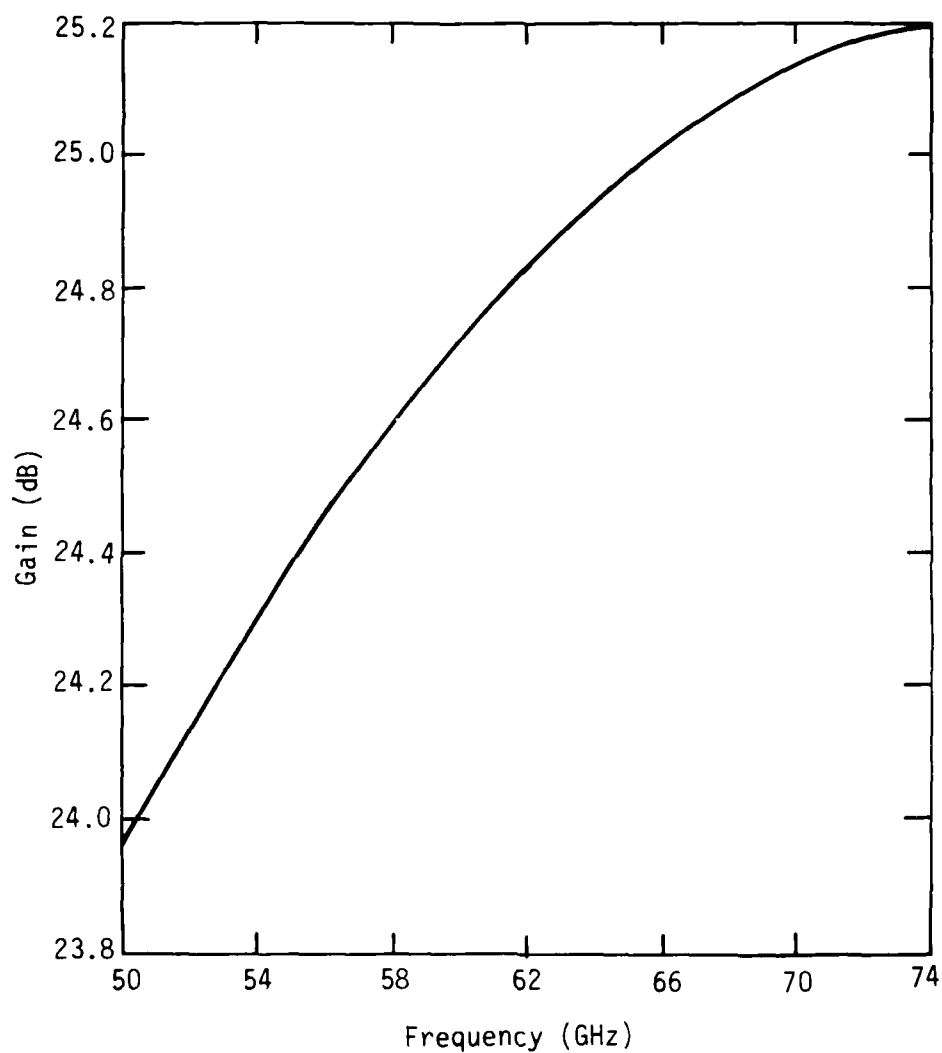
Figure 20. Manufacturer provided calibration curve for the V-band (50-75 GHz) 25 dB standard gain horn used in spectrometer calibration (TRG Model #V861).
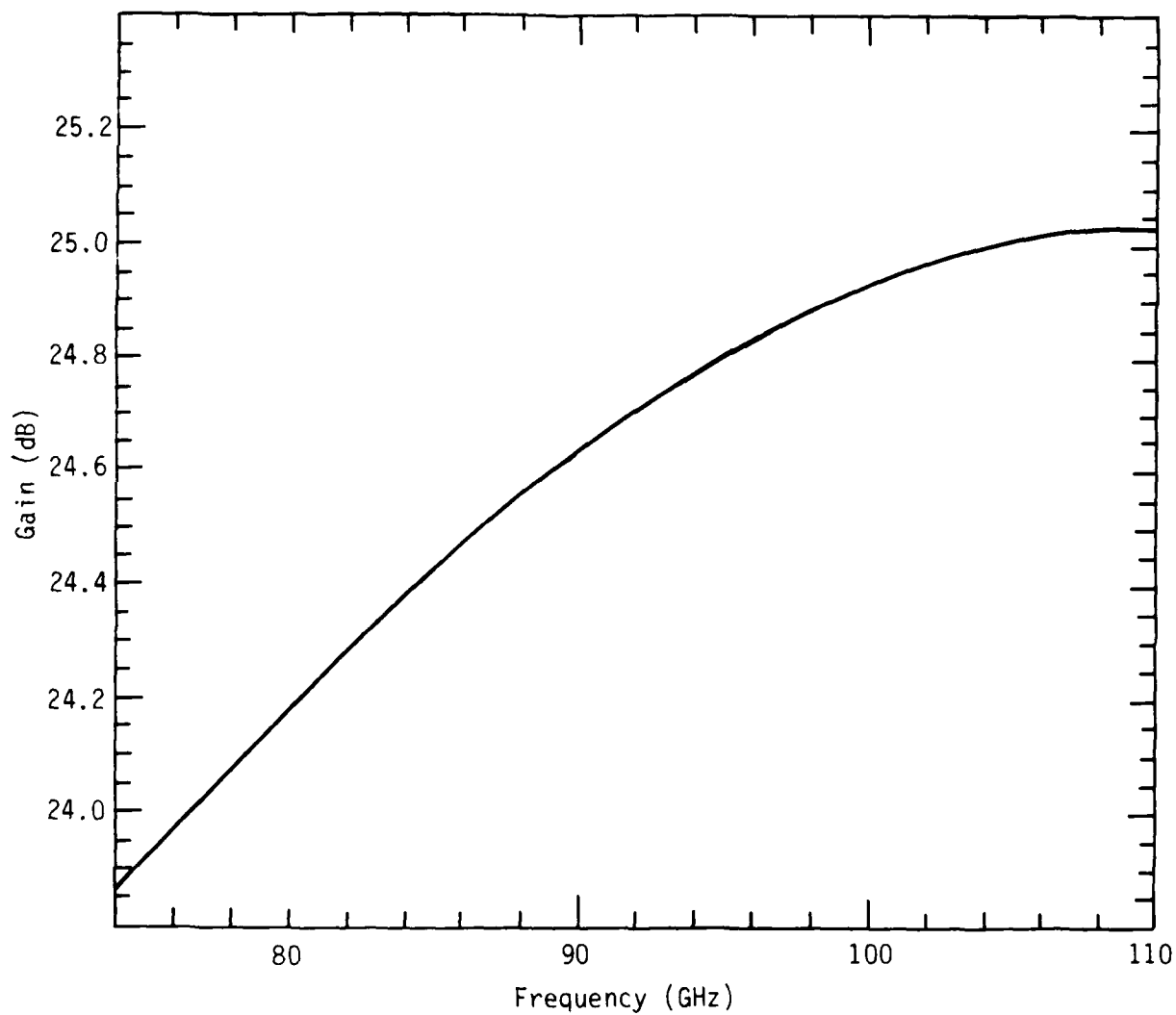
Figure 21. Manufacturer provided calibration curve for the W-band
(75-110 GHz) 25 dB standard gain horn used in spectrometer
calibration (TRG Model #W861).

Two calibrations were performed for each band. The flatness of the frequency response of each of the three (or six) detectors is measured using the apparatus shown in Figure 22. Two series 10 or 15 dB couplers are used to attenuate the nominal 100 mW sweeper output to levels which will not overdrive the crystal. As shown in the figure, the sweeper provides a ramp signal to the oscilloscope which varies linearly in time corresponding to the linear time variation of the output frequency. The scope photo then records the frequency response of the crystal, uncorrected for variations in the sweeper output power.

Next the array of detectors is positioned inside the spectrometer so that each samples a different frequency bin. In this configuration shown in Figure 23, the sweeper drives the spectrometer directly, since the spectrometer itself is very lossy, of order 35 dB. In order to increase the signal to a measurable level, a 25 dB standard gain horn is attached to the waveguide entrance flange which feeds each of the crystals. The calibration curves for these horns are shown in Figures 19, 20, and 21 for B, V, and W-band, respectively. Power variation in the sweeper output as a function of frequency is shown in Figures 16, 17, and 18 for B, V, and W-band, respectively. To the extent that the detector crystal response is linear with input power, these curves and the following data allow an absolute power calibration of the spectrometer frequency response.

Raw data for the three B-band detectors' frequency response is shown in Figure 24. In order to determine the actual crystal sensitivity as a function of frequency, this raw data should be divided point-by-point by the sweeper power output as a function of frequency. The latter quantity is available from the plots of Figure 16. Note that this process also involves an assumption that the crystal voltage output is linear in the power input, i.e., the crystal is operating in the square law regime. Since the extensive tests required to verify square law operation over the entire frequency band have not been done, the tedious point-by-point division has not been carried out. Noting that the input power does not vary by more than a factor of 2, some broad conclusions can still be drawn from
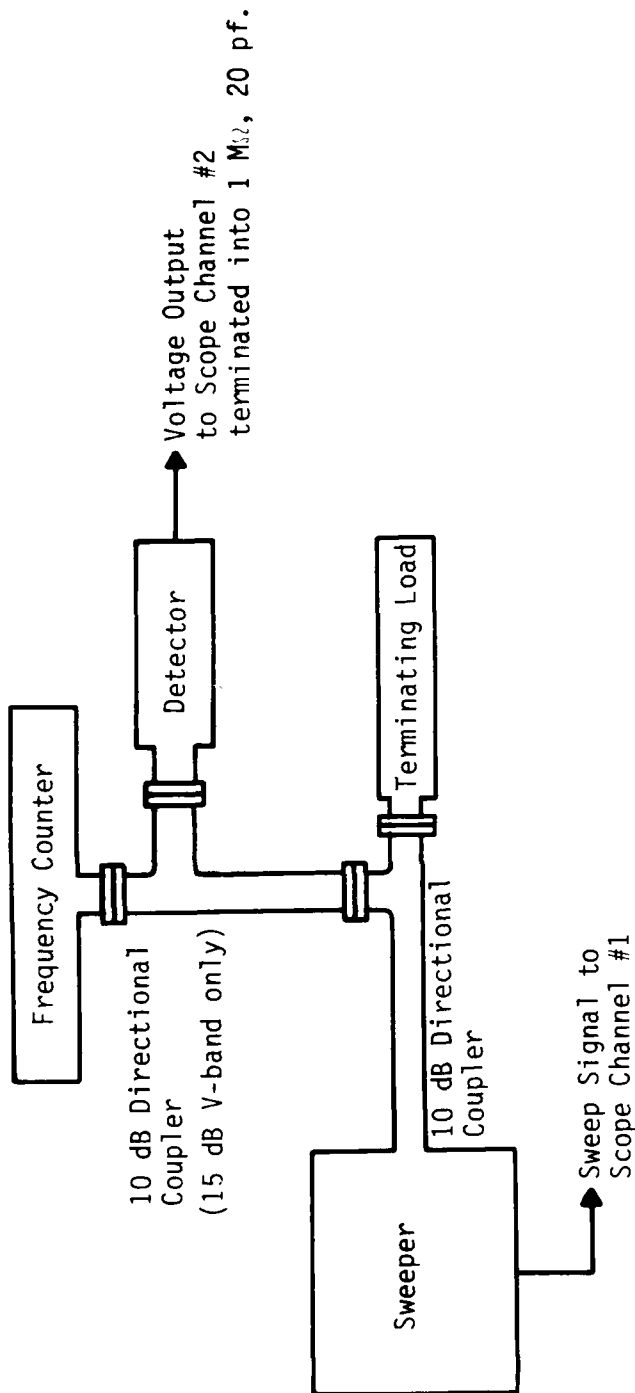
Figure 22. Schematic of the apparatus used in detector calibration. Two directional couplers are configured in series to reduce the sweeper output signal to the mW level which can be tolerated by the detectors.

47

25 dB horn

Detector 1
Detector 2
Detector 3
Detector 4
Detector 5
Detector 6

Voltage Output
to Scope Channel #2
terminated into 1 M,
20 pf.

Microwave
Spectrometer

Frequency
Counter

10 dB Directional
Coupler

Sweep Signal to
Scope Channel #1

Sweeper
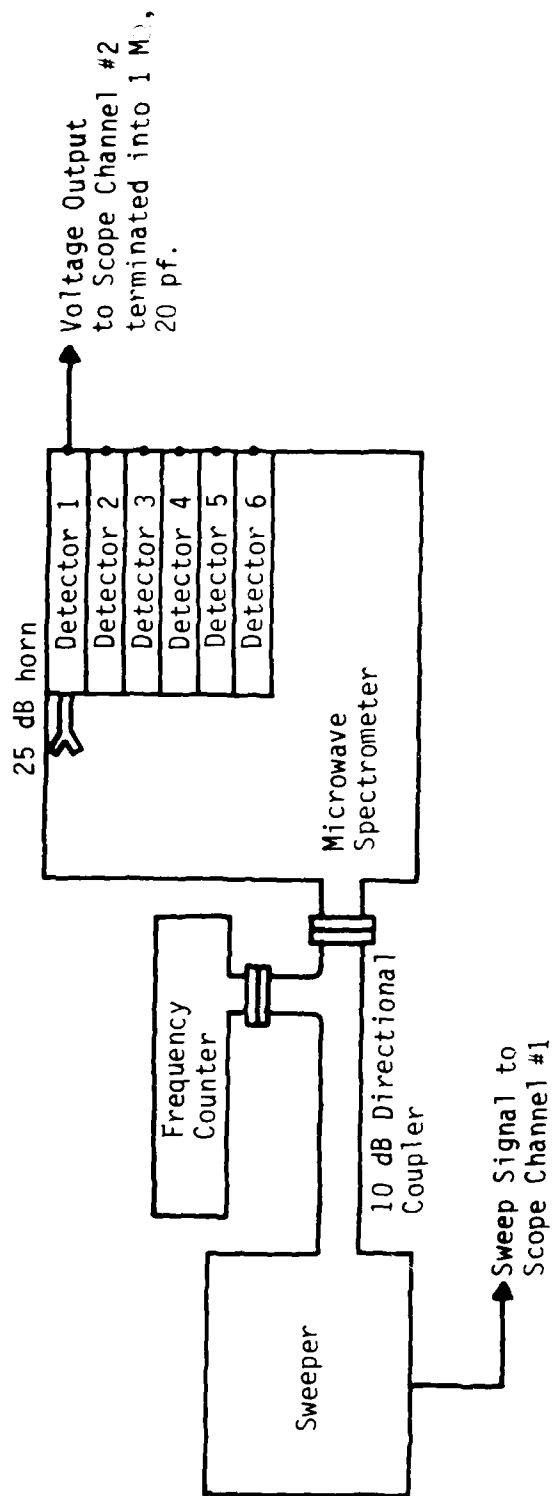
Figure 23. Schematic of the apparatus used to calibrate the frequency response of the six (three each in B and V-band and six in W-band) spectrometer channels. The 25 dB horn is inserted during the calibration to increase the signal to a measurable level.

48

Detector #B1

100mV

32 GHz   50 GHz

Detector #B3

100mV

32 GHz   50 GHz

Detector #B2

100mV

32 GHz   50 GHz

Figure 24.   Detector calibration data for the three B-band detectors, taken using the apparatus of Figure 22.

the raw data. First, detector response is down considerably at high frequencies, dropping by the order of one decade above 44 GHz. Second, response is fairly flat, within a factor of 2, in the 32 to 44 GHz frequency bin. The fine structure in the raw data is due to resonances in the detector housing and some inherent non-linearity in the crystal response. Superior quality detectors can be purchased at a premium price for future work, if it becomes necessary to provide flatter response over the entire band.

Next, detectors B1, B3 and B2 were installed in the spectrometer at stations 15.5, 8.0, and 3.0 inches, respectively, and the spectrometer driven with the sweeper in the configuration of Figure 23. Data was taken with the grating angle at 42 degrees and 48 degrees, as shown in Figures 25 and 26. The grating angle determines the acceptance frequency of each detector through the optics criteria described in References 10 and 11.

A summary of the B-band calibration data is presented in Table III for the 42 degree and 48 degree grating angles tested. The center frequency for peak sensitivity and the peak output voltage are listed for each detector. Note that the FWHM response is approximately 2 GHz, yielding a $\Delta f/f_0$ parameter of order 0.06. A figure of merit parameter has been calculated by dividing the output voltage by the sweeper output power, taking into account the frequency dependence of the horn gain and the loss due to the 10 dB coupler preceding the spectrometer. To the extent that the crystal output is linear with input power, the figure of merit is an absolute calibration of the spectrometer sensitivity for that particular detector, frequency, and grating angle. Table III shows that the figure of merit varies by nearly two decades from one frequency bin to another. This is just a reflection of the poor flatness in the frequency response of the individual crystals and can be rectified by purchasing better housings and better crystals.

Detector #B1, Angle 42°

32 GHz   50 GHz

Detector #B3, Angle 42°

32 GHz   50 GHz

Detector #B2, Angle 42°

32 GHz   50 GHz

Figure 25. Spectrometer calibration data for the three B-band detectors
            (detector B1 at 15.5 inch, B3 at 8.0 inch, and B2 at 3.0 inch)
            taken at a 42 degree grating angle, using the configuration
            of Figure 23.

51

Detector #B1, Angle 48°

32 GHz   50 GHz

Detector #B3, Angle 48°

32 GHz   50 GHz

Detector #B2, Angle 48°

32 GHz   50 GHz

Figure 26. Spectrometer calibration data for the three B-band detectors (detector B1 at 15.5 inch, B3 at 8.0 inch, and B2 at 3.0 inch) taken at a 48 degree grating angle.

TABLE III. SUMMARY OF SPECTROMETER B-BAND (32-50 GHz) CALIBRATION DATA

PARAMETER	Detector #B1	Detector #B3	Detector #B2
Detector Position (inches)	15.5	8.0	3.0
For 42° Grating Angle:			
Center Frequency for Peak Sensitivity (GHz)	38.4	43.8	48.8
Output Voltage (mV)	180	59	6.2
Horn Gain (db)	24.2	24.7	25.0
Input Power (mW)	60	96	145
Calculated Figure of Merit (Volts/Watt)	1.27×10^{-2}	2.31×10^{-3}	1.50×10^{-4}
For 48° Grating Angle:			
Center Frequency for Peak Sensitivity (GHz)	33.2	38.0	41.4
Output Voltage (mV)	89	89	134
Horn Gain (db)	23.4	24.1	24.5
Input Power (mW)	43	57	70
Calculated Figure of Merit (Volts/Watt)	1.05×10^{-2}	6.75×10^{-3}	7.55×10^{-3}

Calibration of the V-band response of the detectors and spectrometer was carried out analagously to the B-band calibration data. Figure 27 shows the response of the three individual crystals and Figures 28, 29, and 30 show the spectrometer response for 44, 46, and 49 degree grating angles, respectively. Peak frequency response and figure of merit numbers are summarized in Table IV. Note that the separate detector responses are far from flat, typically varying by the order of one decade between peaks and valleys. This is the main culprit in the factor of 40 variation in the sensitivity of the various frequency bins. The data shows typical FWHM of the frequency response is about 2 GHz, yielding a $\Delta f/f_0$ parameter of approximately 0.04.

Calibration of the W-band detectors was carried out in a similar manner to the B and V-bands, but was complicated by the extremely hashy and non-uniform frequency response of these crystals and their housings. The data of Figures 31A and 31B shows a variation of more than two decades in the raw frequency response data over the 75-110 GHz frequency band for several of the 6 detectors. Calibration data for the W-band spectrometer configuration is shown in Figures 32 through 35, with a data summary in Table V. Frequency response FWHM is typically 2 GHz, yielding a $\Delta f/f_0$ parameter of order 0.027. The figure of merit parameter continues to show large variation, roughly two decades, over the frequency band. Thus, the frequency selectivity of this spectrometer is good although it displays wide variation in power sensitivity. The latter undesirable characteristic can be corrected in future work by installing crystals with flatter frequency response in housings with weaker resonance characteristics. However, in its present form and with the calibration data presented here, the spectrometer is a unique diagnostic for characterizing the time dependence, power and spectral content of pulsed, millimeter wavelength microwave sources.
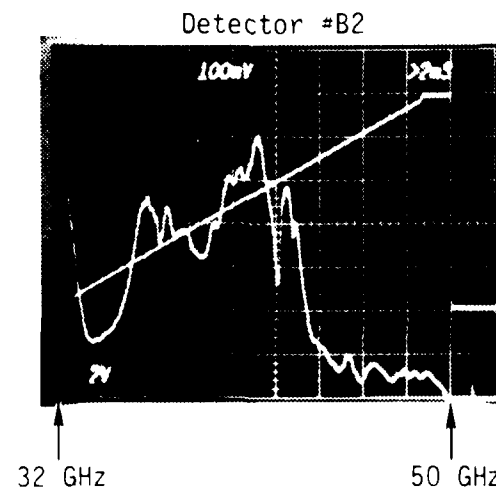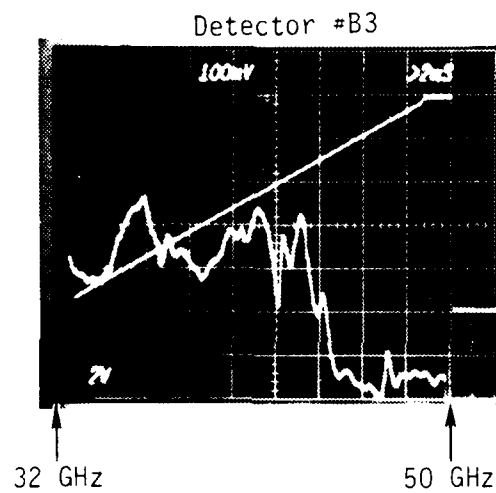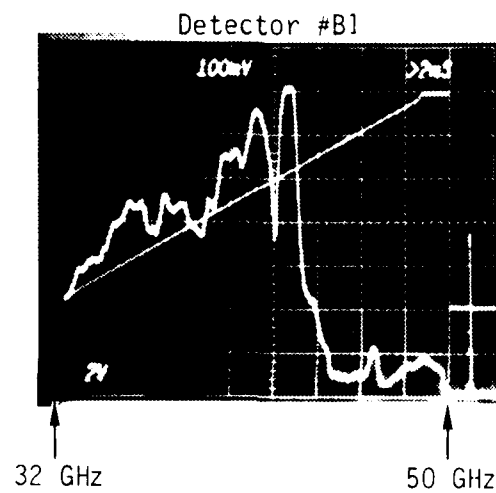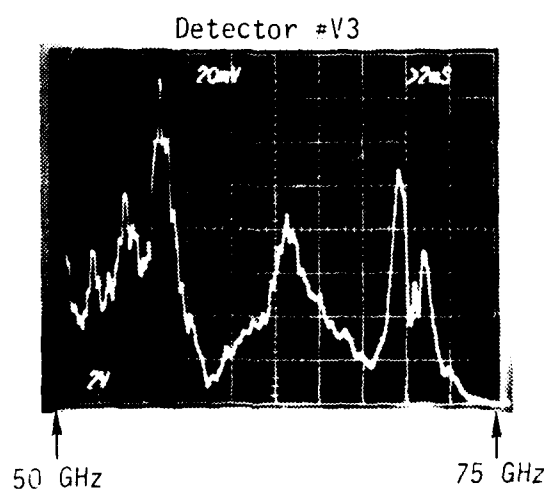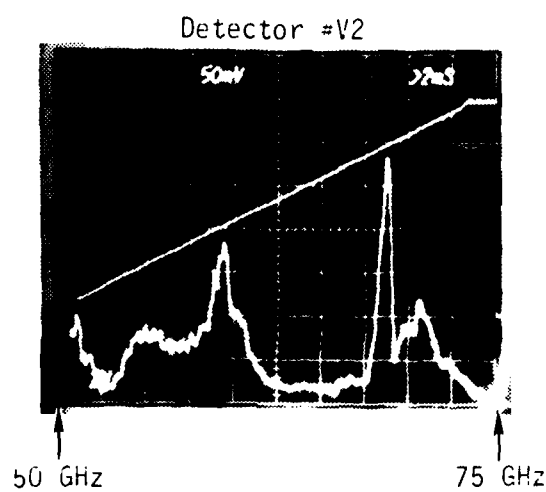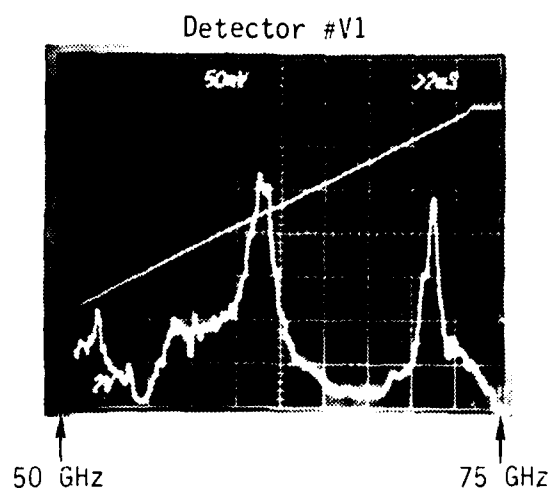
Figure 27. Detector calibration data for the three V-band detectors, taken using the apparatus of Figure 22.

Detector #V1, Angle 44°

50 GHz   75 GHz

Detector #V2, Angle 44°

50 GHz   75 GHz

Detector #V3, Angle 44°

50 GHz   75 GHz
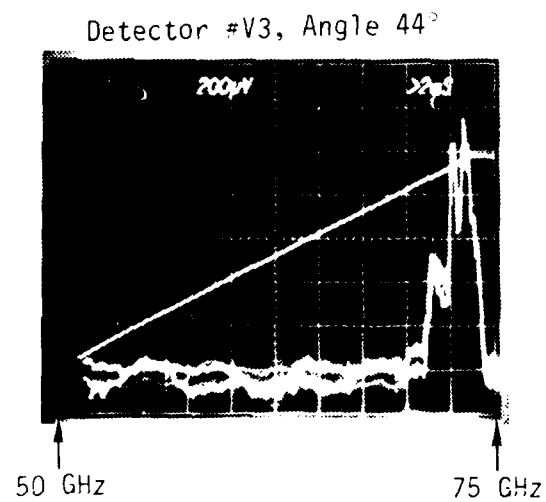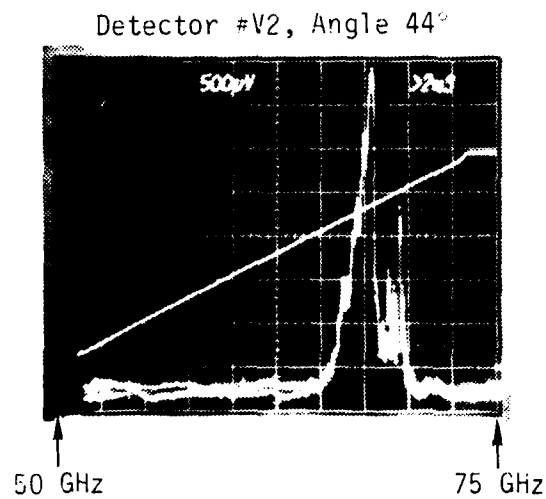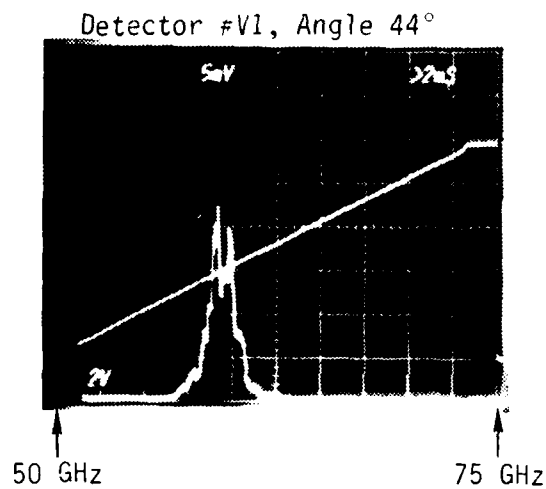
Figure 28.   Spectrometer calibration data for the three V-band detectors (detector V1 at 15.5 inch, V2 at 8.0 inch, and V3 at 3.0 inch) taken at a 44 degree grating angle, using the configuration of Figure 23.

56

Detector #V1, Angle 46°

50 GHz   75 GHz

Detector #V2, Angle 46°

50 GHz   75 GHz

Detector #V3, Angle 46°

50 GHz   75 GHz
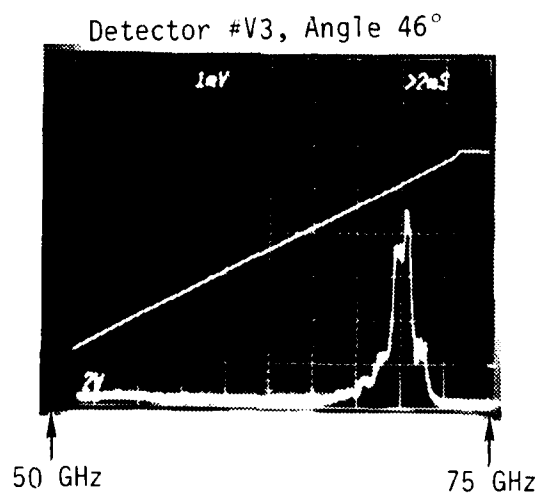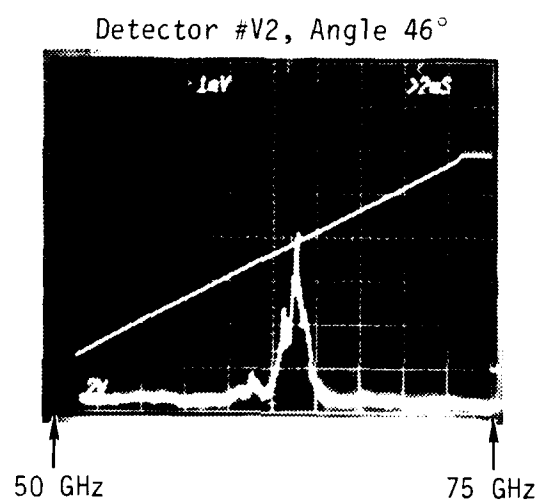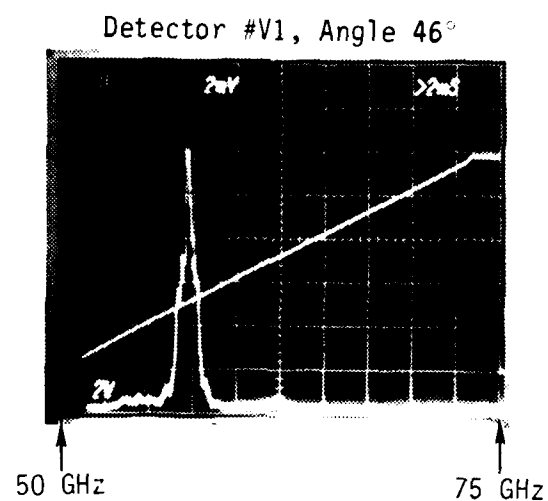
Figure 29. Spectrometer calibration data for the three V-band detectors
            (detector V1 at 15.5 inch, V2 at 8.0 inch, and V3 at 3.0 inch)
            taken at a 46 degree grating angle.

57

Detector #V1, Angle 49°

50 GHz   75 GHz

Detector #V2, Angle 49°

50 GHz   75 GHz

Detector #V3, Angle 49°

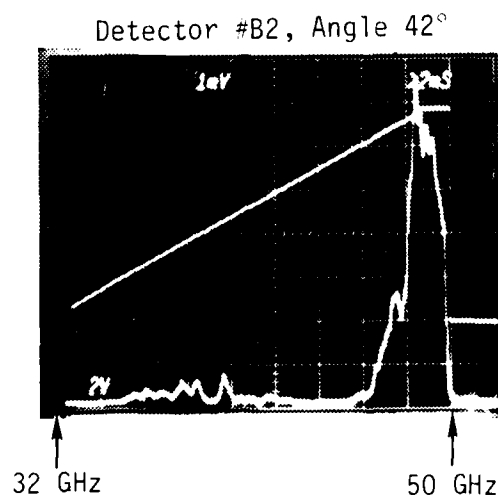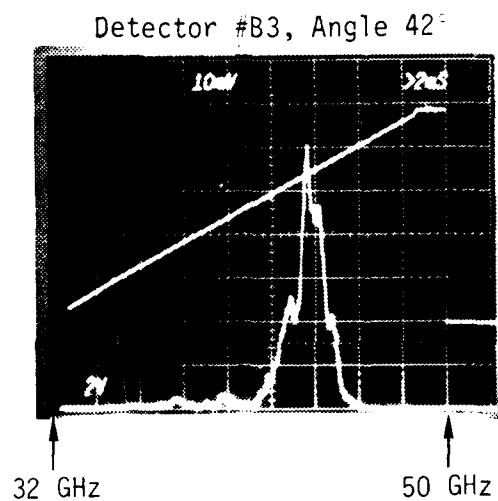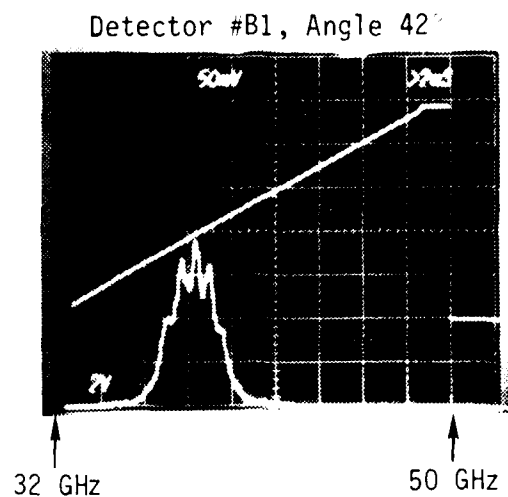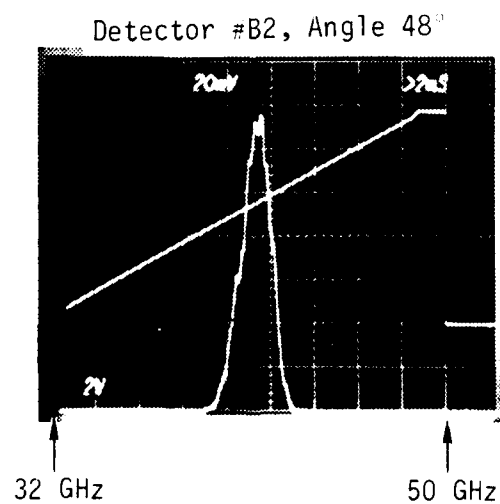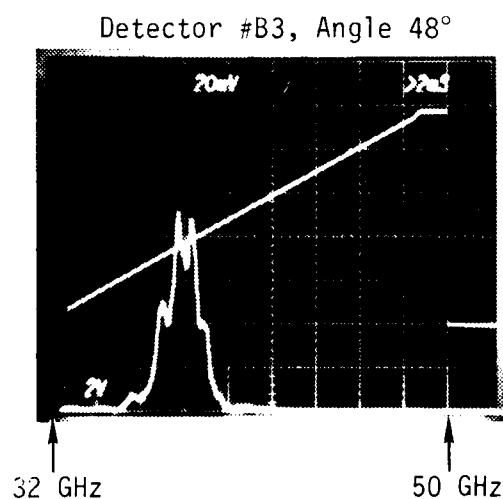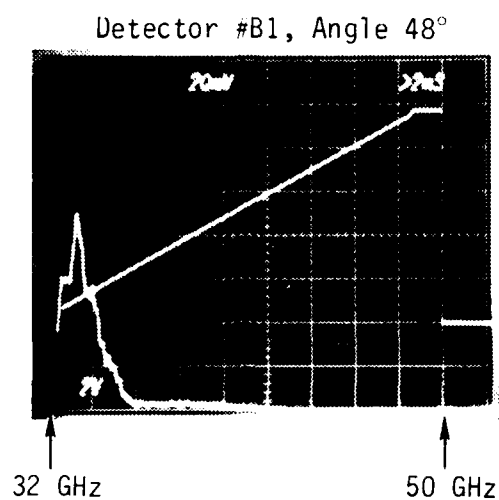50 GHz   75 GHz
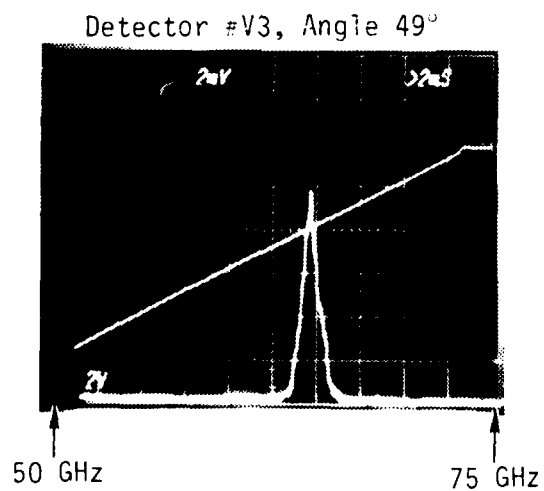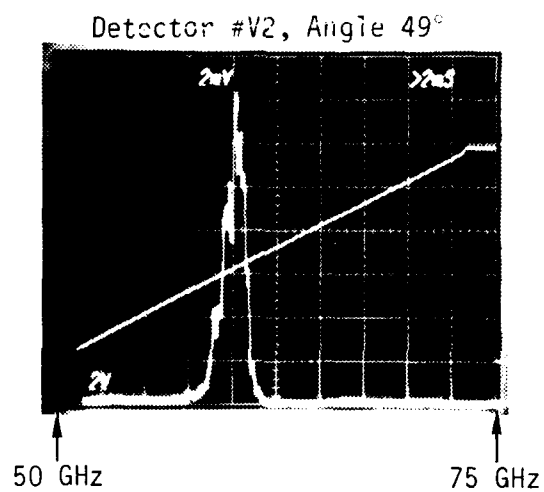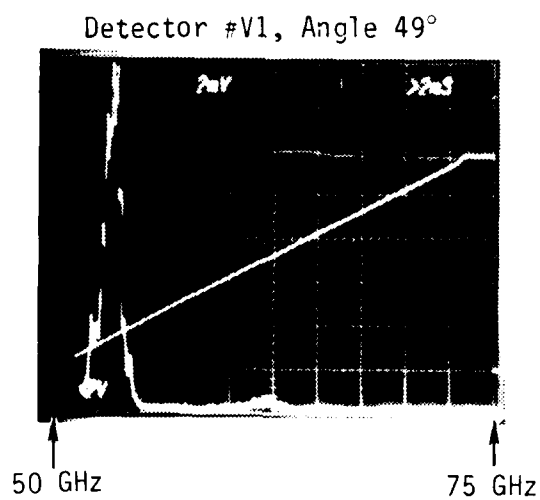
Figure 30.   Spectrometer calibration data for the three V-band detectors
             (detector V1 at 15.5 inch, V2 at 8.0 inch, and V3 at 3.0 inch)
             taken at a 49 degree grating angle.

TABLE IV. SUMMARY OF SPECTROMETER V-BAND (50-75 GHz) CALIBRATION DATA

	Detector #V1	Detector #V2	Detector #V3
Detector Position (inches)	15.5	8.0	3.0
For 44° Grating Angle: Center Frequency for Peak Sensitivity (GHz)	59.5	67.9	73.0
Output Voltage (mV)	20	3.5	1.2
Horn Gain (db)	24.8	25.1	25.2
Input Power (mW)	82	127	110
Figure of Merit (Volts/Watt)	8.97×10^{-4}	9.46×10^{-5}	3.05×10^{-5}
For 46° Grating Angle Center Frequency for Peak Sensitivity (GHz)	57.1	63.8	70.2
Output Voltage (mV)	11.5	3.8	4.3
Horn Gain (db)	24.5	24.9	25.1
Input Power (mW)	66	96	126
Figure of Merit (Volts/W)	6.87×10^{-4}	1.42×10^{-4}	1.17×10^{-4}
For 49° Grating Angle Center Frequency for Peak Sensitivity (GHz)	53.1	60.2	64.7
Output Voltage (mV)	15.8	13.8	9.6
Horn Gain (db)	24.2	24.7	25.0
Input Power (mW)	50	80	105
Figure of Merit (Volts/Watt)	1.33×10^{-3}	6.49×10^{-4}	3.21×10^{-4}

Detector #W1

Detector #W1, x10 gain

Detector #W2

Detector #W2, x5 gain

Detector #W3

Detector #W3, x4 gain

75 GHz   110 GHz
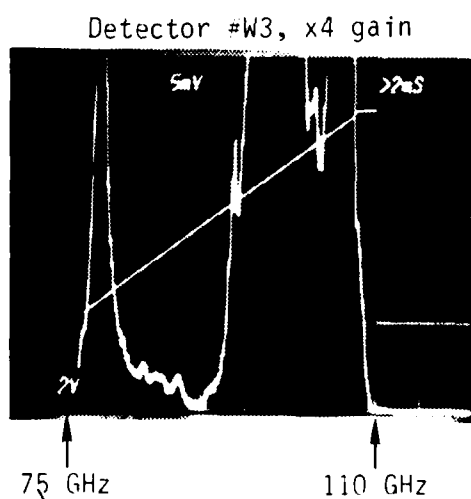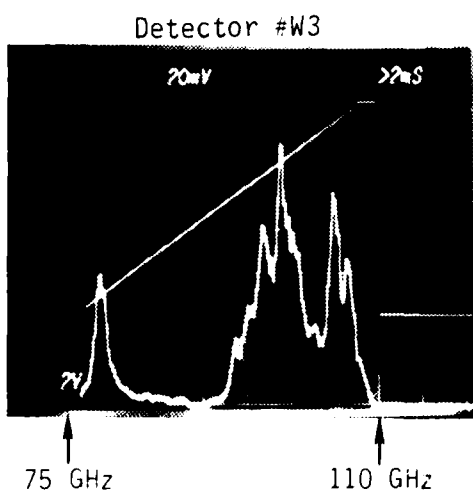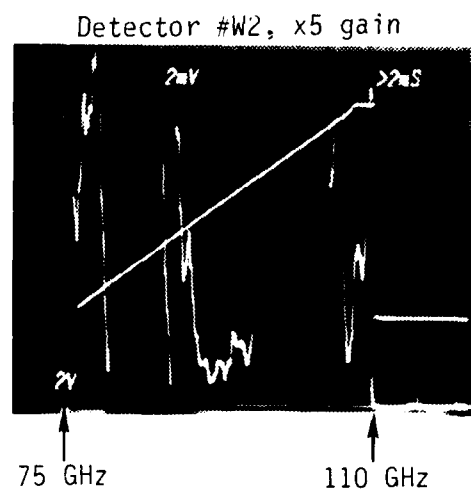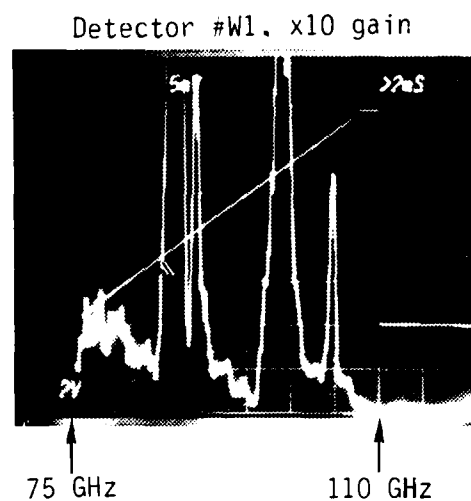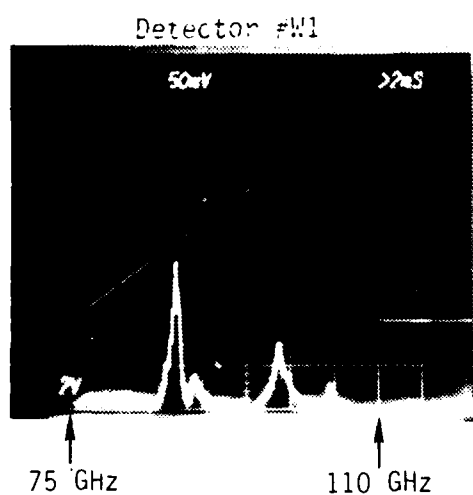
Figure 31A.   Detector calibration data for the first three W-band detectors
W1, W2, and W3, taken using the apparatus of Figure 22. Data
shown on the right is taken at several times the gain of the left,
as is reflected in the labels on the scope photos.

60
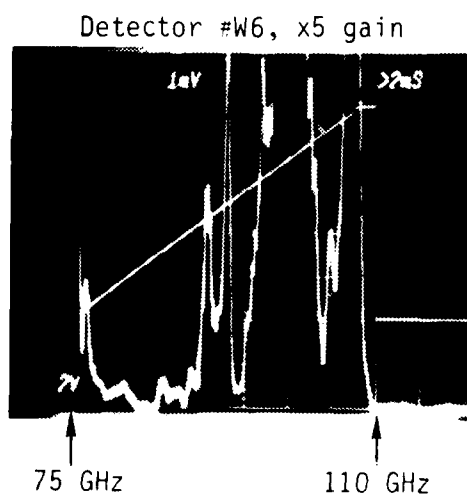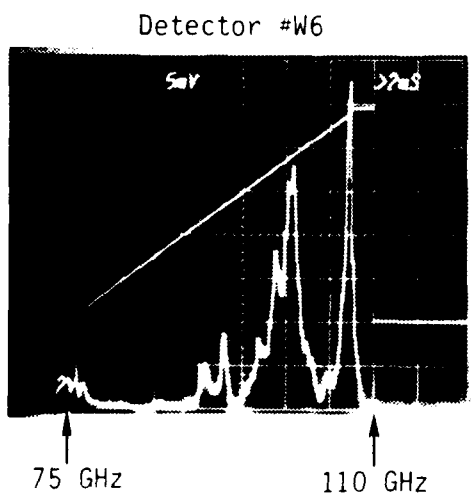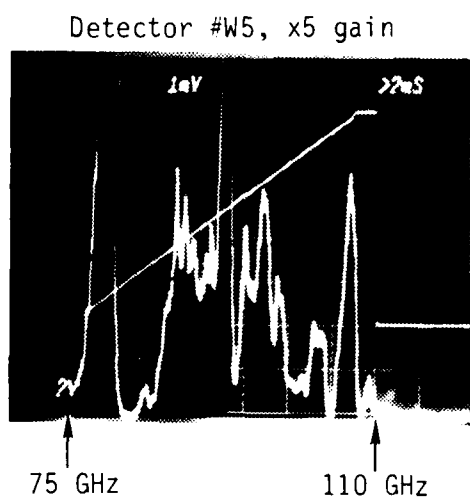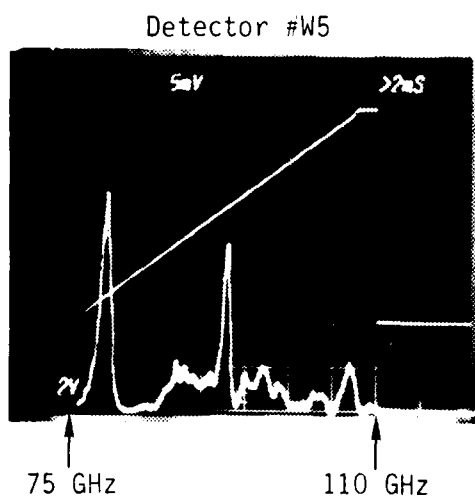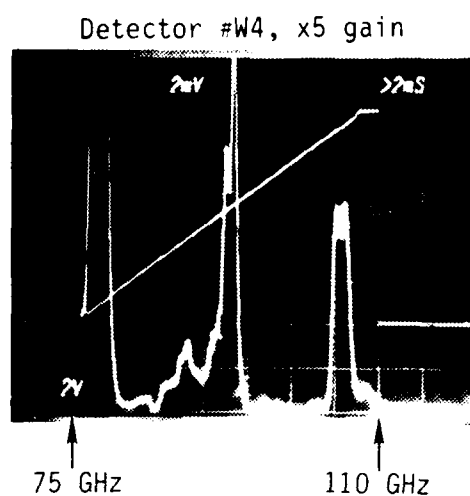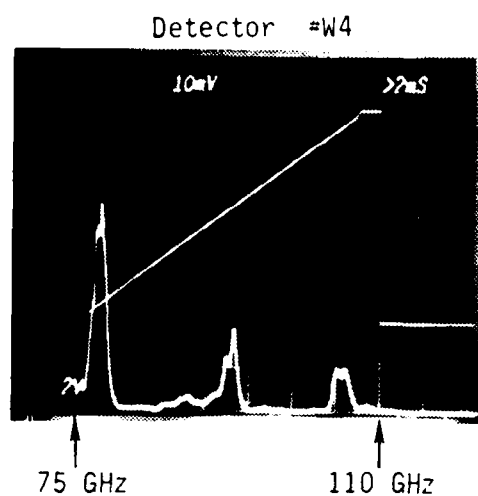
Figure 31B. Detector calibration data for the last three W-band detectors, W4, W5. and W6, taken using the apparatus of Figure 22. Data shown on the right is taken at several times the gain of the left, as is reflected in the labels on the scope photos.

61

Detector #W2, Angle 44°

75 GHz   110 GHz

Detector #W3, Angle 44°

75 GHz   110 GHz

Detector #W6, Angle 44

75 GHz   110 GHz

Detector #W6, Noise Only

75 GHz   110 GHz
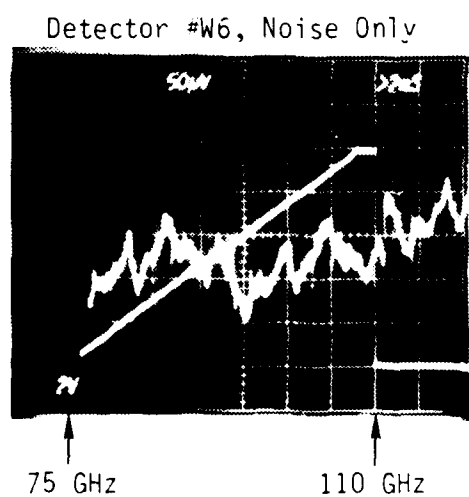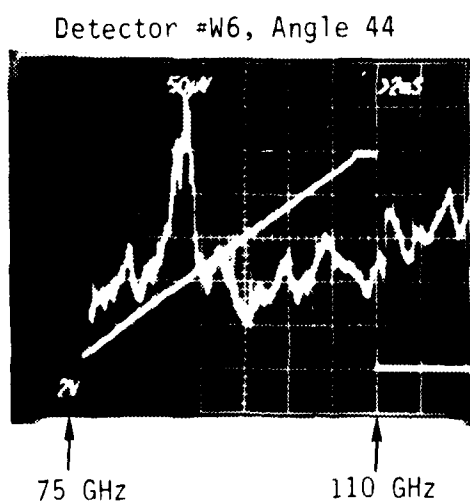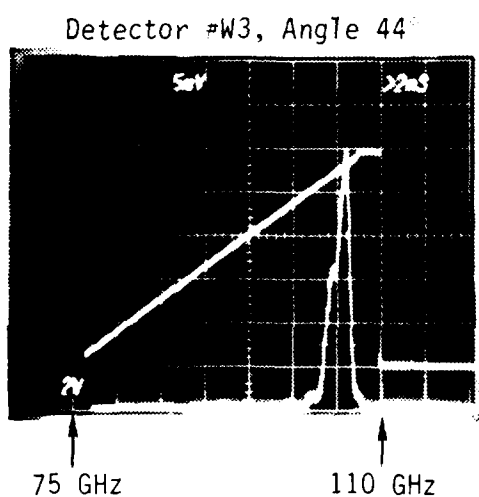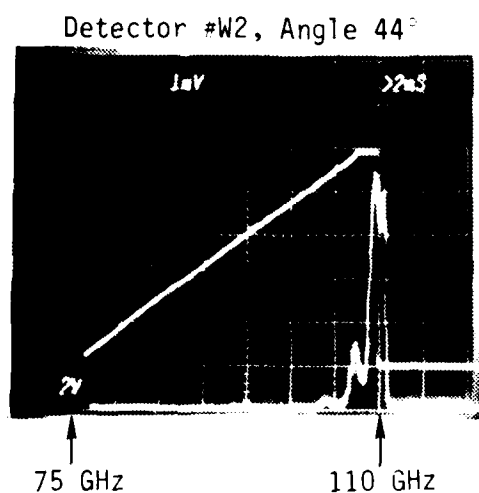
Figure 32. Spectrometer calibration data for the W-band detectors W2, W3, and W6 (detector W2 at 5.5 inch, W3 at 8.0 inch, and W6 at 15.5 inch) taken at a 44 degree grating angle, using the configuration of Figure 23. Left photo is signal plus noise, right photo is noise only, taken with microwave absorbing material covering the detector.

62

Detector #W1, Angle 46

75 GHz   110 GHz

Detector #W2, Angle 46

75 GHz   110 GHz
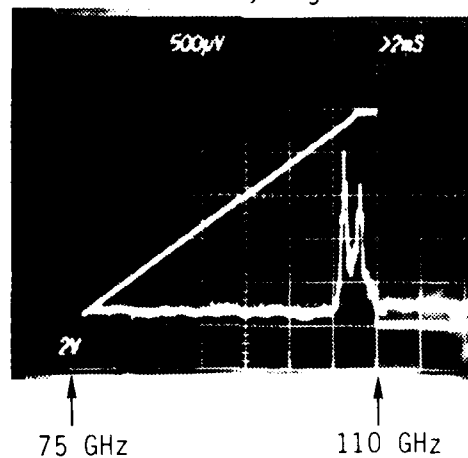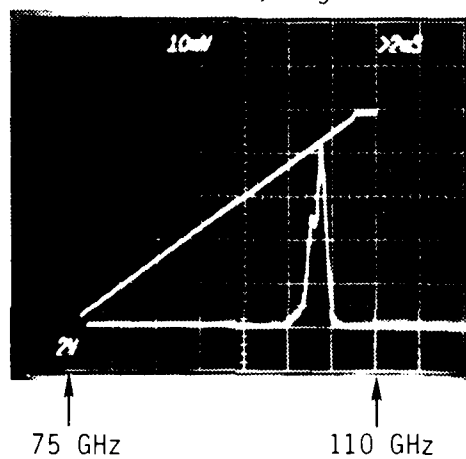
Detector #W3, Angle 46

75 GHz   110 GHz
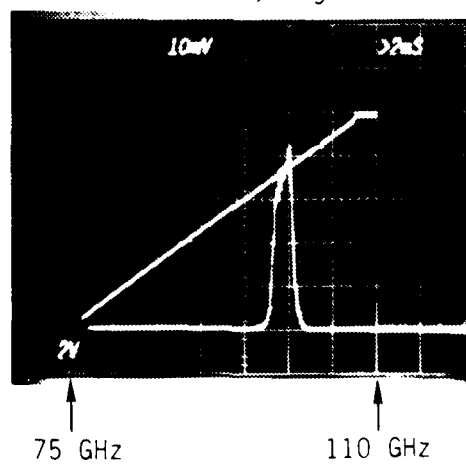
Figure 33A. Spectrometer calibration data for the W-band detectors W1-W6 (detectors
W1-W6 located at 3.0, 5.5, 8.0, 10.2, 13.0, and 15.5 inch, respectively)
taken at a 46 degree grating angle.

Detector #W4, Angle 46

75 GHz   110 GHz

Detector #W5, Angle 46

75 GHz   110 GHz

Detector #W6, Angle 46

75 GHz   110 GHz

Detector #W6, Noise Only

75 GHz   110 GHz
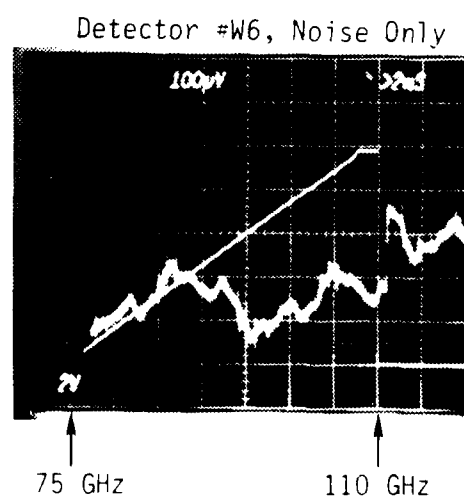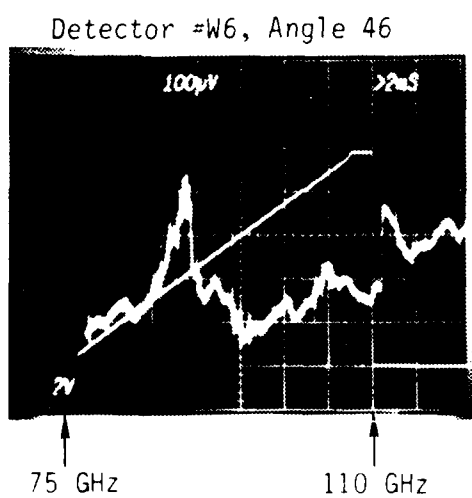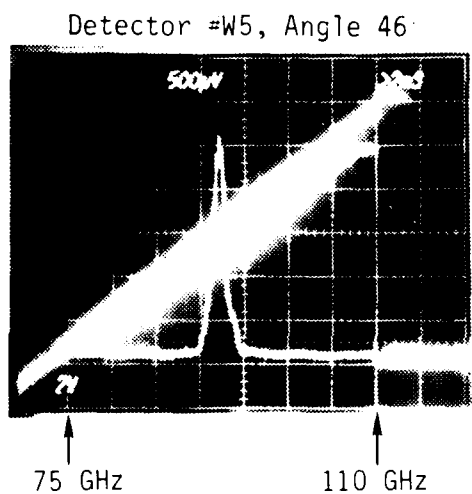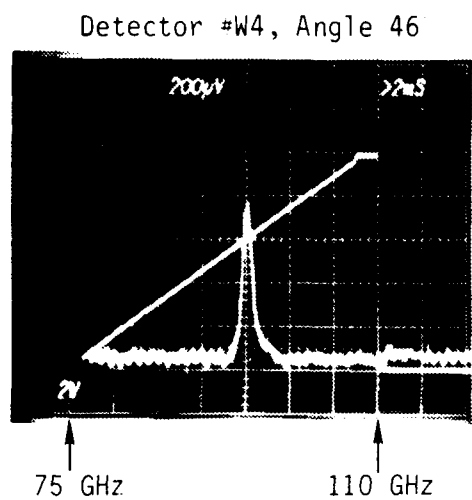
Figure 33B. Spectrometer calibration data for the W-band detectors W1-W6 (detectors W1-W6 located at 3.0, 5.5, 8.0, 10.2, 13.0, and 15.5 inch, respectively) taken at a 46 degree grating angle. Left photo is signal plus noise, right photo is noise only, taken with microwave absorbing material covering the detector.

64

Detector #W1, Angle 49°

75 GHz   110 GHz

Detector #W2, Angle 49°

75 GHz   110 GHz

Detector #W2, Noise Only

75 GHz   110 GHz

Detector #W3, Angle 49

75 GHz   110 GHz

Detector #W3, Noise Only

75 GHz   110 GHz
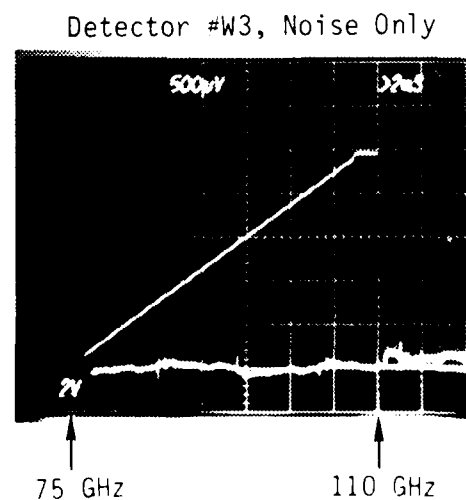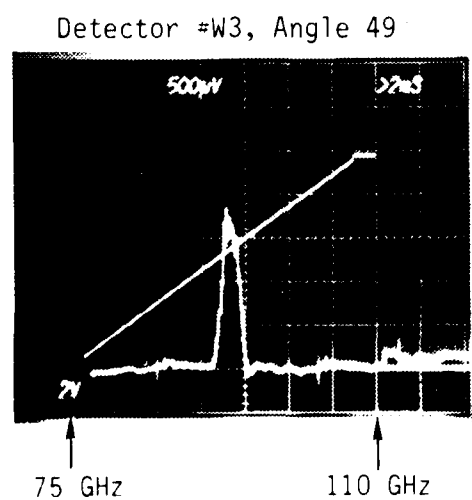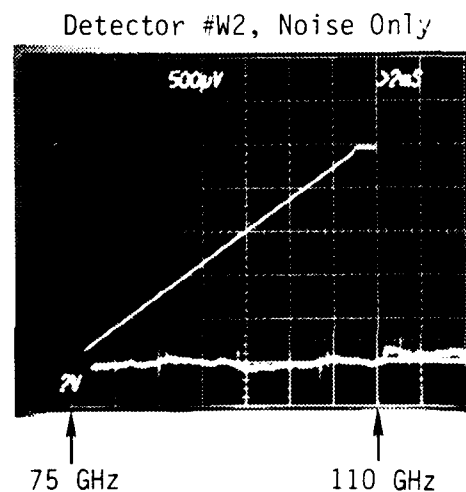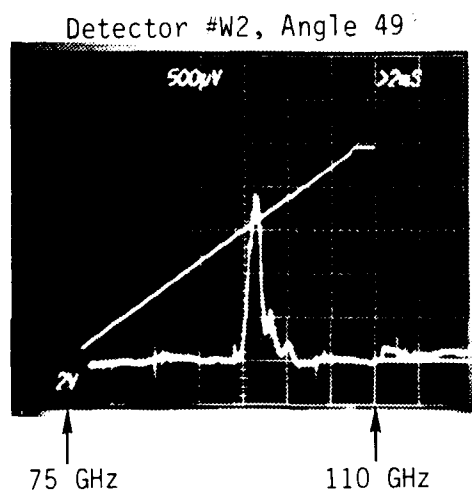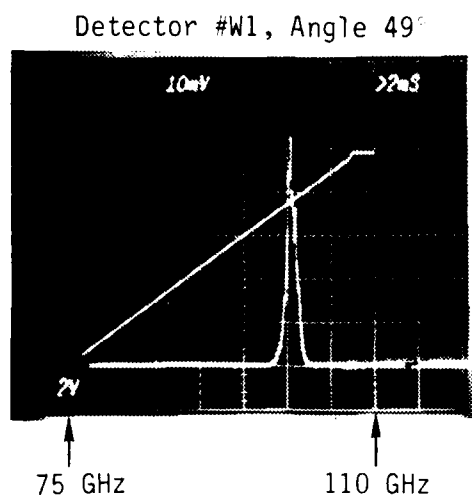
Figure 34A. Spectrometer calibration data for the W-band detectors W1-W6 (detectors W1-W6 located at 3.0, 5.5, 8.0, 10.2, 13.0, and 15.5 inch, respectively) taken at a 49 degree grating angle. Left photo is signal plus noise, right photo is noise only, taken with microwave absorbing material covering the detector.

65

Detector #W4, Angle 49   Detector #W4, Noise Only

75 GHz   110 GHz   75 GHz   110 GHz

Detector #W5, Angle 49   Detector #W5, Noise Only

75 GHz   110 GHz   75 GHz   110 GHz

Detector #W6, Angle 49   Detector #W6, Noise Only

75 GHz   110 GHz   75 GHz   110 GHz
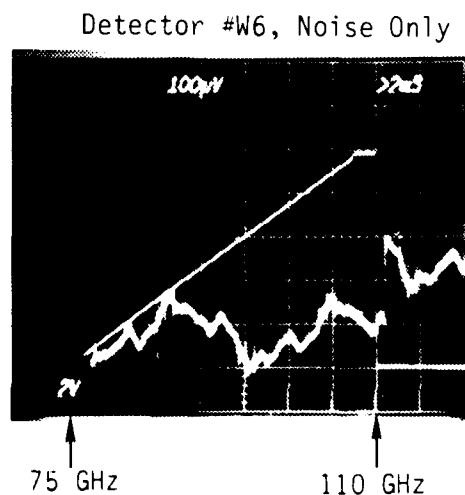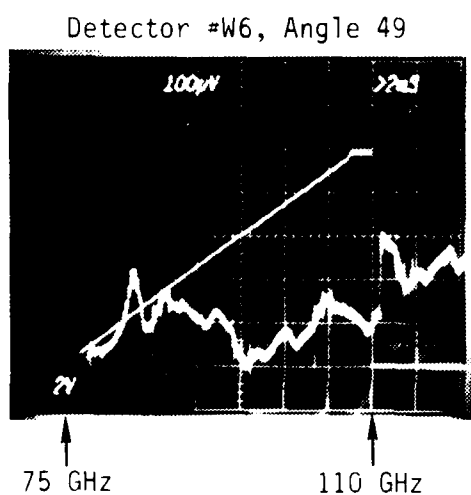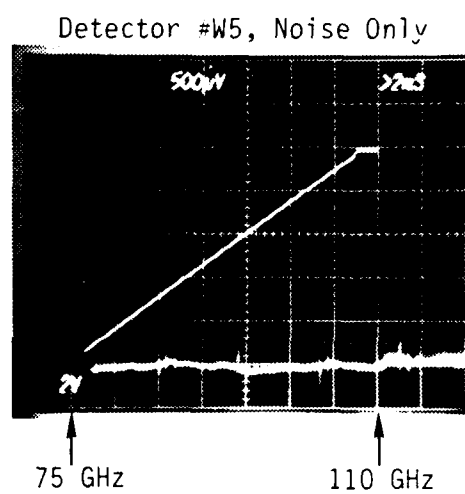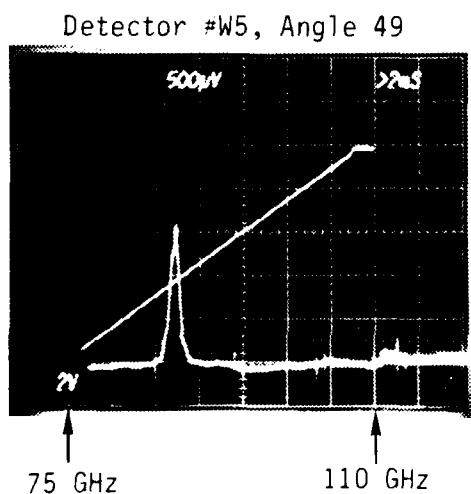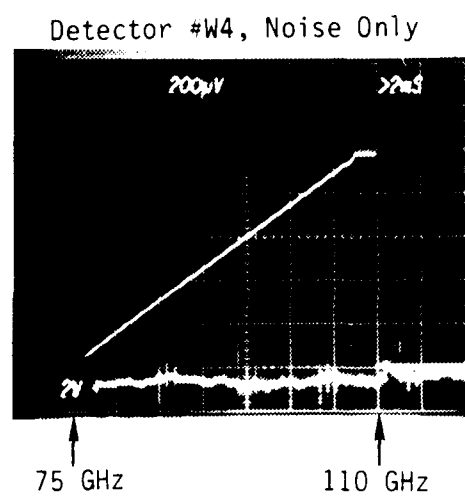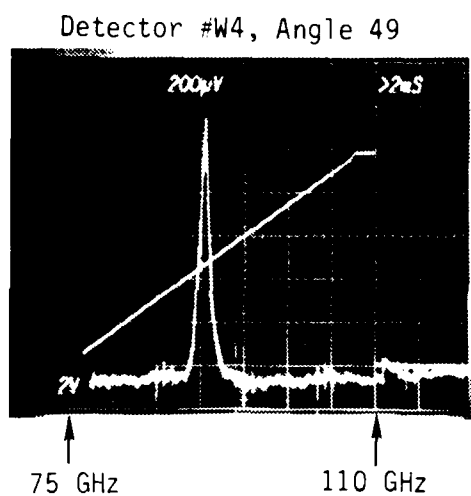
Figure 34B. Spectrometer calibration data for the W-band detectors W1-W6 (detectors W1-W6 located at 3.0, 5.5, 8.0, 10.2, 13.0, and 15.5 inch, respectively) taken at a 49 degree grating angle. Left photo is signal plus noise, right photo is noise only, taken with microwave absorbing material covering the detector.

66

Detector #W1, Angle 51.5   Detector #W1, Noise Only

75 GHz   110 GHz   75 GHz   110 GHz

Detector #W2, Angle 51.5   Detector #W2, Noise Only

75 GHz   110 GHz   75 GHz   110 GHz

Detector #W3, Angle 51.5   Detector #W3, Noise Only

75 GHz   110 GHz   75 GHz   110 GHz
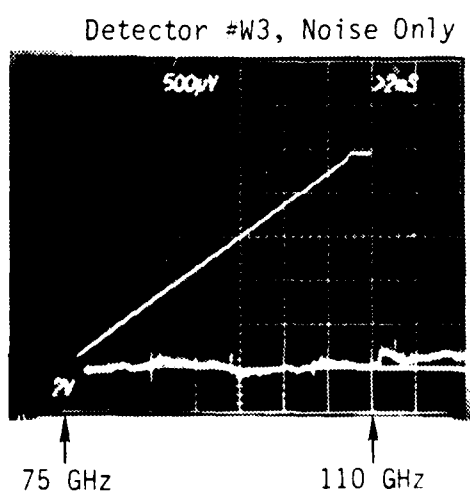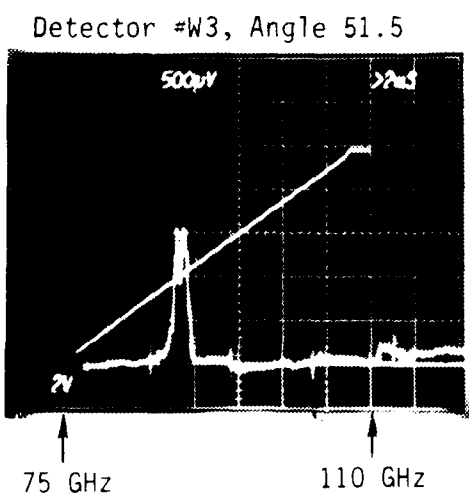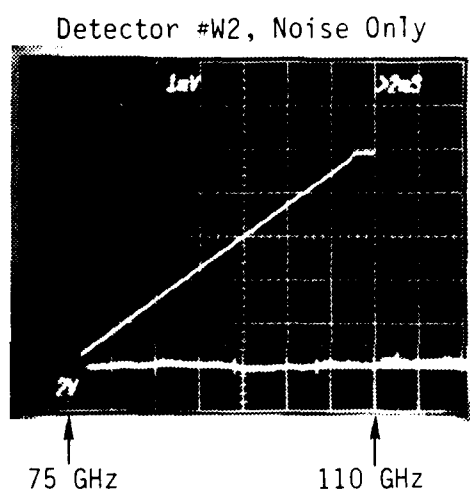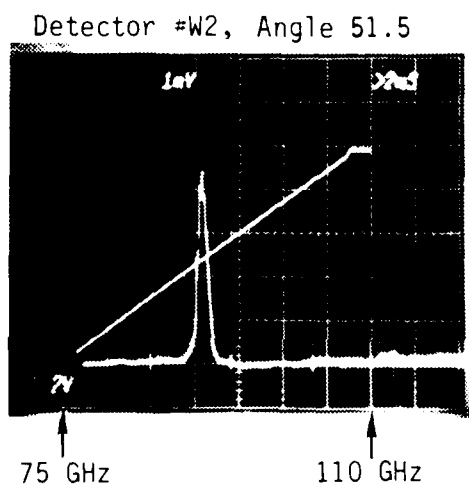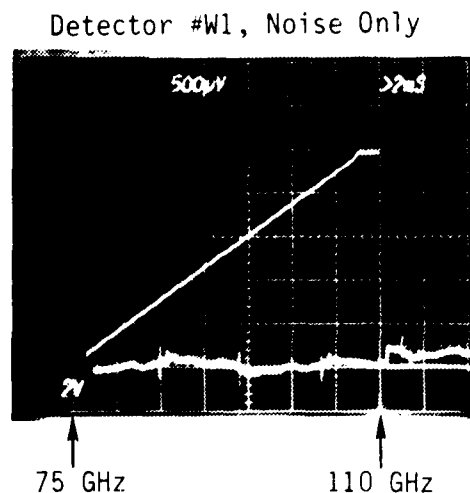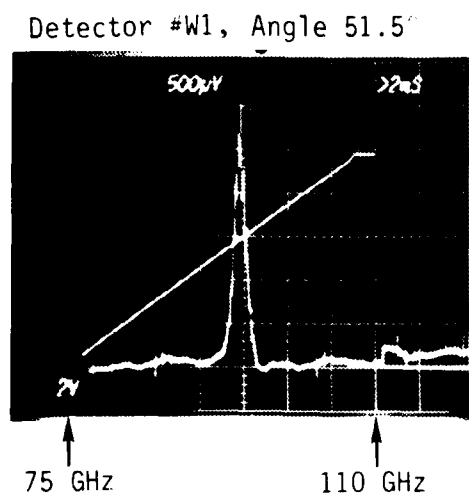
Figure 35A. Spectrometer calibration data for the W-band detectors W1-W6 (detectors W1-W6 located at 3.0, 5.5, 8.0, 10.2, 13.0, and 15.5 inch, respectively) taken at a 51.5 degree grating angle. Left photo is signal plus noise, right photo is noise only, taken with microwave absorbing material covering the detector.

67

Detector #W4, Angle 51.5   Detector #W4, Noise Only

Detector #W5, Angle 51.5   Detector #W5, Noise Only

Detector #W6, Angle 51.5   Detector #W6, Noise Only
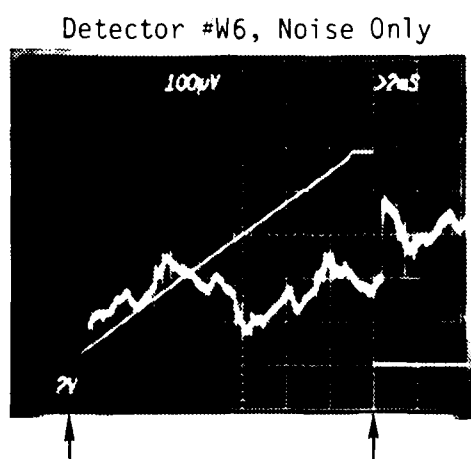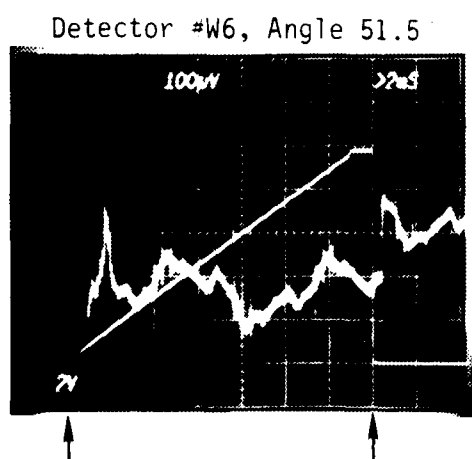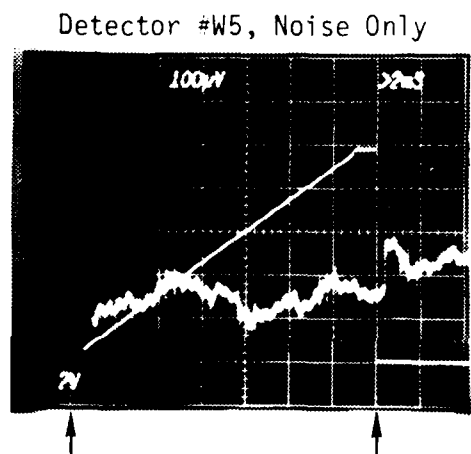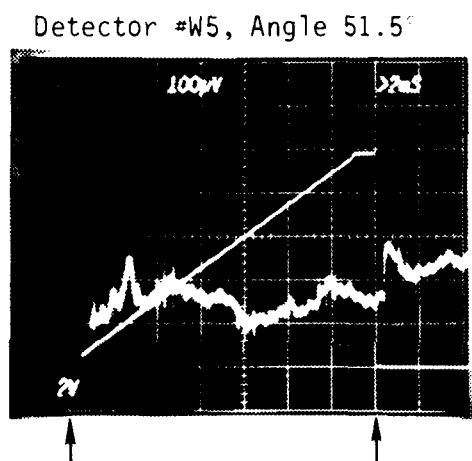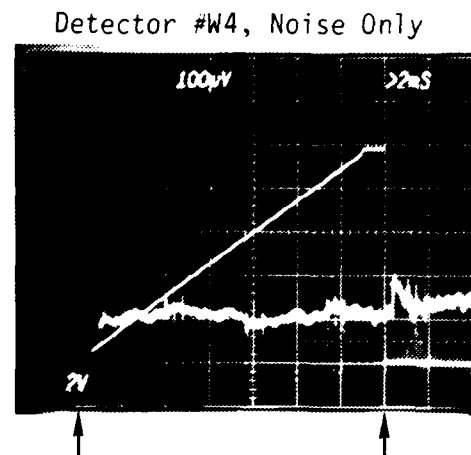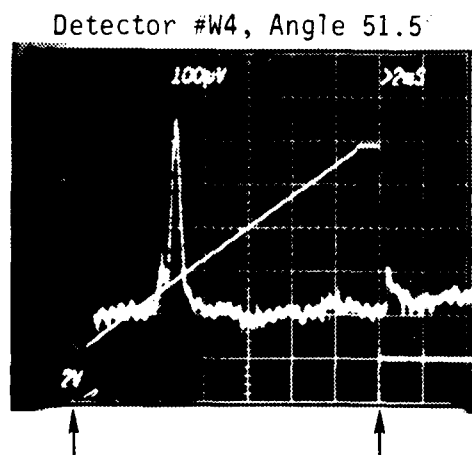
Figure 35B.   Spectrometer calibration data for the W-band detectors W1-W6 (detectors W1-W6 located at 3.0, 5.5, 8.0, 10.2, 13.0, and 15.5 inch, respectively) taken at a 51.5 degree grating angle. Left photo is signal plus noise, right photo is noise only, taken with microwave absorbing material covering the detector.

68

TABLE V. SUMMARY OF SPECTROMETER W-BAND (75-110 GHz) CALIBRATION DATA

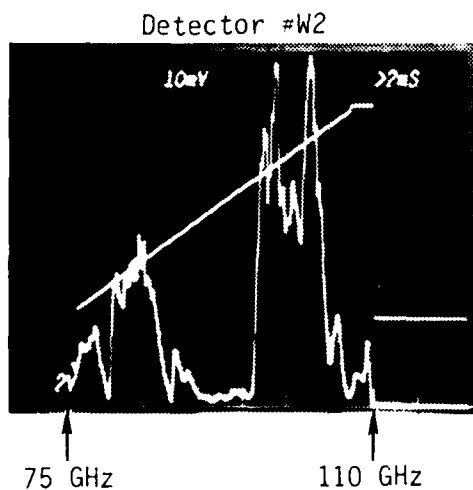| PARAMETER	Detector W1	Detector W2	Detector W3	Detector W4	Detector W5	Detector W6
Detector Position (Inches)	3.0	5.5	8.0	10.2	13.0	15.5
For 44° Grating Angle:						
Center Frequency For Peak Sensitivity (GHz)	-	109.5	105.9	-	-	88
Output Voltage (mV)	-	5.35	29	-	-	0.16
Horn Gain (db)	-	25.2	25.2	-	-	24.8
Input Power (mW)	-	46	61	-	-	30
Calculated Figure of Merit (Volts/Watt)	-	3.90×10^{-4}	1.60×10^{-3}	-	-	1.96×10^{-5}
For 46° Grating Angle:						
Center Frequency For Peak Sensitivity (GHz)	107.3	103.7	99.2	95.2	92.2	88.2
Output Voltage (mV)	1.7	41	41	0.68	2.9	0.17
Horn Gain (db)	25.2	25.2	25.1	25.0	24.9	24.8
Input Power (mW)	59	36	46	46	32	26
Calculated Figure of Merit (Volts/Watt)	9.67×10^{-5}	3.82×10^{-3}	3.06×10^{-3}	5.19×10^{-5}	3.26×10^{-4}	2.41×10^{-5}
For 49° Grating Angle:						
Center Frequency For Peak Sensitivity (GHz)	100.4	96.3	92.8	90.4	87.1	82.7
Output Voltage (mV)	51.5	1.92	1.75	1.37	1.53	0.14
Horn Gain (db)	25.1	25.0	24.9	24.8	24.7	24.5
Input Power (mW)	53	46	34	30	30	22
Calculated Figure of Merit (Volts/Watt)	3.34×10^{-3}	1.47×10^{-4}	1.85×10^{-4}	1.68×10^{-4}	1.92×10^{-4}	2.51×10^{-5}
For 51.5° Grating Angle:						
Center Frequency For Peak Sensitivity (GHz)	94.6	90.7	88.2	86.7	81.8	79.4
Output Voltage (mV)	2.95	4.3	1.5	0.43	0.09	0.22
Horn Gain (db)	25.0	24.9	24.8	24.7	24.5	24.4
Input Power (mW)	37.5	28	26	29	19	17
Calculated Figure of Merit (Volts/Watt)	2.76×10^{-4}	5.52×10^{-4}	2.12×10^{-4}	5.58×10^{-5}	1.87×10^{-5}	5.22×10^{-5}

SECTION IV
ELECTRON BEAM SOURCE

The design of the pulse power system which drives the vircator e-beam diode has been previously described.[11] A schematic of the electrical system is shown in Figure 36. Briefly, the electrical equivalent of a Blumlein type pulse forming line (PFL) is built from discrete capacitors and inductors. The Blumlein is DC charged to nominally 50 kV, and the PFL is erected by a triggered spark gap switch which is driven by a time delay generator. The purpose of the time delay generator is to trigger the e-beam near peak magnetic field time, which is typically 600 μsec after the magnet circuit is fired. The artificial Blumlein, as built inside a high voltage insulated screen box, together with the charging and control components, is shown in Photo 4. A 3 cm diameter, 50 ohm high voltage cable connects the Blumlein source output to the vircator vacuum vessel shown in Photo 5.

An important consideration in the vircator diode development work has been to find a material which exhibits fast electron field emission turn on and slow gap closure. The gap closure problem is severe because the low vircator voltage requires operation at very small anode-cathode gaps, of order a few mm, in order to reach the threshold electric fields for field emission. Carbon has been tried as the cathode material because of its well-known low threshold for field emission, of order 50 kV/cm. However, the resulting slow turn on, spotty emission, and high gap closure rate (several cm/μsec) made carbon unacceptable for the cathode material.

An acceptable cathode material developed in the course of this work is the cloth fiber array. It has shown fast turn-on, as well as, very slow gap closure rates, less than 1 cm/μsec. A typical voltage and current trace for the cloth fiber array is shown in Figure 37. This data was taken
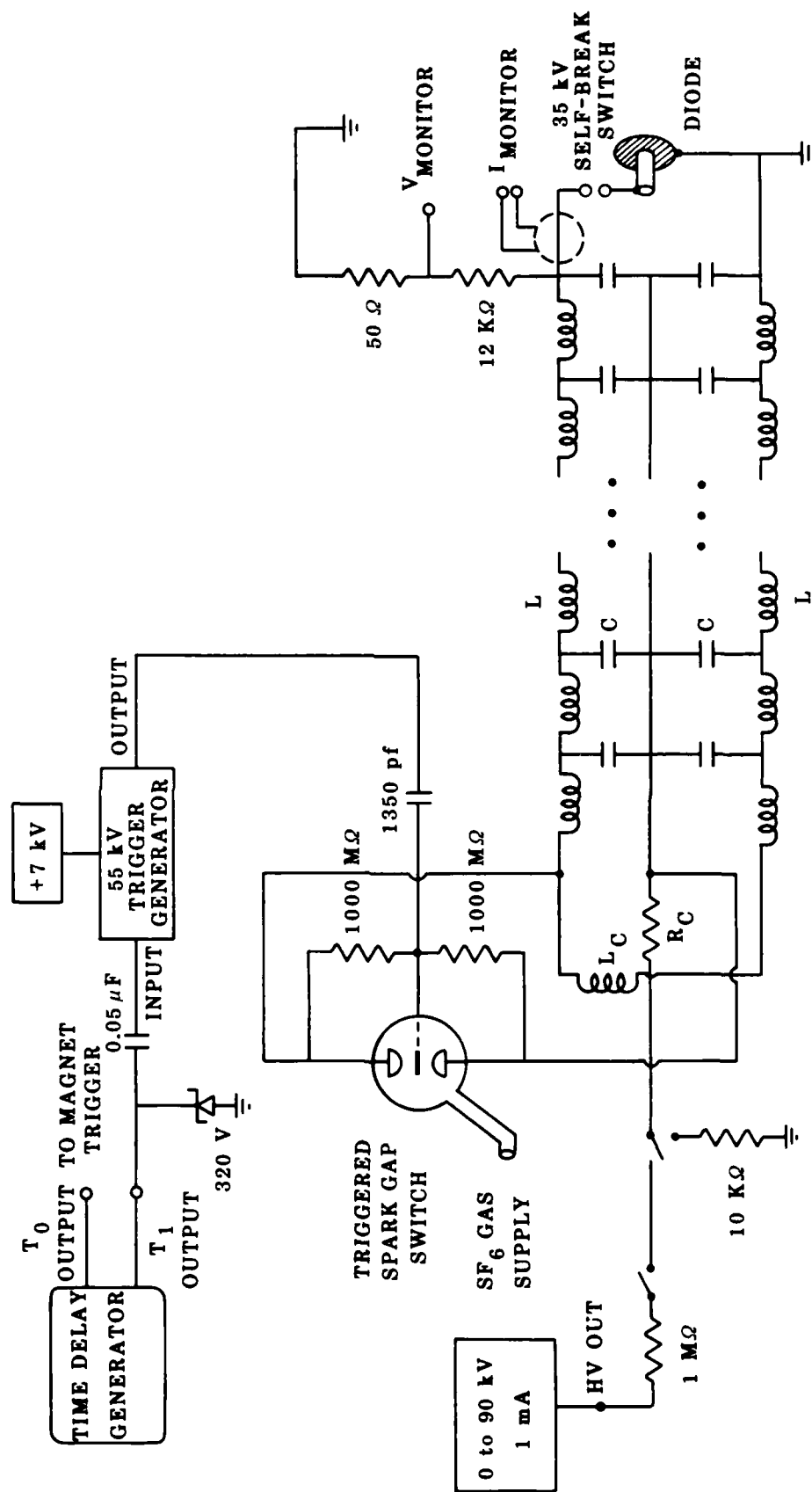
Figure 36. Schematic of the lumped element Blumlein pulse-forming line. Eight stages are used to give a pulse length of 600 nsec at a 50 ohm impedance.
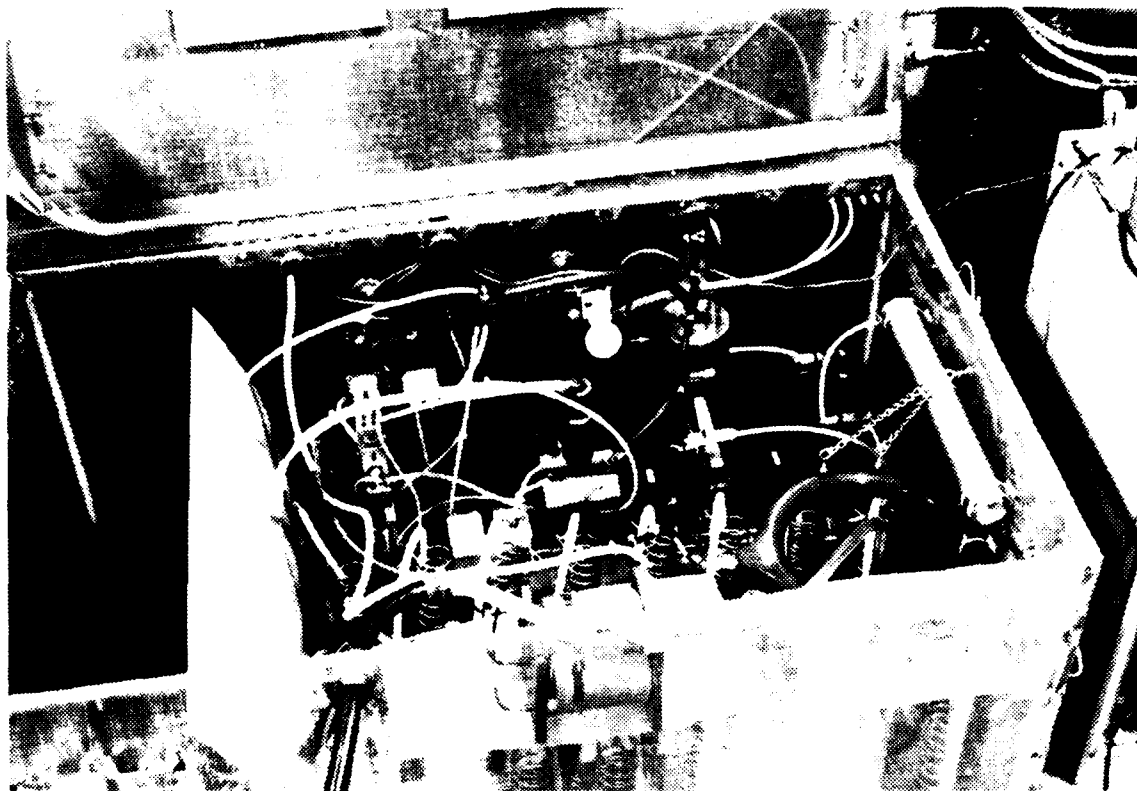
Photograph 4. The 8 stage artificial Blumlein is shown inside the high
voltage insulated screen box, together with charging and
triggering circuitry. The 16 inductors, oriented vertically,
are clearly visible. The 48 2700 pf, 40 kV rated button
capacitors, stacked in sets of 3 each located under the
white polyethylene insulation, are not visible.
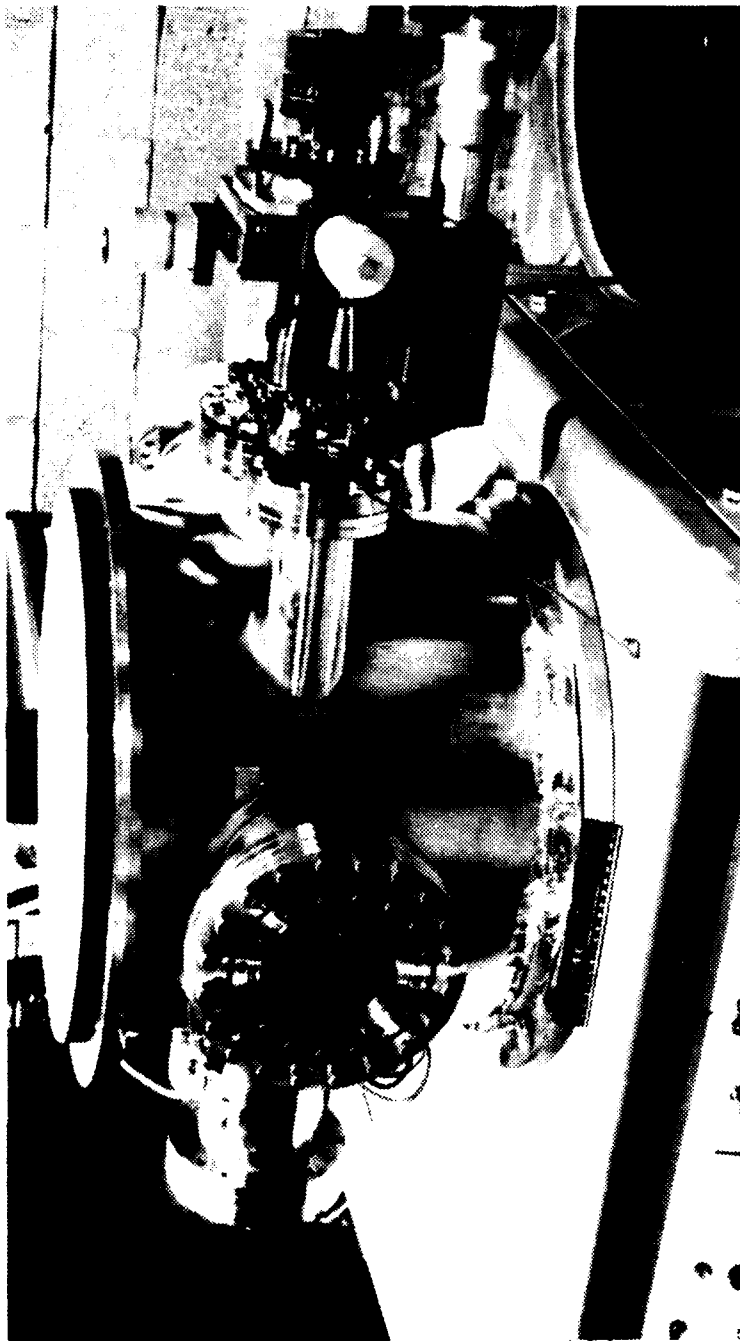
Photograph 5. Vircator vacuum vessel. The 5 degree of freedom external manipulator allowing anode-cathode gap adjustment without breaking vacuum is shown mounted on the 6 inch diameter flange at the right. Microwave emission is through the 4 inch open hole at the left. The 50Ω cable connecting the e-beam pulser to the vacuum vessel is not visible.
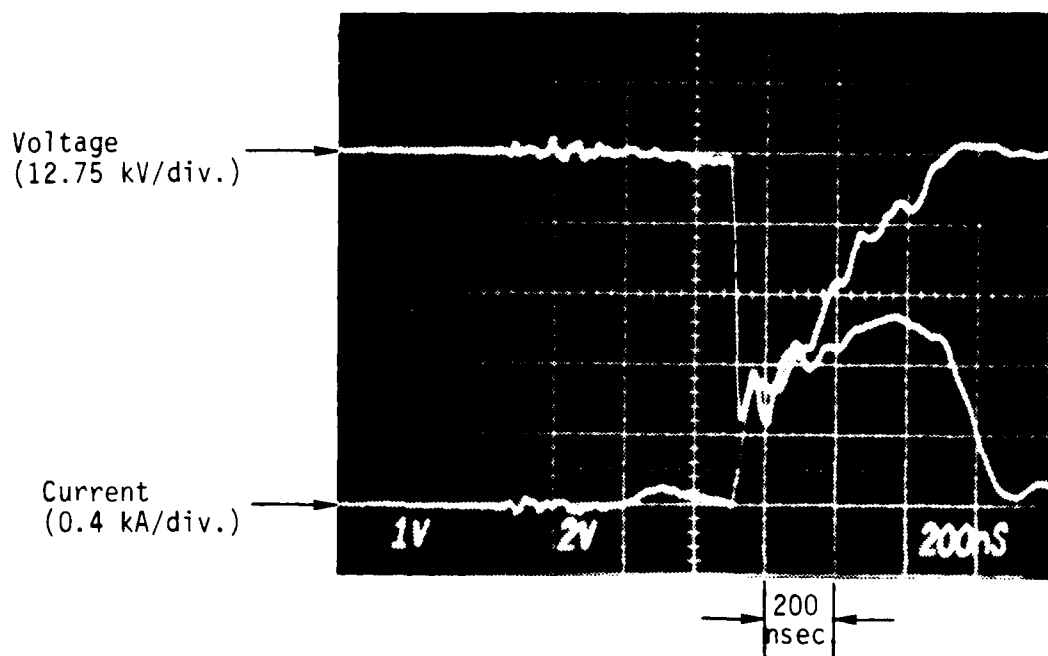
Figure 37. Voltage and current traces for a 50 kV charge voltage and a 4 mm A-K gap. Voltage risetime is 20 nsec. Peak voltage and currents are 45 kV and 1.07 kA, respectively.

74

with a 1.9 cm diameter-cathode, a grid type anode, and a 4 mm anode-cathode gap operating as a standard planar diode. Emission is within a factor of 20% of the space-charge limit. Note that the current turns on as fast as the voltage, approximately 20 nanoseconds, and that the gap stays open for essentially the entire pulse length, 0.6 μsec. These characteristics make the cloth fiber array the favored choice for the vircator cathode relative to the other cold cathode emitters.

Examination of the cloth fiber array with an optical microscope shows that it is composed of a regular array of approximately 3600 nonconducting thin fibers per cm^2 with the fibers oriented perpendicular to a partially transparent nonconducting cloth backing.[12] The emission region then consists of an array of fibers perpendicular to a conducting cathode surface. A surface flashover along the individual fibers contributes to the plasma formation process, and this apparently results in the formation of more emission sites than for the analogous carbon cold cathode. Both long lifetime and the low gap closure velocity are the result of reduced energy per emission site. The amount of energy per site is very small, because the breakdown mechanism is effectively a capacitive discharge of low capacitance. In this sense we believe that the cloth fiber array acts like the Corona electron source developed by Helionetics[13] for laser pre-ionization. The axial surface flashover mechanism is more desirable than the conventional cold cathode emission process, because production of plasma in this manner inhibits the formation of surface cathode spots.

75

REFERENCES

1. W. R. Smythe, <u>Static and Dynamic Electricity</u>, McGraw-Hill, New York (1950).

2. J. R. Freeman, <u>Controlling Magnetic Field Properties</u>, Sandia National Laboratories technical report SAND-79-0678, April 1979.

3. Berni Adler, ed., <u>Methods in Computational Physics, Volume 9</u>, Academic Press, New York (1970).

4. D. Bruce Montgomery, <u>Solenoid Magnet Design</u>, Wiley, New York (1969), p. 233.

5. M. W. Garrett, J. Appl. Phys. <u>22</u>, 1091 (1951).

6. M. W. Garrett, <u>High Magnetic Fields</u>, Chapter 2, MIT Press, Cambridge, Mass. (1962).

7. D. B. Montgomery and J. Terrel, <u>Some Useful Information for the Design of Solenoid Magnets</u>, National Magnet Laboratory Report 1525 (1961).

8. J. D. Jackson, <u>Classical Electrodynamics</u>, Wiley, New York (1962), p. 165.

9. D. Bruce Montgomery, <u>Solenoid Magnet Design</u>, Wiley, New York (1969), p. 190.

10. W. M. Bollen and R. H. Jackson, "A W-Band Diffraction Grating Spectrometer," Mission Research Corporation, MRC/WDC-R-046, December 1982.

11. D. J. Sullivan, D. E. Voss, W. M. Bollen, R. H. Jackson, and E. A. Coutsias, "Annual Report: Virtual Cathode Theory and Design of a Millimeter Wave Vircator," Mission Research Corporation, AMRC-R-451, January 1983.

12. R. J. Adler, G. K. Kiuttu, B. E. Simpkins, D. J. Sullivan, and D. E. Voss, "Improved Electron Emission by Use of a Cloth Fiber Cathode," Mission Research Corporation, AMRC-N-275, October 1984.

13. R. Sandstrom, J. I. Levatter, and J. H. Morris, <u>Proceedings of the Fourth IEEE Pulsed Power Conference</u>, Albuquerque, NM, T. H. Martin and M. F. Rose, Eds.

APPENDIX A

APPENDIX A

LISTING OF FORTRAN SOURCE CODE FOR
MAGNETIC FIELD CALCULATION

```
SOLENOIDAL MAGNETIC FIELD CALCULATION

BASE CODE BY JOHN FREEMAN, MODIFIED BY DON VOSS FOR FIELD LINE
CALCULATION.

      COMMON /A/ RB(50),ZB(50),RF(50),ZF(50)
      COMMON /B/ RCC(100),ZCL(100),ZCR(100),X  C(100),CCC(100)
      COMMON /VOSS1/ BRAD(41, 201), BAXIAL(41, 201)
      COMMON /VOSS2/ RADIUS, XLENG, DR, DZ, DRXDZ
      DIMENSION IHEAD(7)
      DIMENSION STO(5000)
      DIMENSION XPLOT(1001), YPLOT(1001)
      COMMON /C/ R(200),Z(200),NR,NZ,NCT
      DIMENSION IPHEAD(3)
      REAL LENGTH
      DATA IPHEAD /4HBRJ=,4HBZJ=,4HPSJ=/
      OPEN (UNIT=11, NAME='MAGIN.ECH', STATUS='NEW')
      OPEN (UNIT=12, NAME='MAGOUT.LPT', STATUS='NEW')
      PI = 3.1415926535
      RADDEG = 180. / PI
      PRINT *,'ALL DIMENSIONS ARE IN CENTIMETERS'
  100 FORMAT(7A10)
      PRINT *,'ENTER HEADING FOR THIS PROBLEM'
      READ100,IHEAD
  101 FORMAT(1X,7A10//)
      PRINT *,'FOR KEYBOARD INPUT TYPE 1; OTHERWISE TYPE 0'
      READ *,INP
      PRINT *,'FOR SHORT PRINT TYPE 1;OTHERWISE TYPE 0'
      READ *,KPT
      IF (INP.EQ.0) GO TO 30
      PRINT *,'ENTER RADIUS OF COMPUTATION'
      READ *,RADIUS
      PRINT *,'ENTER LENGTH OF COMPUTATION'
      READ *,LENGTH
      PRINT *,'ENTER NUMBER OF RADIAL MESH LINES'
      READ *,NR
      PRINT *,'ENTER NUMBER OF AXIAL MESHLINES'
      READ *,NZ
      NCT=0
    2 PRINT *,'ENTER COIL IDENT NUMBER; 0 TO TERMINATE'
      READ *,NC
```

```
      PRINT *,'ENTER NUMBER OF TURNS'
      READ *, XNTC(NC)
      PRINT *,'ENTER COIL CURRENT IN AMPERES'
      READ *,CCC(NC)
      GO TO 2
   30 CONTINUE
      OPEN (UNIT=1, NAME='MAGIN.DAT', STATUS='OLD')
      READ(1,*) RADIUS
      READ(1,*) LENGTH
      READ(1,*) NR
      READ(1,*) NZ
      READ(1,*) NCT
      DO 32 I=1, NCT
      READ(1,*) RCC(I), ZCL(I), ZCR(I), XNTC(I), CCC(I)
   32 CONTINUE
    1 CONTINUE
  400 FORMAT (1X, 1PE16.8)
  401 FORMAT (1X, I6)
  402 FORMAT (1X, 5(1PE16.8))
      WRITE (11,400) RADIUS
      WRITE (11,400) LENGTH
      WRITE (11,401) NR
      WRITE (11,401) NZ
      WRITE (11,401) NCT
      DO 31 I=1, NCT
      WRITE (11,402) (RCC(I), ZCL(I), ZCR(I), XNTC(I), CCC(I))
   31 CONTINUE
      XLENG = LENGTH
      DR = 0.
      DZ = 0.
      IF (NR .EQ. 1) GO TO 9
      NR1 = NR - 1
      DR = RADIUS / NR1
      R(1) = 0.
      DO 3 I=2, NR
    3 R(I) = R(I-1) + DR
    9 IF (NZ .EQ. 1) GO TO 8
      NZ1 = NZ - 1
      DZ = LENGTH / NZ1
      Z(1) = 0.
      DO 4 I=2, NZ
    4 Z(I) = Z(I-1) + DZ
    8 CONTINUE
      DRXDZ = DR * DZ
      PRINT 201
  201 FORMAT (' COMPUTATION REGION DATA')
      PRINT 102,RADIUS,LENGTH,DR,DZ,NR,NZ
  102 FORMAT (/,' RADIUS=', 1PE12.3, 5X, 'LENGTH=', 1PE12.3, 4X,
```

```
  202 FORMAT (' COIL DATA')
      DO 5 I=1, NCT
      PRINT 103, (RCC(I), ZCL(I), ZCR(I), XNTC(I), CCC(I))
  103 FORMAT ('  RCC=', 1PE9.2, '  ZCL=', 1PE9.2,
     1            '  ZCR=', 1PE9.2, '  NTC=', 1PE9.2, '  CCC=', 1PE9.2)
    5 CONTINUE
      IF (KPT .EQ. 1) GO TO 33
      PRINT 105
  105 FORMAT(/, ' RADIAL MESH LINE LOCATIONS')
      PRINT 104, (R(I), I=1, NR)
      PRINT 106
  106 FORMAT (/, ' AXIAL MESH LINE LOCATIONS')
      PRINT 104, (Z(I), I=1, NZ)
  104 FORMAT ((10(5(1PE13.5)/)))/)
   33 CONTINUE
      WRITE (12, 201)
      WRITE (12, 102) RADIUS, LENGTH, DR, DZ, NR, NZ
      WRITE (12, 202)
      DO 250 I=1, NCT
  250 WRITE (12, 103) RCC(I), ZCL(I), ZCR(I), XNTC(I), CCC(I)
      WRITE (12, 105)
      WRITE (12, 104) (R(I), I=1, NR)
      WRITE (12, 106)
      WRITE (12, 104) (Z(I), I=1, NZ)
      NT = NR * NZ
      PRINT *, ' ENTER -2 TO BYPASS, -1 FOR BR, 0 FOR BZ, 1 FOR PSI'
      READ *, IFIELD
      IF (IFIELD .LE. -2) GO TO 16
      CALL FIELD (STO, IFIELD)
   17 PRINT *, ' ENTER J-LINE FOR PRINT; 0 TO TERMINATE'
      IPT = IFIELD + 2
      READ *, J
      IF (J .EQ. 0) GO TO 16
      PRINT 108, IPHEAD(IPT), J
  108 FORMAT (//1X, A7, I3)
      DO  7 L=1, NZ
      JL = (L-1) * NR + J
    7 RB(L) = STO(JL)
      PRINT 104, (RB(L), L=1, NZ)
      GO TO 17
   16 CONTINUE
      WRITE (6, 300)
  300 FORMAT (/, ' TYPE A 1 IF YOU WANT TO DO FIELD LINES')
      READ (5, 301) IFLINE
  301 FORMAT (I2)
      IF (IFLINE .EQ. 0) GO TO 399
      IFIELD = -1
      CALL FIELD (STO, IFIELD)
```

```
      JL = (L - 1) * NR + K
      BRAD(K,L) = STO(JL)
364 CONTINUE
365 CONTINUE
      IFIELD = 0
      CALL FIELD (STO, IFIELD)
      DO 367 K=1, NR
      DO 366 L=1, NZ
      JL = (L - 1) * NR + K
      BAXIAL(K,L) = STO(JL)
366 CONTINUE
367 CONTINUE
      WRITE (12, 305)
305 FORMAT (//, ' LISTING OF BR AND BZ OVER THE COMPUTATIONAL GRID')
      DO 369 K=1, NR
      WRITE (12, 306)
306 FORMAT (/,'  K', 3X, 'L', 5X, 'R', 9X, 'Z', 6X, 'BR(K,L)', 4X,
    1          'BZ(K,L)', 4X, 'B(K,L)', 5X, 'BR/BZ', 5X, 'THETA')
      XKV = K - 1
      RADV = XKV * DR
      DO 368 L=1, NZ
      XLV = L - 1
      ZV = XLV * DZ
      RCOMP = BRAD(K,L)
      ZCOMP = BAXIAL(K,L)
      BMAG = SQRT (RCOMP * RCOMP + ZCOMP * ZCOMP)
      BRATIO = 0.
      IF (ZCOMP .NE. 0.) BRATIO = RCOMP / ZCOMP
      ANGV = RADDEG * ATAN(BRATIO)
      WRITE (12, 307)  K, L, RADV, ZV, RCOMP, ZCOMP, BMAG, BRATIO, ANGV
307 FORMAT (1X, I2, I4, F9.5, F9.4, 3F11.3, 1X, 1PE10.3, 0PF9.4)
368 CONTINUE
369 CONTINUE

      READ DATA FOR FIELD LINE CALCULATION

380 WRITE (6, 500)
500 FORMAT (' ENTER A 1 FOR FIELD LINE TTY INPUT, 0 FOR DISK INPUT,',
    1          ' -1 TO TERM -- ', $)
      READ (5, *) IDVOPT
      IF (IDVOPT .EQ. -1) GO TO 590
      IF (IDVOPT .EQ. 0) GO TO 555
550 WRITE (6, 501)
501 FORMAT (' HOW MANY FIELD LINES (MAX = 20) -- ', $)
      READ (5, *) IFLNUM
      IF (IFLNUM .LE. 0) GO TO 550
552 WRITE (6, 502)
502 FORMAT (' ENTER FIELD LINE STEP DISTANCE DS (CM) -- ', $)
```

```
    553 WRITE (6, 503)
    503 FORMAT (' ENTER PLOT SPACING DISTANCE DPLOT (CM) -- ', $)
        READ (5, *) DPLOT
        IF (DPLOT .LT. 0.) GO TO 553
    554 WRITE (6, 504)
    504 FORMAT (' ENTER RADIAL RANGE (2 NUMBERS) FOR FIELD LINES (CM) -- '
       1          , $)
        READ (5, *) RFLBEG, RFLEND
        IF (RFLBEG .GT. RFLEND) GO TO 554
    567 WRITE (6, 517)
    517 FORMAT (' ENTER RADIAL GRAPHICS ENHANCEMENT FACTOR -- ', $)
        READ (5, *) RFACT
        IF (RFACT .LE. 0.) GO TO 567
        WRITE (6, 505)
    505 FORMAT (' ENTER R AND Z DISTANCES FOR PLOT WINDOW',
       1          ' (2 NUMBERS) -- ', $)
        READ (5, *) RPLOTW, ZPLOTW
        GO TO 556
    555 CONTINUE
        READ (1, *) IFLNUM
        READ (1, *) DS
        READ (1, *) DPLOT
        READ (1, *) RFLBEG, RFLEND
        READ (1, *) RFACT
        READ (1, *) RPLOTW, ZPLOTW
    556 CONTINUE
        WRITE (12, 510) IFLNUM, DS, RFLBEG, RFLEND, DPLOT
    510 FORMAT (//, '    FIELD LINE PLOT SPECIFICATIONS AS FOLLOWS:', /,
       1          1X, I2, ' FIELD LINES CALCULATED WITH DS =', 1PE14.7,
       2          ' CM,',/, ' BEGINNING AT A RADIUS OF', OPF10.6, ' CM AND',
       3          /, ' ENDING AT A RADIUS OF', OPF10.6, ' CM.  FIELD LINE',
       4          /, ' (R,Z) POSITIONS RECORDED AT INTERVALS OF', OPF10.6,
       5          ' CM.')
        IF (RPLOTW .GT. 0.) GO TO 570
        RPLOTW = RADIUS
        DO 569 IDUM=1, NCT
        IF (RCC(IDUM) .GT. RPLOTW) RPLOTW = RCC(IDUM)
    569 CONTINUE
    570 IF (ZPLOTW .GT. 0.) GO TO 572
        ZPLOTW = XLENG
        DO 571 IDUM=1, NCT
        IF (ZCR(IDUM) .GT. ZPLOTW) ZPLOTW = ZCR(IDUM)
    571 CONTINUE
    572 WRITE (12, 523) RFACT, RPLOTW, ZPLOTW
    523 FORMAT (' RADIAL SCALE ON PLOTS ENHANCED BY', 1PE14.7, /,
       1          ' (R,Z) PLOT RANGE = (', OPF9.5, ',', OPF9.5, ').')
        WRITE (6, 510) IFLNUM, DS, RFLBEG, RFLEND, DPLOT
        WRITE (6, 523) RFACT, RPLOTW, ZPLOTW
```

```
       WRITE (11, 400) DPLOT
       WRITE (11, 402) RFLBEG, RFLEND
       WRITE (11, 400) RFACT
       WRITE (11, 402) RPLOTW, ZPLOTW

       START FIELD LINES AT Z=0 AND USE 'SHOOTING' TECHNIQUE FOR INTEGRATING

       DRFL = 0.
       XFLNUM = IFLNUM
       IF (IFLNUM .GT. 1) DRFL = (RFLEND - RFLBEG) / (XFLNUM - 1.)

       PLOT SET-UP --- PLOT AXES AND LABELS --- 11-30-82

       XPLOT(1) = 0.
       YPLOT(1) = 0.
       XPLOT(2) = ZPLOTW
       YPLOT(2) = RPLOTW
       RADEFF = RPLOTW * RFACT
       CALL STARTT(1)
       CALL PLOJB (XPLOT, YPLOT, 2, 1, 0, 0, 0.0, ZPLOTW,
     1          RADEFF,37H VIRCATOR VACUUM FIELD LINE STRUCTURE,
     2          -37,25H AXIAL CO-ORDINATE Z (CM),
     3          25, 2H R, 2)

       DO 560 IDUM=1, IFLNUM
       XDUM = IDUM - 1
       RSTART = RFLBEG + XDUM * DRFL
       ZSTART = 0.
       WRITE (12, 511) IDUM
 511 FORMAT (//, ' FIELD LINE NUMBER', I4, ' (R,Z) TRAJECTORY IS AS'
     1          ' FOLLOWS :')
       WRITE (12, 512)
 512 FORMAT (/,' STEP #', 5X, 'R', 9X, 'Z', 6X, 'BR(K,L)', 4X,
     1          'BZ(K,L)', 4X, 'B(K,L)', 5X, 'BR/BZ', 5X, 'THETA')
       DISTDV = DPLOT
       INC = 0
       DO 559 IDV=1, 10001
       CALL BINTRP (RSTART, ZSTART, BRINT, BZINT, IOFF)
       IF (IOFF .EQ. 1) GO TO 559
       BMAG = SQRT (BRINT * BRINT + BZINT * BZINT)
       IF (DISTDV .LT. DPLOT) GO TO 566
       BRATIO = 0.
       IF (BZINT .NE. 0.) BRATIO = BRINT / BZINT
       ANGV = RADDEG * ATAN (BRATIO)
       WRITE (12, 513) IDV, RSTART, ZSTART, BRINT, BZINT, BMAG, BRATIO,
     1                 ANGV
 513 FORMAT (1X, I6, F9.5, F9.4, 3F11.3, 1X, 1PE10.3, OPF9.4)
       DISTDV = DISTDV - DPLOT
```

```
      YPLOT(INC) = RSTART
566 IF (BMAG .GT. 0.) GO TO 557
    WRITE (12, 515)
515 FORMAT (' RUN TERMINATED DUE TO ZERO B FIELD')
    GO TO 561
557 FACDV = DS / BMAG
    RSTART = RSTART + BRINT * FACDV
    IF (RSTART .GT. 0.) GO TO 558
    WRITE (12, 514)
514 FORMAT (' RUN TERMINATED DUE TO PROJECTION THROUGH ZERO RADIUS')
    GO TO 561
558 ZSTART = ZSTART + BZINT * FACDV
    DISTDV = DISTDV + DS
559 CONTINUE
561 IF (INC .LE. 1) GO TO 560

    PLOT THE FIELD LINE JUST CALCULATED

    CALL CHOPAR (XPLOT, YPLOT, INC, ZPLOTW, RPLOTW)
    CALL PLOJB (XPLOT, YPLOT, INC, 1, 0, -1, 0.0, ZPLOTW, RADEFF,
   1            0, 0, 0, 0, 0, 0)

560 CONTINUE
399 CONTINUE

    PLOT THE POSITION OF EACH TURN OF THE COIL SET

    DO 575 IDV=1, NCT
    INC = XNTC(IDV)
    XPLOT(1) = ZCL(IDV)
    YPLOT(1) = RCC(IDV)
    IF (INC .EQ. 1) GO TO 574
    DXCOIL = (ZCR(IDV) - ZCL(IDV)) / (XNTC(IDV) - 1.)
    DO 573 IDUM=2, INC
    XDUM1 = IDUM - 1
    XPLOT(IDUM) = ZCL(IDV) + XDUM1 * DXCOIL
573 YPLOT(IDUM) = RCC(IDV)
574 ICHARP = - IDV
    CALL CHOPAR (XPLOT, YPLOT, INC, ZPLOTW, RPLOTW)
    CALL PLOJB (XPLOT, YPLOT, INC, 1, -1, ICHARP, 0.0,
   1            ZPLOTW, RADEFF, 0, 0, 0, 0, 0, 0)
575 CONTINUE

    MAKE HARDCOPY OF PLOT AND RELEASE PLOTTER

    CALL HDCOPY
    CALL STOPT
```

```
      READ *, ICORR
      IF (ICORR .EQ. 0) GO TO 20
      PRINT *,'FIELD CORRECTION FOR BZ ONLY'
      CALL ECORR(STO)
      CALL FIELD(STO,IFIELD)
21 PRINT *,'ENTER J-LINE FOR PRINT; 0 TO TERMINATE'
      READ *,J
      IF(J.EQ.0) GO TO 22
      PRINT 108,IPHEAD(IPT),J
      DO 70 L=1,NZ
      JL=(L-1)*NR+J
70 RB(L)=STO(JL)
      PRINT 104,(RB(L),L=1,NZ)
      GO TO 21
22 CONTINUE
20 CONTINUE
      STOP
      END




      SUBROUTINE TO CHOP ARRAYS

      SUBROUTINE CHOPAR (XPLOT, YPLOT, NUM, XMAX, YMAX)
      DIMENSION XPLOT(1001), YPLOT(1001)
      DO 1 I=1, NUM
      IF (XPLOT(I) .GT. XMAX) XPLOT(I) = XMAX
      IF (YPLOT(I) .GT. YMAX) YPLOT(I) = YMAX
  1 CONTINUE
      RETURN
      END




      SUBROUTINE TO DO 2-DIMENSIONAL MAGNETIC FIELD INTERPOLATION
      D. VOSS - 11/24/82.

      SUBROUTINE BINTRP (RCOORD, ZCOORD, BRINT, BZINT, IOFF)
      COMMON /VOSS1/ BRAD(41, 201), BAXIAL(41, 201)
      COMMON /VOSS2/ RADIUS, XLENG, DR, DZ, DRXDZ
      COMMON /C/ R(200), Z(200), NR, NZ, NCT
      KUPR = (RCOORD / DR) + 2.
      LUPR = (ZCOORD / DZ) + 2.
      IF (KUPR .LE. NR .AND. LUPR .LE. NZ) GO TO 3
  1 BRINT = 0.
      BZINT = 0.
      IOFF = 1

      IOFF = 1 INDICATES THAT THE (R,Z) POINT REQUESTED IS NOT ON THE GRID

  2 RETURN
  3 IF (KUPR .LE. 1 .OR. LUPR .LE. 1) GO TO 1
```

```
      CALCULATE AREAL WEIGHTS - THIS SCHEME ACCURATE TO 2ND ORDER IN DR, DZ

      RDIST = R(KUPR) - RCOORD
      ZDIST = Z(LUPR) - ZCOORD
      DRDIST = DR - RDIST
      DZDIST = DZ - ZDIST
      WLL = RDIST * ZDIST
      WLR = RDIST * DZDIST
      WUL = DRDIST * ZDIST
      WUR = DRDIST * DZDIST
      KUPR1 = KUPR - 1
      LUPR1 = LUPR - 1
      BRINT = (BRAD(KUPR1,LUPR1) * WLL + BRAD(KUPR1,LUPR) * WLR +
     1        BRAD(KUPR,LUPR1) * WUL + BRAD(KUPR,LUPR) * WUR) / DRXDZ
      BZINT = (BAXIAL(KUPR1,LUPR1) * WLL + BAXIAL(KUPR1,LUPR) * WLR +
     1        BAXIAL(KUPR,LUPR1) * WUL + BAXIAL(KUPR,LUPR) * WUR)/DRXDZ
      GO TO 2
      END




      SUBROUTINE FIELD(STO,IFIELD)
      COMMON /B/ RCC(100), ZCL(100), ZCR(100), XNTC(100), CCC(100)
      COMMON /C/ R(200), Z(200), NR, NZ, NCT
      DIMENSION STO(1)
      REAL K,K2
      TPI=6.2831853072
      EMU=2.E-1*TPI
      NT=NR*NZ
      DO 6 I=1,NT
    6 STO(I)=0.
      DO 7 J=1,NR
      DO 7 L=1,NZ
      JL=(L-1)*NR+J
      DO 8 I=1,NCT
      IF(XNTC(I) .NE. 1.) GO TO 14
      DZC=0.
      GO TO 15
   14 DZC = (ZCR(I)-ZCL(I)) / (XNTC(I)-1)
   15 NTCPAR = XNTC(I) + .0001

      PREVIOUS STATEMENT CHANGED 11-23-82 TO FLOATING - D.V.

      DO 9 IK=1, NTCPAR
      R2=R(J)/RCC(I)
      Z2=-((ZCL(I)+(IK-1)*DZC-Z(L))/RCC(I)
      A=CCC(I)*EMU*R(J)
      A1=CCC(I)*EMU/RCC(I)
      C1=SQRT((1.+R2)**2+Z2*Z2)
      C2=(1.-R2)**2+Z2*Z2
      AK=SQRT(4.*R2)/C1
```

```fortran
  107 FORMAT (' MESH POINT COINCIDENT WITH COIL')
      K2=AK*AK
      CK2=1.-K2
      CALL CELI2(E,AK,1.,CK2,IER)
      CALL CELI2(K,AK,1.,1.,IER)
      IF(R2.NE.0.) C3=2./(TPI*AK*SQRT(R2))
      IF(IFIELD) 10,11,12
   10 BRI=-K+E*(1.+R2*R2+Z2*Z2)/C2
      IF(R2.NE.0.) BRI=A1*BRI*Z2/(TPI*R2*C1)
      IF(R2.EQ.0.) BRI=0.
      STO(JL)=STO(JL)+BRI
      GO TO 13
   11 BZI=K+E*(1.-R2*R2-Z2*Z2)/C2
      BZI=A1*BZI/(TPI*C1)
      STO(JL)=STO(JL)+BZI
      GO TO 13
   12 IF(R2.NE.0.) PSI=A*C3*((1.-.5*K2)*K-E)
      IF(R2.EQ.0.) PSI=0.
      STO(JL)=STO(JL)+PSI
   13 CONTINUE
    9 CONTINUE
    8 CONTINUE
    7 CONTINUE
      RETURN
      END



      SUBROUTINE CELI2(RES,AK,A,B,IER)
      IER=0
      CK=AK*AK
      IF(CK-1.) 7,7,5
    5 IER=1
      GO TO 100
    7 GEO=SQRT(1.-CK)
      IF(GEO) 50,10,50
   10 IF(B) 20,40,30
   20 RES=-1.E37
      GO TO 100
   30 RES=1.E37
      GO TO 100
   40 RES=A
      GO TO 100
   50 ARI=1.
      AA=A
      AN=A+B
      W=B
   60 W=W+AA*GEO
      W=W+W
      AA=AN
      AARI=ARI
```

```
       IF(AARI-GEO-1.E-4*AARI) 80,80,70
 70 GEO=SQRT(GEO*AARI)
    GEO=GEO+GEO
    GO TO 60
 80 RES=.78539816*AN/ARI
100 RETURN
    END




    SUBROUTINE ECORR(STO)
    COMMON/A/ RB(50),ZB(50),RF(50),ZF(50)
    DIMENSION STO(1),CM(100),PN(100),NRF(50),MZF(50),EHO(100)
    COMMON/B/RCC(100),ZCL(100),ZCR(100), XNTC(100),CCC(100)
    COMMON/C/R(200),Z(200),NR,NZ,NCT
    DIMENSION BE(100),EHNM(1000),IN(100),ARR(1000)
    DIMENSION BZC(100),BZA(100)
    REAL K,K2
    TPI=6.283185072
    EMU=2.E-1*TPI
    READ(2,*) ME
    DO 40 I=1,ME
    READ(2,*) NRF(I),MZF(I)
 40 CONTINUE
    DO 41 I=1,ME
    READ(2,*) EHO(I)
 41 CONTINUE
    READ(2,*) NE
    READ(2,*)CMO
    READ(2,*)PNO
    DO 42 I=1,NE
    READ(2,*) RB(I),ZB(I)
 42 CONTINUE
    DO 24 M=1,ME
    MM=MZF(M)
    NM=NRF(M)
    RF(M)=R(NM)
 24 ZF(M)=Z(MM)
    PRINT 43,CMO,PNO
 43 FORMAT(//'   CMO=',1PE13.5,'  PNO=',1PE13.5)
    DO 25 M=1,ME
 25 CM(M)=CMO
    DO 26 N=1,NE
 26 PN(N)=PNO
    PRINT 110
110 FORMAT(//'   FIELD CORRECTION PARAMETERS')
    PRINT 111,NE,ME
111 FORMAT(//,'   NE=',1I2,'   ME=',I2,'   EHO(M)=',1PE10.3)
    PRINT 112
112 FORMAT(//,' RADIAL MESHS FOR FIELD CONTROL',/)
    PRINT 113,(RF(I),I=1,ME)
```

```
114 FORMAT(//,' AXIAL MESHS FOR FIELD CONTROL',/)
    PRINT 113,(ZF(I),I=1,ME)
    PRINT 115
115 FORMAT(//10X,' CURRENT LOOPS',/,10X,'RADII',/)
    PRINT 113,(RB(I),I=1,NE)
    PRINT 116
116 FORMAT(/,10X,'AXIAL POSITION',/)
    PRINT 113,(ZB(I),I=1,NE)
    DO 27 N=1,NE
    DO 27 M=1,ME
    R2=RF(M)/RB(N)
    Z2=-(ZB(N)-ZF(M))/RB(N)
    A1=EMU/RB(N)
    C1=SQRT((1.+R2)**2+Z2*Z2)
    C2=(1.-R2)**2+Z2*Z2
    AK=SQRT(4.*R2)/C1
    IF(C2.EQ.0.) PRINT 119
119 FORMAT(' GRID POINT COINCIDENT WITH CURRENT LOOP')
    IF(C2.EQ.0.) CALL EXIT
    K2=AK*AK
    CK2=1.-K2
    CALL CELI2(E,AK,1.,CK2,IER)
    CALL CELI2(K,AK,1.,1.,IER)
    NM=(M-1)*NE+N
    EHNM(NM)=K+E*(1.-R2*R2-Z2*Z2)/C2
 27 EHNM(NM)=EHNM(NM)*A1/(TPI*C1)
    DO 28 N=1,NE
    BE(N)=0.
    DO 29 M=1,ME
    I1=NRF(M)
    J1=MZF(M)
    I1J1=(J1-1)*NR+I1
    NM=(M-1)*NE+N
 29 BE(N)=BE(N)+(EHO(M)-STO(I1J1))*EHNM(NM)*CM(M)
 28 CONTINUE
    DO 30 I=1,NE
    DO 30 J=1,NE
    IJ=(J-1)*NE+I
    ARR(IJ)=0.
    DO 31 M=1,ME
    IM=(M-1)*NE+I
    JM=(M-1)*NE+J
 31 ARR(IJ)=ARR(IJ)+EHNM(IM)*EHNM(JM)*CM(M)
 30 CONTINUE
    DO 32 I=1,NE
    II=(I-1)*NE+I
 32 ARR(II)=ARR(II)+PN(I)*RB(I)
    CALL SAXB(NE,NE,1,ARR,BE,0,IN,KER)
```

```
      IF(KER.NE.O.) CALL EXIT
      PRINT 121
12: FORMAT(////,' CORRECTION CURRENTS',/)
      PRINT 113,(BE(N),N=1,NE)
      DO 33 M=1,ME
      I1=NRF(M)
      J1=MZF(M)
      I1J1=(J1-1)*NR+I1
  33 BZC(M)=EHO(M)-STO(I1J1)
      DO 34 M=1,ME
      BZA(M)=0.
      DO 34 N=1,NE
      NM=(M-1)*NE+N
  34 BZA(M)=BZA(M)+EHNM(NM)*BE(N)
      PRINT 122
122 FORMAT(//,'   CORRECTION FIELD REQUESTED',/)
      PRINT 113,(BZC(M),M=1,ME)
      PRINT 123
123 FORMAT(//,'   ACTUAL FIELD RETURNED',/)
      PRINT 113,(BZA(M),M=1,ME)
      L=NCT
      DO 35 I=1,NE
      L=L+1
      RCC(L)=RB(I)
      ZCL(L)=ZB(I)
      ZCR(L)=ZB(I)
      CCC(L)=BE(I)
  3J XNTC(L)=1
      NCT=NCT+NE
      RETURN
      END
```

APPENDIX B

REPRINTS OF JOURNAL PUBLICATIONS BASED ON WORK
CARRIED OUT UNDER AFOSR SPONSORSHIP

SPACE-CHARGE-LIMIT INSTABILITIES IN ELECTRON BEAMS

END

FILMED

DTIC
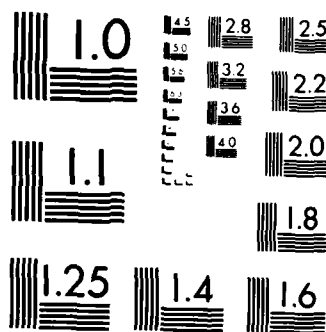
MICROCOPY RESOLUTION TEST CHART
NATIONAL BUREAU OF STANDARDS-1963-A

Space-charge-limit instabilities in electron beams

E. A. Coutsias and D. J. Sullivan*

Department of Mathematics, University of New Mexico, Albuquerque, New Mexico 87131

(Received 22 April 1982)

The method of characteristics and multiple-scaling perturbation techniques are used to study the space-charge instability of electron beams. It is found that the stable oscillating state (virtual cathode) created when the space-charge limit is exceeded is similar to a collisionless shock wave. The oscillatory solution originates at the bifurcation point of two unstable steady states. Complementary behavior (virtual anode) results when an ion beam exceeds its space-charge limit. The virtual cathode can also exist in the presence of a neutralizing heavy-ion background. The Pierce instability, where the electron and ion charge densities are equal, is a special case of this broader class. Estimates of the nonlinear growth rate of the instability at the space-charge limit are given.

I. INTRODUCTION

Since the discovery of the Child-Langmuir relation[1,2] it has been known that exceeding the limiting current of a diode leads to the development of a virtual cathode. Subsequently, numerous papers were written on experiments and theory relating to space-charge—limited flows. Reference 3 provides an excellent background and bibliography. More recently, the exact steady-state solutions for electron beams in one-dimensional relativistic diodes[4] and bounded drift spaces[5] were derived. It is easily seen that for sufficiently large currents there exist two steady states for an electron beam, only one of which is stable.[6] At the space-charge limit (SCL) these two states coalesce, and above the SCL they disappear.[7] As current is increased past the SCL, the beam develops a jump instability and relaxes into an oscillating state.

In the early 1960's, computer models were developed which quantitatively depicted the nonlinear oscillatory nature of the virtual cathode.[8-10] These were one-dimensional, nonrelativistic, electrostatic, multiple-sheet models. References 8 and 9 qualitatively pointed out many interesting dependencies of the oscillation frequency and potential minimum position on injected current, thermal spread, and circuit resistance. Reference 10 presents computer experiments with one and two species.

The phenomenon of virtual-cathode formation in intense relativistic electron beams figures prominently in a number of high-interest research areas. Devices used to produce high-current ion beams for inertial-confinement fusion—pinch reflex diodes[11,12] and reflex triodes[13,14]—depend on the virtual cathode to inhibit electron transport and use its potential well to accelerate ions. The recent concept of the spherical electron-to-ion converter[15] requires a virtual cathode.

The virtual cathode plays a dominant role in areas other than production of light-ion beams for fusion. It is attributed with the main role in collective ion acceleration in neutral gas.[16,17] Control of virtual-cathode motion is the mechanism for acceleration in the Ionization Front Accelerator.[18,19] It is also the acceleration method in two concepts for collective-effect accelerators.[20,21] A final application is the use of virtual-cathode oscillations to produce high-power short-wavelength microwaves.[22-25] Experiments using reflex triodes have already produced 1.4 GW of power with 12% beam-to-rf energy-conversion efficiency.[26]

In this paper we use multiple-scaling perturbation techniques to study the time-dependent behavior of a beam when the SCL is exceeded. We derive estimates for the nonlinear growth rate of the ensuing instability and show that even below the SCL the beam is unstable to sufficiently large perturbations. The method can be applied to a wide class of problems, but here we treat the short-circuited one-dimensional electrostatic diode depicted in Fig. 1 as the simplest model containing the appropriate physics. We show that, at least in one dimension, an arbitrary heavy-ion background does not alter the qualitative behavior of the beam and present numerical results that exhibit virtual-cathode oscillations for a neutral beam.

II. PHYSICAL DESCRIPTION

Simulations were carried out in conjunction with the theory presented in the next section using a two-dimensional, relativistic, electrostatic, particle-in-cell code. The code can solve self-consistently for the time-dependent trajectories of tens of thousands of plasma particles over thousands of plasma

FIG. 1. Schematic of the short-circuited one-dimensional electrostatic diode modeled in this study.

FIG. 2. Electrostatic potential minimum as a function of current α. Plot depicts the various possible solutions such as normal-C flow (stable), C-overlap (unstable), the partially reflected solution (unstable), and the oscillatory virtual cathode (stable). Motion around the hysteresis loop is denoted by arrows.

periods. All variables are expressed in dimensionless terms. Therefore length is in units of c/ω_p, time is measured in units of ω_p^{-1}, and particle velocity is given by

$$v_i = \beta_i \gamma \quad (i = 1, 2, 3) ,$$

where ω_p is the initial electron plasma frequency.

In these simulations a monoenergetic 51-keV electron beam is injected into a Cartesian geometry. The left and right boundaries are grounded, representing a planar short-circuited diode. Periodic boundary conditions in the transverse direction make configuration space effectively one-dimensional. In general, the simulation had 62 cells in the longitudinal direction modeling a length of $1.0c/\omega_p$. The time step was $0.0125\omega_p^{-1}$. Twenty particles were injected per cell.

A detailed discussion of the physical dynamics of the virtual cathode based on these numerical results is appropriate here. The usual graph of potential minimum ϕ_m in the diode versus electron-beam current α is shown in Fig. 2. The parameter α will be discussed later. When α is increased above the space-charge limit, ϕ_m jumps from the stable normal-C branch to the oscillatory stable branch. The amplitude and position of ϕ_m while on the oscillatory branch describe a limit cycle, as expected for a relaxation oscillation which this represents. Typical limit cycles are depicted in Fig. 3. As α is increased further, ϕ_m, the oscillation frequency, and virtual-cathode position within the diode asymptotically approach limiting values. If α is decreased, the oscillation amplitude $\Delta\phi_m$ decreases, and the position of ϕ_m moves toward the diode center. The electron flow reverts to the equilibrium steady state when the perturbation due to the rate of change of diode current below the space-charge limit is sufficiently large. This normally occurs before the bifurcation point is reached. The entire process forms a hysteresis loop, which is depicted in Fig. 2.

The virtual cathode originates at the bifurcation point. This is the intersection of the oscillatory state with the C-overlap and partially reflected solution branches. The bifurcation point cannot be reached
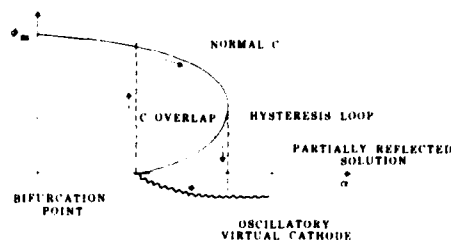
in the short-circuited diode. Of the three branches emanating from it, two (the steady ones) are physically unstable while the oscillatory branch is numerically unstable at this point. This results because the limit cycle at the bifurcation point is infinitesimally small, so that simulation codes lose resolution before it can be reached. Loss of resolution creates a small-amplitude high-frequency oscillation observed in this study and previously.[9] This result is numerical, not physical.

This problem can be overcome if we eliminate the hysteresis loop. Then the C-overlap branch disappears, and we can get to the bifurcation point along the stable normal-C branch. This can be accomplished in several ways. The most appropriate in this study is to have a retarding potential difference across the diode equal to the injected-electron kinetic energy. Then the C-overlap solution vanishes, and the bifurcation takes place at the space-charge limit α_{SCL}. The oscillation can be described as a small perturbation on the beam rather than the radical change that results in the short-circuited diode when α_{SCL} is exceeded. This analysis indicates that the onset of virtual-cathode formation occurs when the electron velocity in the steady state vanishes at some point inside the diode. For the short-circuited diode, this occurs at the diode center; for the biased diode, it occurs at $x \leq l$. Because the oscillation is a small perturbation on the steady-state fields in the biased diode, it is readily seen that the virtual-cathode oscillation period at onset is the electron transit time from the injection plane to the position where the velocity vanishes.

Finally, consider the particle dynamics during the oscillation period for counterclockwise limit cycles $(\alpha \leq \alpha_{SCL})$ as in Fig. 3(c). At the point where the virtual-cathode position is a minimum and the potential well is starting to move to the right, its amplitude is too small to stop the electrons. When its motion is to the left it opposes the electron beam
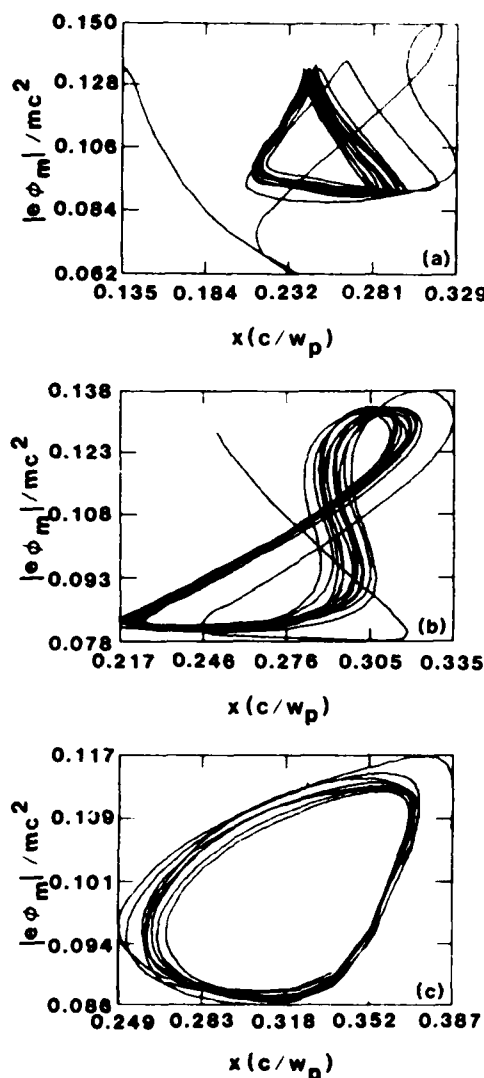
FIG. 3. Typical virtual-cathode limit cycles in the classical short-circuited one-dimensional diode with an injection energy of 51 keV. (a) $\alpha = 2.5$, (b) $\alpha = 2.0$, and (c) $\alpha = 1.4$. Motion in (a) is clockwise and in (c) is counterclockwise. $l = 1.0c/\omega_p$.

and causes particle bunching. Since the well is deeper, the stream velocity will vanish at some location and then become negative. Here, the second derivative of the velocity $(d^2 u/dx^2)$ is also negative. In this process the stream is continuously deformed to create a double-valued negative velocity protrusion. The entire system is three-valued (Fig. 4), as in a collisionless shock wave.[?] Here, the region of triple flow is not limited, as in usual collisionless shocks, by the presence of a transverse magnetic field,[?] but rather by the presence of the walls. Indeed, the reflected part detaches from the main beam and exits through the anode periodically, thus

being responsible for the onset of oscillatory behavior in beam characteristics. As the potential minimum reaches the end of its left motion the two "lips" of the back reflected stream close. At this point no more electrons are reflected, and the well moves to the right, repeating the cycle.

For larger values of α the limit cycle is distorted into a figure "8" with one lobe having a clockwise motion and the other a counterclockwise one [Fig. 3(b)]. This transition continues until the motion is completely clockwise [Fig. 3(a)]. It indicates a change in the particle bunching process and is related to the fraction of current which is reflected versus transmitted from the injected-electron beam. In Fig. 3(a) most of the beam is reflected, whereas in Fig. 3(c) most electrons are transmitted.

III. THEORY

The one-dimensional motion of electrons in the diode is given by the equations of continuity and momentum conservation for the electrons plus Poisson's equation. They are expressed here as

$$\rho_{\tilde{t}} + (\rho v)_{\tilde{x}} = 0 , \tag{1a}$$

$$v_{\tilde{t}} + vv_{\tilde{x}} = -(e/m)\xi , \tag{1b}$$

$$\epsilon_0 \xi_{\tilde{x}} = \rho + \rho_h , \tag{1c}$$

where $0 \le \tilde{x} \le l$. The subscripts denote differentiation with respect to that variable. Electron and heavy-ion charge densities, and electron velocity, electric field, time, and position, are indicated by ρ, ρ_h, v, ξ, $\tilde{t}$, and $\tilde{x}$, respectively. The appropriate boundary conditions are $v(0,\tilde{t})=v_0$, $\rho(0,\tilde{t})=\rho_0$, and $\int_0^l \xi \, d\tilde{x} = 0$. An ion component is placed in Poisson's equation in order to discuss two-species space-charge flow. Conservation equations of mass and momentum for the heavy ions are not included, because it is assumed that their velocity does not change appreciably during their passage through the diode.

In order to simplify the mathematics, we introduce dimensionless equations for our model. They are

$$n_t + (nu)_x = 0 , \tag{2a}$$

$$u_t + uu_x = -\alpha E , \tag{2b}$$

$$E_x = \alpha(n + l) , \tag{2c}$$

where $n = \rho/\rho_0$, $u = v/v_0$,

$$E = (e\epsilon_0/m \rho_0)^{1/2}\xi/v_0 ,$$

$$t = v_0\tilde{t}/l , \quad \tilde{x} = x/l ,$$

$$\alpha = (e \rho_0/\epsilon_0 m)^{1/2}l/v_0$$
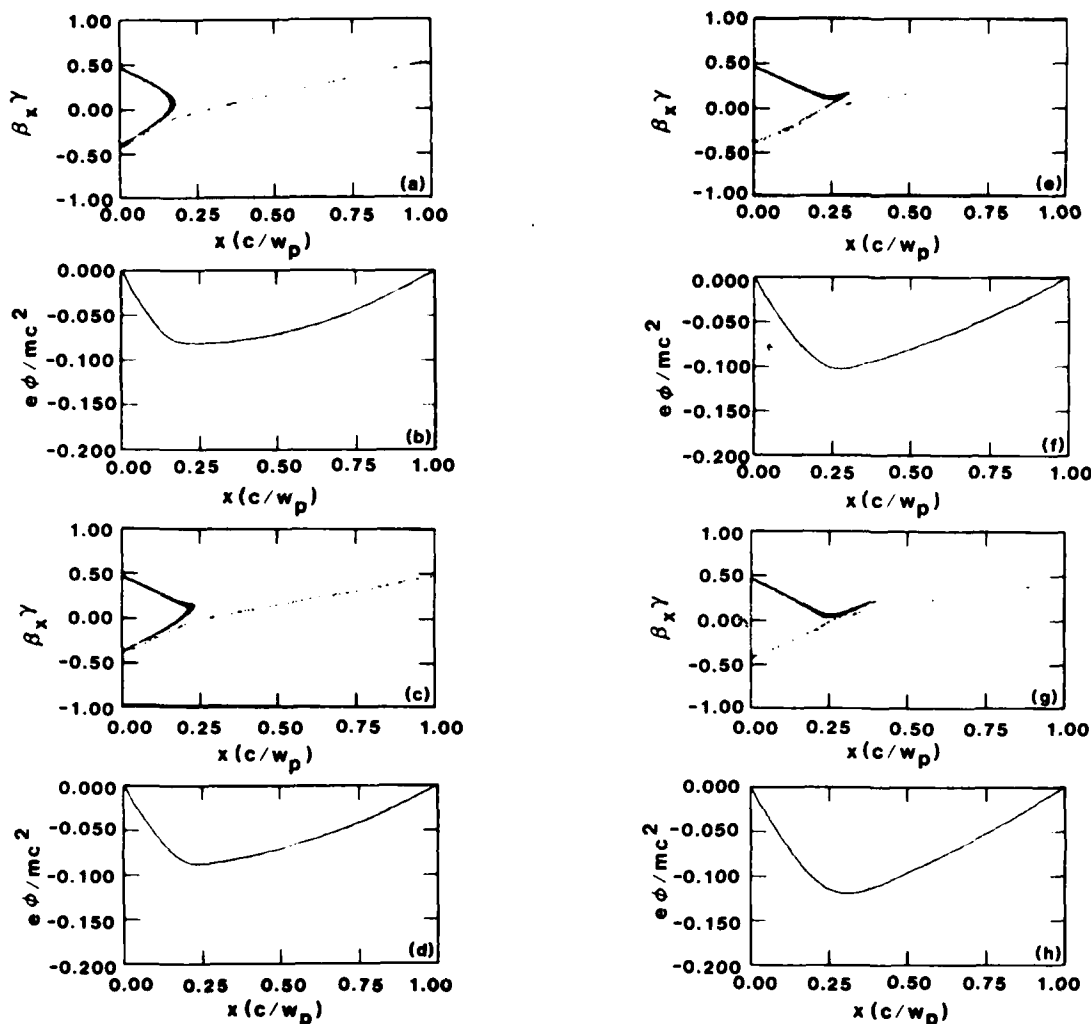
FIG. 4. Successive snapshots of electron-beam momentum space and corresponding potential shape in the diode for $\alpha = 2.0$, $I = 1.0c/\omega_p$. Time between frames is $0.5\omega_p^{-1}$. Initial beam kinetic energy is 51 kev.

(a dimensionless parameter related to current), and the ratio of heavy-ion to electron charge densities, $I = \rho_h / \rho_0$. Alternatively, α may be written as $I\omega_p / v_0$, where ω_p is the beam plasma frequency. The boundary conditions for electrons become $u(0,t) = 1$, $n(0,t) = -1$, and $\int_0^1 E\,dx = 0$. For an ion beam, $n(0,t) = 1$; otherwise, the following derivation is the same.

A. Unneutralized beams

For an unneutralized beam, setting $I = 0$ and solving by the method of characteristics[29,30] we find

$$n^{-1} = -\tfrac{1}{2}\alpha^2(t-s)^2 + \alpha E_0(s)(t-s) - 1 , \qquad (3)$$

where s is the entry time for the particle occupying

position x at time t, and $E_0(s)$ is the electric field at $x = 0$. The particle trajectories are found by utilizing Eq. (2a), from which it follows that

$$\left.\left(\frac{\partial x}{\partial s}\right)\right|_t = n^{-1} . \qquad (4)$$

This yields

$$x = \tfrac{1}{6}\alpha^2(t-s)^3 + \alpha \int_t^s E_0(s)(t-s)\,ds + (t-s) . \qquad (5)$$

Integration of the trajectory equation is hard for general time-dependent situations, because imposing the proper boundary conditions leads to a nonlinear integral equation for $E_0(t)$. However, several special cases can be solved exactly. The problem of injec-

tion into an empty diode can be integrated until the formation of a singularity in n, indicating the crossing of trajectories.[30] In this case, the stream velocity becomes three-valued and one must use a Vlasov-equation description,[31] rather than system (2) that is derived assuming a single stream of monoenergetic particles. As described in Sec. II, this multistreaming is characteristic of the oscillatory state created when α exceeds its SCL value.

Using these equations we can derive a similar representation for Fig. 2 in terms of E_0 and α. For steady states, $E_0(t) = E_0$, a constant, we find

$$u = -n^{-1} = \tfrac{1}{2}\alpha^2(t-s)^2 - \alpha E_0(t-s) + 1 , \quad (6a)$$

$$x = \tfrac{1}{6}\alpha^2(t-s)^3 - \tfrac{1}{2}\alpha E_0(t-s)^2 + (t-s) . \quad (6b)$$

Imposing the conditions $x = 1$, $u = 1$ at $t-s = t_0$, the particle transit time, we note that t_0 must satisfy

$$\tfrac{1}{12}\alpha^2 t_0^3 - t_0 + 1 = 0 . \quad (7)$$

This equation has two positive solutions for $0 \le \alpha \le \tfrac{4}{3}$, coalescing at $\alpha = \tfrac{4}{3}$. The largest one, for $0 \le \alpha < 2\sqrt{2/3}$ does not correspond to a real flow. In Fig. 5 we show E_0 ($= \alpha t_0/2$) vs α. This representation will be used in the discussion of nonlinear stability.

B. Neutralized beams

The Pierce instability occurs when electron and ion space-charge flow is considered in finite geometries where there is no potential difference across the boundaries.[32] The ions can be stationary or moving with respect to the electrons. Charge neutrality is maintained at the injection plane. This instability may have ramifications for charged-particle inertial confinement fusion because of its ef-

FIG. 5. Electric field at the injection plane vs current α for $I = 0$. Plot depicts the normal C-flow (stable) and C-overlap (unstable) solutions. Oscillating virtual-cathode (stable) solution is also shown. Regions I and II define the domains of attraction of the normal-C and virtual-cathode solutions near the SCL, α .

fect on neutralized-beam propagation in the reactor.[33] In this section, we show that the Pierce instability is a special case of electron and ion space-charge flow. In general, two-species flow has steady and oscillatory states analogous to one-species space-charge flow.

The steady-state behavior for the case of arbitrary I can be found in a manner similar to $I = 0$. Rewriting system (2) in characteristic coordinates, we arrive at

$$\frac{d^2}{dt^2}\left[1+\frac{I}{n}\right] + \alpha^2 I\left[1+\frac{I}{n}\right] = 0 . \quad (8)$$

For positive ions $(I > 0)$ the solution of (8) after satisfying the boundary conditions is

$$1 + I/n = (1+I)\cos[\alpha\sqrt{I}(t-s)]$$
$$\qquad + E_0\sqrt{I}\,\sin[\alpha\sqrt{I}(t-s)] . \quad (9)$$

Imposing conditions $x = 1$, $u = 1$ at $t-s = t_0$, we find the system

$$1 = \frac{1}{I}t_0 - \left[\frac{1-I}{\alpha I^{3/2}}\right]\sin(\alpha\sqrt{I}t_0)$$
$$\qquad + \frac{E_0}{\alpha I}[\cos(\alpha\sqrt{I}t_0)-1] , \quad (10a)$$

$$1 = \frac{1}{I} - \left[\frac{1-I}{I}\right]\cos(\alpha\sqrt{I}t_0)$$
$$\qquad - \frac{E_0}{I}\sin(\alpha\sqrt{I}t_0) . \quad (10b)$$

For $I = 1$, which implies charge neutralization, these equations reduce to the relations given in Ref. 34 for the Pierce instability. However, by varying I the curves shown in Fig. 6 are obtained. These are cuts at constant I through a three-dimensional contiguous surface. The space is defined by the axes $\bar{E} = E_0 I^{1/2}$, $A = \alpha I^{3/2}$, and I. The surface is 2π periodic in A with the vertical plane at $A = 2\pi$ being common for all values of I. For given A, a linearized analysis establishes that the equilibria denoted by the curves are stable (unstable) for the lowest (highest) value of $\bar{E}$. At $I = 1$, exchange of stability takes place at odd multiples of π. For $I < 1$, exchange of stability occurs at the points where $dE_0/d\alpha \to \infty$.

It is evident from Fig. 6 that, for $I < 1$, there are no stable equilibrium solutions in the neighborhood of $A = \pi$. Therefore one expects a virtual cathode to form when $I < 1$ and A adiabatically increases to π. We have found, by using numerical simulation, that in this case the beam settles to an oscillatory state, similar to the virtual cathode for unneutralized
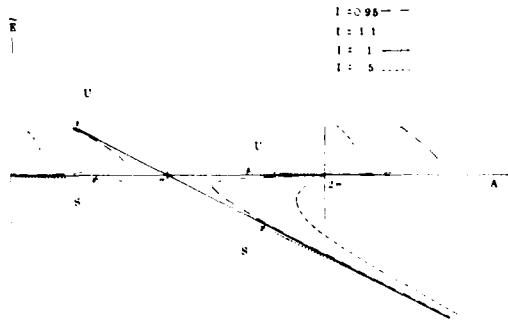
FIG. 6. Curves of scaled electric field at the injection plane $\tilde{E}$ vs scaled current A for various values of charge neutralization I. Curves represent slices through a three-dimensional surface. S and U indicate stable and unstable branches, respectively, for the $I = 1$ slice.

beams.[31] By slowly increasing I past the neutral-beam value of 1 in our simulation, we have established that this oscillation persists. Indeed, finding this oscillatory state for $I > 1$ by other means would have been difficult, because the simulation would tend to follow the stable steady-state branch that is present for all values of current.

C. Nonlinear stability analysis

For $I < 1$, it is of interest to establish the properties of the beam instability at the SCL—generalized for $I \neq 0$ to mean the point where $d\alpha/dE_0 = 0$. We shall carry out the analysis for $I = 0$, but our method can be applied to any similar jump phenomenon.

A linear stability analysis[6] about the steady state described by (7) results in the dispersion relation

$$(2+\beta)e^{-\beta} = 2 - \beta + \beta^3/(\alpha^2 t_0^3) , \tag{11}$$

where $\beta = i\omega t_0$. We have written the expression derived in Ref. 6 in terms of our dimensionless variables. For α near the SCL value we let

$$\alpha = \tfrac{4}{3} - \epsilon^2 , \quad \epsilon \ll 1 \tag{12}$$

and find from (7) that near this value, t_0 is approximately

$$t_0 \sim \frac{3}{2} + \epsilon \frac{3}{2\sqrt{2}} + O(\epsilon^2) , \tag{13}$$

where the $-$ ($+$) sign corresponds to the lower (upper) branch in Fig. 5.

By substituting in (11), and assuming β small, we find that

$$i\omega = \beta \sim \mp 2\sqrt{2}\epsilon + O(\epsilon^2) . \tag{14}$$

Since the linearized analysis led to time factors of the form $e^{i\omega t}$ in the perturbations, it follows that the lower branch in Fig. 5 is stable and the upper un-

stable, while at the SCL ($\epsilon = 0$) we have neutral stability.

Above the value $\alpha = \tfrac{4}{3}$, linearized theory is not applicable. Utilizing multiple-scaling perturbation theory,[35] we can carry out a nonlinear stability analysis near $\alpha = \tfrac{4}{3}$. In system (2) we set $\alpha = \tfrac{4}{3} + \epsilon^2$. In this neighborhood, perturbations evolve on a "slow" time scale, depicted by $\tau = \epsilon t$.

Eliminating the electric field by combining (2b) and (2c) and utilizing τ, system (2) becomes

$$\epsilon n_\tau + (nu)_x = 0 , \tag{15a}$$

$$(\epsilon u_\tau + uu_x)_x = -(\tfrac{4}{3} \pm \epsilon^2)^2 n \tag{15b}$$

with conditions $u(0,\tau) = 1$, $n(0,\tau) = -1$, and $\int_0^1 E\,dx = 0$ rewritten as

$$\epsilon \int_0^1 u_\tau dx + \tfrac{1}{2}[u^2(1,\tau) - u^2(0,\tau)] = 0 . \tag{16}$$

Substituting the asymptotic expansions

$$u \sim \sum_{i=0}^{j} \epsilon^i u_i(x,\tau) + O(\epsilon^{j+1}) ,$$

$$n \sim \sum_{i=0}^{j} \epsilon^i n_i(x,\tau) + O(\epsilon^{j+1}) , \tag{17}$$

for u and n into (15) and equating coefficients of various powers of ϵ, there results a hierachy of equations for the u_i and n_i.

Solving the $O(1)$ system gives

$$(u_0 - \tfrac{1}{2})(u_0 + 1)^2 = 2(2x - 1)^2 , \tag{18a}$$

$$n_0 = -1/u_0 . \tag{18b}$$

To solve the $O(\epsilon)$ system we introduce a new variable q by

$$x = \frac{16}{9}\left[\frac{q^3}{6} - \frac{3}{8}q^2\right] + q , \tag{19}$$

so that

$$u_0 = \frac{16}{9}\left[\frac{q^2}{2} - \frac{3}{4}q\right] + 1 . \tag{20}$$

We then find

$$n_1 = \frac{1}{u_0^2} u_1 , \tag{21a}$$

$$u_1 = C\frac{q(q - \tfrac{3}{2})}{u_0} \tag{21b}$$

with C a constant of integration which is, in general, a function of the slow time τ. To find $C = C(\tau)$ which determines the slow evolution of the perturbation $u_1(x,\tau)$ we need to go to the next order, $O(\epsilon^2)$. By substituting in the expressions for u_0, u_1, n_0, n_1 and eliminating n_2, we find that $u_2(x,\tau)$ satisfies

$$(u_0 u_2)_{xx} + \frac{16}{9}\frac{1}{u_0^2} u_2 = \frac{16}{9}\frac{C_\tau}{u_0} \int_0^q \frac{q(q-\frac{1}{2})}{u_0^2} dq + C^2 \frac{q^2(q-\frac{1}{2})^2}{u_0^3} - C_\tau \left| \frac{q(q-\frac{1}{2})}{u_0} \right|_x + \frac{8}{3}\frac{1}{u_0} ,$$ (22a)

$$u_2(0,\tau)=0 , \quad u_2(1,\tau)= +\frac{9}{16}C_\tau .$$ (22b)

The solution to this inhomogeneous two-point boundary-value problem exists provided a certain orthogonality condition between the right-hand side and the solution of the adjoint problem that takes account of the boundary conditions is satisfied (Fredholm alternative theorem).[36] This leads to the desired equation determining $C(\tau)$,

$$aC_\tau + bC^2 \cdot c = 0 ,$$ (23)

where a, b, and c are found to be

$$a = - \int_0^{3/2} \frac{q(q-\frac{1}{2})}{u_0^2} [\frac{16}{9}q^2(q-\frac{9}{4}) + \frac{1}{2}]dq = 1.6850 ,$$ (24a)

$$b = \frac{1}{3} \int_0^{3/2} \frac{q^3(q-\frac{1}{2})^3}{u_0^4} dq = -3.7968 ,$$ (24b)

$$c = \frac{1}{3} \int_0^{3/2} q(q-\frac{1}{2})dq = -1.5 .$$ (24c)

In (23) the $(+)$ or $(-)$ signs indicate that we are above or below the SCL, respectively.

Above the SCL, we find

$$C(\tau) = -\frac{c}{b}\tan\left| \sqrt{\bar{cb}} \left| \frac{\tau + \tau_0}{a} \right| \right| ;$$ (25)

and below the SCL,

$$C(\tau) = \begin{cases} \left| \frac{c}{b}\tanh \left| \sqrt{\bar{cb}} \left| \frac{\tau + \tau_0}{a} \right| \right| \right| , & C(0) < (c/b)^{1/2} \\[2mm] \left| \frac{c}{b}\coth \left| \sqrt{\bar{cb}} \left| \frac{\tau + \tau_0}{a} \right| \right| \right| , & C(0) > (c/b)^{1/2} \end{cases}$$ (26)(27)

where τ_0 is a constant of integration. In general, small initial perturbations will lead to the solution

$$u(x,t) \sim u_0 + \epsilon \sum_{i=1} C_i(\tau)e^{\omega_i t}u_i(x)+O(\epsilon^2) ,$$ (28)

where ω_i are the various distinct solutions of the dispersion relation (11) at $\alpha = \frac{4}{3}$.[15,17] It is straightforward to show that all modes are such that $\mathrm{Re}\,\omega_i < 0$ except one for which $\omega = 0$. Thus all other modes will decay in the fast time scale and only the neutral mode $(\omega = 0)$ will persist. Our solution after a short time will look like

$$u \sim u_0 + \epsilon C(\tau)\frac{q(q-\frac{1}{2})}{u_0} +O(\epsilon^2) .$$ (29)

From the given initial conditions it is easy to determine the initial condition for the neutral mode. Below the SCL, if the initial conditions are such that $C(0) > -(c/b)^{1/2}$, the solution will evolve to the stable lower branch in Fig. 5 (region I), while if $C(0) < -(c/b)^{1/2}$, $C \rightarrow \infty$ in finite time (Fig. 5, region II). Blowup in finite time also occurs above the SCL for any $C(0)$. This does not mean that the actual solution blows up, just that it evolves to a final state far away from the two steady-state branches shown in Fig. 5 and thus is not accessible by perturbation theory.

As can be seen in (25), the blowup above the SCL is described by a tangent function, therefore the growth rate we find for this case must be appropriately interpreted. Note that the linearized dispersion relation seems to suggest an imaginary exponential growth rate above the space-charge limit.[3,6] In view of our results, we see that this is actually misleading. Moreover, we find that even below the SCL the stable steady-state branch can be destabilized by sufficiently large perturbations.

Our results agree with the linear theory, provided we consider the limit where the latter becomes ap-

plicable. Thus we must compare the linear theory with (26) as $\tau \to +\infty$ (near the stable branch) and (27) as $\tau \to -\infty$ (near the unstable branch). To demonstrate this we set $\tau = \epsilon t$ in (26) and consider the limit $\tau \to +\infty$. Then

$$C(t) = \frac{c}{b} \tanh \left[\frac{\sqrt{cb}}{a}(\epsilon t + \tau_0) \right]$$

$$= \frac{c}{b} \frac{1 - \exp\left[-\frac{2\sqrt{cb}}{a}(\epsilon t + \tau_0) \right]}{1 + \exp\left[-\frac{2\sqrt{cb}}{a}(\epsilon t + \tau_0) \right]}$$

$$\simeq \frac{c}{b} \left[1 - 2\exp\left[-\frac{2\sqrt{cb}}{a}(\epsilon t + \tau_0) \right] \right.$$

$$\left. + \cdots \right] . \tag{30}$$

We see that the decay rate of the perturbations as $t \to +\infty$ is equal to

$$\frac{2\sqrt{cb}}{a}\epsilon \approx 2.83\epsilon , \tag{31}$$

which is the same as that found by the linearized analysis.[6] This quantity is important as it also

determines an initial "growth rate" for the jump instability above the SCL described by (25). If we substitute the original dimensional time variable into our expressions and write the deviation of α from its value at the SCL as

$$\epsilon = (\alpha - \alpha_{\text{SCL}})^{1/2} = (\alpha - \tfrac{4}{3})^{1/2} , \tag{32}$$

we find that the "growth rate" is given by

$$D = (\alpha - \tfrac{4}{3})^{1/2} \frac{\sqrt{cb}}{a} \frac{v_0}{l} \tag{33}$$

or

$$D = \left[\frac{l\omega_p}{v_0} - \frac{4}{3} \right]^{1/2} \sqrt{2} \frac{v_0}{l} . \tag{34}$$

Of course, for the expansions in (28) to be valid, we must have $C(\tau) \ll 1/\epsilon$. However, while C is not too large, (25) gives a reliable estimate for the growth rate of the instability.

ACKNOWLEDGMENTS

*Permanent address: Mission Research Corporation, 1720 Randolph Rd. S.E., Albuquerque, NM 87106.

[1]G. D. Child, Phys. Rev. (Ser. I) 32, 492 (1911).

[2]I. Langmuir, Phys. Rev. 21, 419 (1923).

[3]C. K. Birdsall and W. B. Bridges, Electron Dynamics of Diode Regions (Academic, New York, 1966), Chap. 3.

[4]H. R. Jory and A. W. Trivelpiece, J. Appl. Phys. 40, 3924 (1969).

[5]V. S. Voronin, Yu. T. Zozulya, and A. N. Lebedev, Zh. Tekh. Fiz. 42, 546 (1972) [Sov. Phys.—Tech. Phys. 17, 432 (1972)].

[6]R. J. Lomax, Proc. IEEE 108, 119 (1961).

[7]C. E. Fay, A. L. Samuel, and W. Shockley, Bell Syst. Tech. J. 17, 49 (1938).

[8]C. K. Birdsall and W. B. Bridges, J. Appl. Phys. 32, 2611 (1961).

[9]W. B. Bridges and C. K. Birdsall, J. Appl. Phys. 34, 2946 (1963).

[10]D. A. Dunn and I. T. Ho, AIAA J. 1, 2770 (1963).

[11]S. A. Goldstein and R. Lee, Bull. Am. Phys. Soc. 23, 763 (1978).

[12]R. A. Meyer, S. A. Goldstein, D. D. Hinshelwood, and G. Cooperstein, Bull. Am Phys. Soc. 24, 977 (1979).

[13]D. S. Prono, J. M. Creedon, I. Smith, and N.

Bergstrom, J. Appl. Phys. 46, 3310 (1975).

[14]D. S. Prono, J. W. Shearer, and R. J. Briggs, Phys. Rev. Lett. 37, 2 (1976).

[15]P. A. Miller, J. A. Halbleib, J. W. Poukey, and J. T. Verdeyen, J. Appl. Phys. 52, 593 (1981).

[16]J. W. Poukey and N. Rostoker, Plasma Phys. 13, 897 (1971).

[17]C. L. Olson, in Collective Ion Acceleration-Springer Tracts in Modern Physics (Springer, Berlin, 1979), Vol. 84.

[18]C. L. Olson, IEEE Trans. Nucl. Sci. NS-26, 4231 (1979).

[19]C. L. Olson, J. R. Woodworth, C. A. Frost, and R. A. Gerber, IEEE Trans. Nucl. Sci. NS-28, 3349 (1981).

[20]R. B. Miller, in Proceedings of the Second International Topical Conference on High-Power Electron and Ion Beam Research and Technology (Cornell University Press, Ithaca, N.Y., 1977), p. 613.

[21]R. B. Miller, in Collective Methods of Acceleration, edited by N. Rostoker and M. Reiser (Harwood, New York, 1979), p. 675.

[22]R. A. Mahaffey, P. Sprangle, J. Golden, and C. A. Kapetanakos, Phys. Rev. Lett. 39, 843 (1977).

[23]H. E. Brandt, A. Bromborsky, H. B. Bruns, and R. A.

Kehs, in Ref. 20, p. 649.

[24]J. M. Buzzi, H. J. Doucet, B. Etlicher, P. Haldenwang, A. Huetz, H. Lamain, C. Rouille, J. Cable, J. Delvaux, J. C. Jouys, and C. Peugnet, in Ref. 20, p. 663.

[25]D. J. Sullivan, in *Proceedings of the Third International Topical Conference on High-Power Electron and Ion Beam Research and Technology* (Institute of Nuclear Physics, Novosibirsk, USSR, 1979), p. 769.

[26]A. N. Didenko, G. P. Fomenko, I. Z. Gleizer, Ya. E. Krasik, G. V. Melnikov, S. F. Perelygin, Yu. G. Shtein, A. S. Sulakshin, V. I. Tsvetkov, and A. G. Zerlitsin, in Ref. 25, p. 683 (1979).

[27]R. Z. Sagdeev, *Reviews of Plasma Physics*, edited by M. A. Leontovich (Consultants Bureau, New York, 1966), Vol. 4, p. 23.

[28]S. S. Moiseev and R. Z. Sagdeev, Plasma Phys. **5**, 43 (1963).

[29]G. B. Whitham, *Linear and Nonlinear Waves* (Wiley, New York, 1974).

[30]E. A. Coutsias and D. J. Sullivan (unpublished).

[31]D. J. Sullivan and E. A. Coutsias, in *High-Power Beams '81*, edited by H. J. Doucet and J. M. Buzzi (Ecole Polytechnique, Palaiseau, France, 1981), p. 371.

[32]J. R. Pierce, J. Appl. Phys. **15**, 721 (1944).

[33]J. W. Poukey, J. P. Quintenz, and C. L. Olson, Appl. Phys. Lett. **38**, 20 (1981).

[34]B. B. Godfrey, Mission Research Corporation Report No. AMRC-R-282, 1981 (unpublished).

[35]J. Kevorkian and J. D. Cole, *Perturbation Methods in Applied Mathematics* (Springer, Berlin, 1981).

[36]G. Birkhoff and G. Rota, *Ordinary Differential Equations* (Ginn, Boston, 1962).

[37]A. V. Paschenko and B. N. Rutkevich, Fiz. Plazmy **3**, 774 (1977) [Sov. J. Plasma Phys. **3**, 437 (1977)].

HIGH POWER MICROWAVE GENERATION FROM A
VIRTUAL CATHODE OSCILLATOR (VIRCATOR)

HIGH POWER MICROWAVE GENERATION FROM A VIRTUAL CATHODE OSCILLATOR (VIRCATOR)

Donald J. Sullivan
Mission Research Corporation
Albuquerque, New Mexico 87106

Abstract

High power microwaves, up to Gigawatt levels in the centimeter regime, have been observed in reflex triode, foil and foilless diode systems. Generation efficiencies range from 1% to 12%. The source of the microwaves is an oscillating virtual cathode - the nonlinear state which develops when the electron beam injection current exceeds the space-charge limiting current defined by the beam energy and wave guide geometry. This stable oscillation results in severe longitudinal charge bunching giving rise to large time dependent current variations. The experimental frequency dependence and broadband characteristics are explained by the scaling of the oscillator frequency with $\sqrt{n_b/\gamma}$, where n_b is the beam density and γ its relativistic factor, in conjunction with the Child-Langmuir relation. The optimal design for a narrow-band millimeter wave vircator is based on a foilless diode with a strong axial magnetic field. It will be tunable over an order of magnitude in frequency by varying the magnetic field strength.

Introduction

Of the several millimeter sources that are in various stages of development, the virtual cathode oscillator (Vircator) has a combination of characteristics which recommend it for high frequency use. First, the frequency of the vircator is tunable by changing the magnitude of an imposed axial magnetic field, eliminating any requirement to change the physical structure of the device. A single vircator will be tunable over an order of magnitude in frequency (e.g., 10 GHz - 100 GHz). Second, the bandwidth of the generator can be narrow or broad based on magnetic field shaping and the use of beam limiters described below. Third, because the vircator functions above the space-charge limiting current for the electron beam, given efficient operation, it should be capable of much higher power than other microwave sources. Finally, the lack of passive resonating structures to produce the transmitted wave reduces the problem of field emission. This also increases the maximum possible generator power.

Experimentally, the virtual cathode has already proven itself to be a copious microwave source.[1-7] Table 1 lists experiments which have been carried out to date. With the exception of the Didenko experiment at Tomsk,[4] the frequency spectra have all had a broad bandwidth and relatively low efficiency. Nevertheless, even at low efficiency the experiment at Harry Diamond Laboratories[5] using a foilless diode (1 MV, 30 kA) produced Gigawatts of power in the Ku band. It is one of the most powerful centimeter wavelength microwave sources available. It will be shown later that the foilless diode in a shaped axial magnetic field represents the best configuration for a high frequency device.

Microwave Generation

Although only scaling relations are presently available, qualitative dependencies of virtual cathode parameters on beam kinetic energy and injected current are known.[8,9] First, potential amplitude, position, and oscillation frequency all have the same functional dependence on injected beam current. These parameters

TABLE 1

REFERENCE	SYSTEM	PEAK POWER	FREQUENCY	EFFICIENCY
1. MAHAFFEY, et al.	REFLEX TRIODE	100 MW	11 GHz (10.6 - 13.4 GHz)*	1.5%
2. BRANDT, et al.	REFLEX TRIODE	---	9.5 GHz (7.0 - 13.0 GHz)*	---
3. BUZZI, et al.	FOIL DIODE	1 GW	10 GHz (9.0 - 14.0 GHz)*	1.25%
4. DIDENKO, et al.	REFLEX TRIODE	1.4 GW	3.3 GHz (3.1 - 5.0 GHz)*	17%
5. BROMBORSKY, et al.	FOILLESS DIODE	3 GW	16 GHz (5.2 - 18.0 GHz)*	4%
6. CLARK, et al.	FOILLESS DIODE	---	WIDEBAND (1.7 - 40.0 GHz)*	---
7. EKDAHL, et al.	FOILLESS DIODE	> 100 MW	> 70 GHz	---

* DETECTOR BANDWIDTH IN PARANTHESES

asymptotically approach a limiting value for current above the space-charge limit. Second, the fundamental oscillation frequency is approximately the relativistic beam plasma frequency given by

$$\omega_p^r = \left(\frac{4\pi n_b^0 e^2}{\gamma_0 m} \right)^{1/2} \qquad (1)$$

where n_b^0 is the electron beam number density at injection γ_0 is the beam relativistic factor, e is the electron charge and m is its mass. In particular, the oscillation frequency from one-dimensional electrostatic and two-dimensional electromagnetic numerical simulations varies such that

$$\omega_p^{rel} \le \omega_{osc} \le \sqrt{2\pi}\, \omega_p^{rel} \qquad (2)$$

The value of $\sqrt{2\pi}$ is an empirical result which has not yet been derived theoretically. The value of ω_{osc} increases with current monotonically. If the injection current exceeds the space-charge limiting current by a factor of three or greater, ω_{osc} is close to the maximum value. Equation 11 in conjunction with the Child-Langmuir law describing space-charge limited diode emission explains the experimental linear dependence of frequency on the square root of diode voltage in foil diodes and reflex triodes.

The virtual cathode oscillates stably at a set frequency in both time and space. This fluctuating potential barrier acts as a gate to reflect some electrons and transmit others. The motion of the gate bunches charge. In two dimensions the charge bunch and virtual cathode are separated spatially.

By analogy this configuration represents an LC oscillator. The virtual cathode acts as a capacitor to store the beam kinetic energy. During that portion of the limit cycle in which the potential is greater than the injected beam energy, charge is constrained to remain near the anode. This starves the virtual cathode so that its amplitude decreases below $(\gamma_0-1)\, mc^2/e$. Once this occurs the charge bunch is transmitted. The electron motion represents a large time varying current through an inductor. The presence of charge away from the anode reestablishes the virtual cathode, and the cycle repeats. The effect on

beam current can be examined using simulations. A net current diagnostic is given in Fig. 1 where the probe is positioned between the anode and virtual cathode. The injected current in units of mc^3/e, v_0, is 3.4 times the limiting current, v_ℓ, and γ_0 is 3.5. Note that the virtual cathode can actually reverse the direction of current. The average current value is v_ℓ.

The oscillating current generates microwaves.[10,11] The wave frequency is the oscillation frequency of the virtual cathode. The wave propagates down the drift tube in a TM waveguide mode, which determines the wavelength and phase velocity of the wave in the guide. The field configuration is evident in simulations where there is no axial magnetic field. If a cold beam is injected and azimuthal symmetry is assumed by the code, the only nonzero fields are E_z, E_r, and B_θ in cylindrical geometry. These three fields define a TM wave traveling in the z direction.

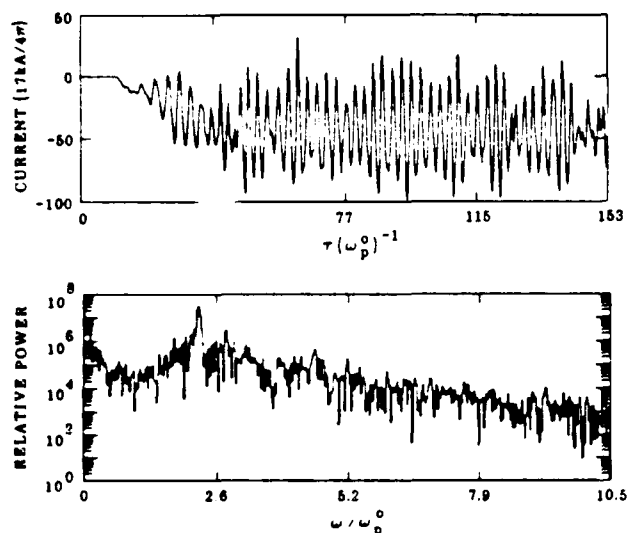Figure 1. Net current amplitude and spectrum for a probe placed between the anode and virtual cathode. $\nu_0=3.5$, $\nu_c=3.4$.

The largest impediment to constructing an efficient vircator is the effect which heating has on the microwave generation efficiency. As noted earlier[12], beam temperature significantly damps out the amplitude of the potential oscillation. This can be understood in the following way. For a monoenergetic beam all of the charged particles bunch at the same location. Mathematically this represents a singularity where the charge density goes to infinity. In reality the charge bunch is not infinitely dense, but it does become several times greater than the initial beam injection density. The severity of the charge bunching leads to efficient microwave generation. If, on the other hand, the beam has a spread in axial momentum, the electrons will stop at different locations in the potential well. This tends to limit the charge bunching and the amplitude of the oscillating electric and magnetic fields. The effect of beam temperature in reducing the RF efficiency of the vircator has been witnessed in one-dimensional electromagnetic simulations.[13] A beam spread of less than 3% in energy reduces the microwave generation efficiency from 20% to approximately 2%. Under these conditions the vircator is nothing more than a Barkhausen oscillator.[14] Indeed, the low efficiency and broad bandwidth observed in most of the experiments to date can probably be attributed to the effects of electron reflexing in the diode region resulting in beam heating.

Vircator Design

Based on our current theoretical knowledge of the virtual cathode, numerical simulations, and experimental results, the following points must be considered in the design of a coherent, high frequency vircator. First, generation of high microwave frequencies requires large beam densities. Extremely high beam densities ($n_0 > 10^{14}$ cm^{-3}) have been obtained from a foilless diode. The beam plasma frequency scales linearly with the electron cyclotron frequency due to the magnetic field.[15] This is of significance, because it implies that a single vircator can be tuned over an order of magnitude in frequency (eg. 10-100 GHz) simply by changing the axial magnetic field strength without changing the physical structure of the device.

Second, both the oscillation frequency and net current asymptotically approach a value as injected current is increased above the space-charge limit. Thus, using a very large value of v_0/v_ℓ does not substantially increase frequency or RF efficiency where efficiency is given by

$$n \leq \frac{e\Delta\phi}{(\gamma_0-1)\,mc^2} \qquad (3)$$

A foilless diode in a strong axial magnetic field produces a very thin annular beam. Since v_ℓ for an annular beam is larger than for a solid beam of the same area, the value of v_0/v_ℓ will be smaller for the same beam current.

In order to assure narrow bandwidth, high efficiency microwave generation at high or low frequency from the vircator, the following characteristics must be met. First, no reflexing of electrons in the region between the real and virtual cathodes must occur. Any axial magnetic field must be shaped to divert the electrons, or flux excluders must be employed to confine the magnetic field to the diode region. The latter arrangement will allow the radial space-charge electric field to perform the role of expelling electrons to the waveguide wall. In addition, if the beam is annular, a collimator may be used to help prevent reflexing of electrons back to the cathode. Second, the electron beam must be cold. Experimental[16] and theoretical[15] results indicate that foilless diodes create low emittance beams. Laminar flow, where the electron Larmor orbit is smaller than the beam thickness, is obtained when[16]

$$\omega_c > (\gamma_0 - 1)^{1/2}\,\frac{c}{\sqrt{a\delta/2}} \qquad (4)$$

where a is the orbit radius, δ is the radial spacing between the cathode and drift tube wall (which acts as the anode) and ω_c is the electron cyclotron frequency given by eB_z/mc. Low beam scatter is also assured, because of the lack of a foil. Finally, the diode voltage and injected current must be constant. More appropriately stated, the impedance must be constant. Flat-top voltage pulses can be attained in a variety of ways in several diode configurations. However, at high voltages the foilless diode operates as a purely resistive load, therefore $\omega_{osc} \propto \sqrt{I/V} = I^{1/2}$ is constant. Also, absence of diode closure in some foilless diode experiments makes a long pulse device possible.

It is evident from this discussion that the foilless diode in a strong axial magnetic field represents the optimal configuration for a high frequency vircator. It optimizes microwave power and efficiency while generating high frequency, coherent

radiation. For low frequency operation a foil diode or reflex triode utilizing a high transparency mesh for the anode can be used. No axial magnetic field should be employed in order to minimize electron reflexing.

A schematic of the configuration being used in the vircator experiment[17] at Mission Research Corporation is presented in Fig. 2. The pulse power parameters are 50 kV, 66 Ω matched impedance and a pulse length of 1 μsec. The magnetic field coil is capable of attaining 60 kG. We anticipate operating at frequencies as high as 100 GHz. Even with a low efficiency of 2.5% we will produce 1 MW of RF power. A multi-channel microwave grating spectrometer in the 30-110 GHz region developed by MRC will be the chief diagnostic on this experiment.[17]

In summary, the vircator has the potential for producing very high power microwave pulses in the centimeter and millimeter wavelength regimes. In a foilless diode configuration it is tunable by adjusting the imposed axial magnetic field. In a foil diode or reflex triode tuning is accomplished by changing the A-K gap spacing. The microwave generation will be coherent and efficient, if electron reflexing into the diode region is prevented.

For an injected current $v_o > 3 v_s$, $f_{osc} \sim \omega_p^{rel}/\sqrt{2\pi}$. Because the oscillating beam is equivalent to a deformable dipole, the preferred waveguide mode for an axisymmetric beam in a straight-walled cylindrical guide is TM_{0n} where $n = D/\lambda_0$, D is the waveguide diameter and λ_0 is the free space wavelength. Thus, D/λ_0 should be chosen to be close to an integer value. Once n is known, the phase velocity, group velocity, wavelength and impedance of the wave in the guide are determined. Similar considerations hold for a rectangular waveguide. Note that both v_ℓ and the cutoff wavelength, λ_c, depend on the guide dimensions and geometry. Both must be considered in choosing an experimental configuration.

BEAM TARGET ASSEMBLY
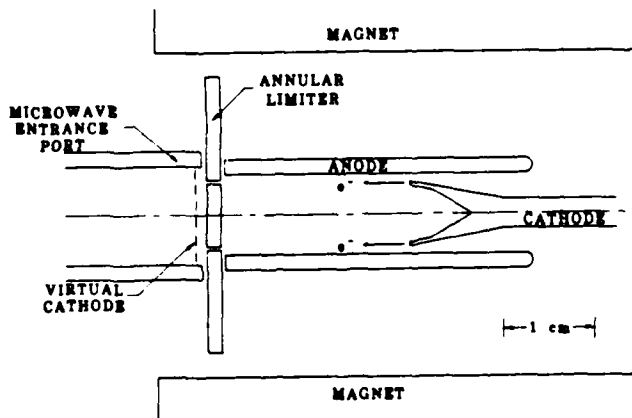
Figure 2. Schematic of the AFOSR/MRC Vircator

References

1. R. A. Mahaffey, P. Sprangle, J. Golden and C. A. Kapetanakos, Phys. Rev. Lett. 39, 843 (1977).

2. H. E. Brandt, A. Bromborsky, H. B. Bruns, and R. A. Kehs, in Proc. of the 2nd Intl. Top. Conf. on High Power Electron and Ion Beam Research and Technology, (Cornell University, Ithaca, New York, 1977), p. 649.

3. J. M. Buzzi, H. J. Doucet, B. Etlicher, P. Haldenwang, A. Huetz, H. Lamain, C. Rouille, J. Cable, J. Delvaux, J. C. Jouys and C. Peugnet, idem, p. 663.

4. A. N. Didenko, G. P. Fomenko, I. Z. Gleizer, Ya. E. Krasik, G. V. Melnikov, S. F. Perelygin, Yu. G. Shtein, A. S. Sulakshin, V. I. Tsvetkov, and A. G. Zerlitsin, in Proc. of the 3rd Intl. Top. Conf. on High Power Electron and Ion Beam Research and Technology, (Institute of Nuclear Physics, Novosibirsk, USSR, 1979), p. 683.

5. A. Bromborsky, H. Brandt, and R. A. Kehs, Bull. Am. Phys. Soc. 26, 165 (1981); and private communication.

6. M. C. Clark, private communication.

7. C. A. Ekdahl, private communication.

8. D. J. Sullivan and E. A. Coutsias in High Power Beams '81, Proceedings of the 4th Intl. Top. Conf. on High Power Electron and Ion Beam Research and Technology, edited by H. J. Doucet and J. M. Buzzi (Ecole Polytechnique, Palaiseau, France, 1981), p. 371.

9. E. A. Coutsias and D. J. Sullivan, to be published in Phys. Rev. A., March, 1983.

10. D. J. Sullivan, Bull. Am. Phys. Soc. 25, 948 (1980).

11. D. J. Sullivan, in Proc. of the 3rd Intl. Top. Conf. on High Power Electron and Ion Beam Research and Technology, (Institute of Nuclear Physics, Novosibirsk, USSR, 1979), p. 769.

12. W. B. Bridges and C. K. Birdsall, J. Appl. Phys. 34, 2946 (1963).

13. M. A. Mostrom, T. J. T. Kwan and C. M. Snell, Bull. Am. Phys. Soc. 27, 1075 (1982).

14. H. Barkhausen and K. Kurz, Phys. Zeit. 21, 1 (1920).

15. M. E. Jones and L. E. Thode, J. Appl. Phys., 51, 5212 (1980).

16. R. B. Miller, K. R. Prestwich, J. W. Poukey, and S. L. Shope, J. Appl. Phys. 51, 3506 (1980).

17. D. J. Sullivan, D. E. Voss, W. M. Bollen, R. H. Jackson and E. A Coutsias, AMRC-R-451 (1983), unpublished.

A HIGH FREQUENCY VIRCATOR MICROWAVE GENERATOR

(Beams '83 - Fifth International Conference on
High Power Particle Beams)

A HIGH FREQUENCY VIRCATOR MICROWAVE GENERATOR

Donald J. Sullivan
Mission Research Corporation
1720 Randolph Road, S. E.
Albuquerque, New Mexico 87106

Abstract

The virtual cathode oscillator (Vircator) has the potential for producing very high power microwave pulses in the centimeter and millimeter wavelength regimes. In a foilless diode configuration it is tunable by adjusting the imposed axial magnetic field. This permits high frequency operation. In a foil diode or reflex triode tuning is accomplished by changing the A-K gap spacing. The microwave generation will be coherent and efficient, if electron reflexing into the diode region is prevented. Gigawatt power levels have already been produced in the centimeter regime.

For an injected current a factor of three greater than the limiting current, $f_{osc} \sim \omega_p^{rel}/\sqrt{2\pi}$. Because the oscillating beam is equivalent to a deformable dipole, the preferred waveguide mode for an axisymmetric beam in a straight-walled cylindrical guide is TM_{0n} where $n = D/\lambda_0$, D is the waveguide diameter and λ_0 is the free space wavelength. Thus, D/λ_0 should be chosen to be close to an integer value. Note that both the limiting current and the cutoff wavelength depend on the guide dimensions and geometry. Both must be considered in choosing an experimental configuration.

Introduction

Of the several millimeter sources that are in various stages of development, the virtual cathode oscillator (Vircator) has a combination of characteristics which recommend it for high frequency use. First, the frequency of the vircator is tunable by changing the magnitude of an imposed axial magnetic field, eliminating any requirement to change the physical structure of the device. A single vircator will be tunable over an order of magnitude in frequency (e.g., 10 GHz - 100 GHz). Second, the bandwidth of the generator can be narrow or broad based on magnetic field shaping and the use of beam collimators described below. Third, because the vircator functions above the space-charge limiting current for the electron beam, given efficient operation, it should be capable of much higher power than other microwave sources. Finally, the lack of passive resonating structures to produce the transmitted wave reduces the problem of field emission. This also increases the maximum possible generator power.

Experimentally, the virtual cathode has already proven itself to be a copious microwave source [1-7]. With the exception of the Tomsk experiment [4] the frequency spectra have all had a broad bandwidth and relatively low efficiency. Nevertheless, even at low efficiency the experiment at Harry Diamond Laboratories [5] using a foilless diode (1 MV, 30 kA) produced gigawatts of power in the Ku band. It is one of the most powerful centimeter wavelength microwave sources available. It will be shown later that the foilless diode in a shaped axial magnetic field represents the best configuration for a high frequency device.

Microwave Generation

Although only scaling relations are presently available, qualitative dependencies of virtual cathode parameters on beam kinetic energy and injected current are known [8,9]. First, potential amplitude, position, and oscillation frequency all have the same functional dependence on injected beam current. These parameters asymptotically approach a limiting value for current above the space-charge limit. Second, the fundamental oscillation frequency is approximately the relativistic beam plasma frequency given by

$$\omega_p^{rel} = \left(\frac{4\pi n_b^0 e^2}{\gamma_0 m}\right)^{1/2} \qquad (1)$$

where n_b^0 is the electron beam number density at injection γ_0 is the beam relativistic factor, e is the electron charge and m is its mass. In particular, the oscillation frequency from one-dimensional electrostatic and two-dimensional electromagnetic numerical simulations varies such that

$$\omega_p^{rel} \leq \omega_{osc} \leq \sqrt{2\pi}\, \omega_p^{rel} . \qquad (2)$$

The value of $\sqrt{2\pi}$ is an empirical result which has not yet been derived theoretically. The value of ω_{osc} increases with current monotonically. If the injection current exceeds the space-charge limiting current by a factor of three or greater, ω_{osc} is close to the maximum value. Eq. (1) in conjunction with the Child-Langmuir law describing space-charge limited diode emission explains the experimental linear dependence of frequency on the square root of diode voltage in foil diodes and reflex triodes. This analysis also

shows that the freuqency is inversely proportional to the anode-cathode (A-K) gap spacing d.

The virtual cathode oscillates stably at a set frequency in both time and space. This fluctuating potential barrier acts as a gate to reflect some electrons and transmit others. The motion of the gate bunches charge. In two dimensions the charge bunch and virtual cathode are separated spatially.
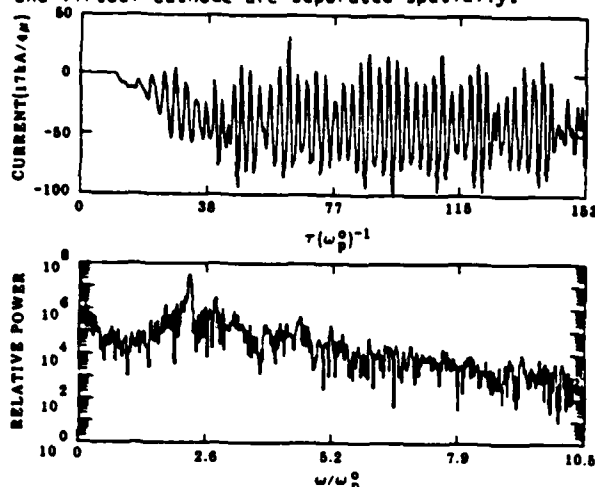

Figure 1. Net current amplitude and spectrum for a probe placed between the anode and virtual cathode. $\gamma_0 = 3.5$, $v_0 = 3.4\ v_\ell$.

By analogy this configuration represents an LC oscillator. The virtual cathode acts as a capacitor to store the beam kinetic energy. During that portion of the limit cycle in which the potential is greater than the injected beam energy, charge is constrained to remain near the anode. This starves the virtual cathode so that its amplitude decreases below $(\gamma_0 -1)\ mc^2/e$. Once this occurs the charge bunch is transmitted. The electron motion represents a large time varying current through an inductor. The presence of charge away from the anode reestablishes the virtual cathode, and the cycle repeats. The effect on beam current can be examined using simulations. A net current diagnostic is given in Fig. 1 where the probe is positioned between the anode and virtual cathode. The injected current in units of mc^3/e, v_0, is 3.4 times the limiting current, v_ℓ, and γ_0 is 3.5. Note that the virtual cathode can actually reverse the direction of current. The average current value is v_ℓ.

The oscillating current generates microwaves [10,11]. The wave frequency is the oscillation frequency of the virtual cathode. The wave propagates down the drift tube in a TM waveguide mode, which determines the wavelength and phase velocity of the wave in the guide. The field configuration is evident in simulations where there is no axial magnetic field. If a cold beam is injected and azimuthal symmetry is assumed by the code, the only nonzero fields are E_z, E_r, and B_θ in cylindrical geometry. These three fields define a TM wave traveling in the z direction.

The largest impediment to constructing an efficient vircator is the effect which heating has on the microwave generation efficiency. As noted earlier [12], beam temperature significantly damps out the amplitude of the potential oscillation. This can be understood in the following way. For a monoenergetic beam all of the charged particles bunch at the same location. Mathematically this represents a singularity where the charge density goes to infinity. In reality the charge bunch is not infinitely dense, but it does become several times greater than the initial beam injection density. The severity of the charge bunching leads to efficient microwave generation. If, on the other hand, the beam has a spread in axial momentum, the electrons will stop at different locations in the potential well. This tends to limit the charge bunching and the amplitude of the oscillating electric and magnetic fields. The effect of beam temperature in reducing the RF efficiency of the vircator has been witnessed in one-dimensional electromagnetic simulations [13]. A beam spread of less than 3% in energy reduces the microwave generation efficiency from 20% to approximately 2%. Under these conditions the vircator is nothing more than a Barkhausen oscillator [14]. Indeed, the low efficiency and broad bandwidth observed in most of the experiments to date can probably be attributed to the effects of electron reflexing in the diode region resulting in beam heating.

Vircator Design

Based on our current theoretical knowledge of the virtual cathode, numerical simulations, and experimental results, the following points must be considered in the design of a coherent, high frequency vircator. First, generation of high microwave frequencies requires large beam densities. Extremely high beam densities $(n_b^0 > 10^{14}\ cm^{-3})$ have been obtained from a foilless diode. The beam plasma frequency scales linearly with the electron cyclotron frequency due to the imposed axial magnetic field [15]. This is of significance, because it implies that a single vircator can be tuned over an order of magnitude in frequency (e.g., 10-100 GHz) simply by changing the axial magnetic field strength without changing the physical structure of the device.

Second, both the oscillation frequency and net current asymptotically approach a value as injected current is increased above the space-charge limit. Thus, using a very large value of v_0/v_ℓ does not substantially increase frequency or RF efficiency where efficiency is given by

$$n \leq \frac{e\Delta\phi}{(\gamma_0 - 1)\ mc^2} \ . \qquad (3)$$

A foilless diode in a strong axial magnetic field produces a very thin annular beam. Since v_ℓ for an annular beam is larger than for a solid beam of the same area, the value of v_0/v_ℓ will be smaller for the same beam current.

In order to assure narrow bandwidth, high efficiency microwave generation at high or low frequency from the vircator, the following characteristics must be met. First, no reflexing of electrons in the region between the anode and real cathode should occur. Any axial magnetic field must be shaped to divert the electrons, or flux excluders must be employed to confine the magnetic field to the diode region. The latter arrangement will allow the radial space-charge electric field to perform the role of expelling electrons to the waveguide wall. In addition, if the beam is annular, a collimator may be used to help prevent reflexing of electrons back to the cathode. Second, the electron beam must be cold. Experimental [16] and theoretical [15] results indicate that foilless diodes create low emittance beams. Laminar flow, where the electron Larmor orbit is smaller than the beam thickness, is obtained when [16]

$$\omega_c > (\gamma_0 - 1)^{1/2} \frac{c}{\sqrt{a\delta/2}} \qquad (4)$$

where a is the orbit radius, δ is the radial spacing between the cathode and drift tube wall (which acts as the anode) and ω_c is the electron cyclotron frequency given by eB_z/mc. Low beam scatter is also assured, because of the lack of a foil. Finally, the diode voltage and injected current must be constant. More appropriately stated, the impedance must be constant. Flat-top voltage pulses can be attained in a variety of ways in several diode configurations. However, at high voltages the foilless diode operates as a purely resistive load, therefore, $\omega_{osc} = \sqrt{I/V} = 1/\sqrt{Z}$ is constant. Also, absence of diode closure in some foilless diode experiments makes a long pulse device possible.

It is evident from this discussion that the foilless diode in a strong axial magnetic field represents the optimal configuration for a high frequency

vircator. It optimizes microwave power and efficiency while generating high frequency, coherent radiation. For low frequency operation a foil diode or reflex triode utilizing a high transparency mesh for the anode is the optimal design. No axial magnetic field should be employed in this case in order to minimize electron reflexing.

Conclusion

In summary, the vircator has the potential for producing very high power microwave pulses in the centimeter and millimeter wavelength regimes. In a foilless diode configuration it is tunable by adjusting the imposed axial magnetic field. In a foil diode or reflex triode tuning is accomplished by changing the A-K gap spacing. The microwave generation will be coherent and efficient, if electron reflexing into the diode region is prevented.

For an injected current $v_0 > 3\ v_\ell$, the frequency is approximately

$$f = 10.2\sqrt{j(kA/cm^2)/\beta\gamma_0}\ GHz \qquad (5)$$

where β is v/c. Because the oscillating beam is equivalent to a deformable dipole, the preferred waveguide mode for an axisymmetric beam in a straight-walled cylindrical guide is TM_{0n} where $n = D/\lambda_0$. D is the waveguide diameter and λ_0 is the free space wavelength. Thus, D/λ_0 should be chosen to be close to an integer value, in order to be near cutoff for that waveguide mode. This maximizes coupling to the nonresonant waveguide, because E_z/B_θ which is equal to the wave phase velocity is substantially larger than c. Once n is known, the phase velocity, group velocity, wavelength and impedance of the wave in the guide are determined. Similar considerations hold for a rectangular waveguide. Note that both v_ℓ and the cutoff wavelength, λ_c, depend on the guide dimensions and geometry. Both must be considered in choosing an experimental configuration.

Acknowledgment

<div align="center">References</div>

1. R. A. Mahaffey, P. Sprangle, J. Golden and C. A. Kapetanakos, Phys. Rev. Lett. **39**, 843 (1977).

2. H. E. Brandt, A. Bromborsky, H. B. Bruns, and R. A. Kehs, in Proc. of the 2nd Intl. Top. Conf. on High Power Electron and Ion Beam Research and Technology, (Cornell University, Ithaca, New York, 1977), p. 649.

3. J. M. Buzzi, H. J. Doucet, B. Etlicher, P. Haldenwang, A. Huetz, H. Lamain, C. Rouille, J. Cable, J. Delvaux, J. C. Jouys and C. Peugnet, idem, p. 663.

4. A. N. Didenko, G. P. Fomenko, I. Z. Gleizer, Ya. E. Krasik, G. V. Melnikov, S. F. Perelygin, Yu. G. Shtein, A. S. Sulakshin, V. I. Tsvetkov, and A. G. Zerlitsin, in Proc. of the 3rd Intl. Top. Conf. on High Power Electron and Ion Beam Research and Technology, (Institute of Nuclear Physics, Novosibirsk, USSR, 1979), p. 683.

5. A. Bromborsky, H. Brandt, and R. A. Kehs, Bull. Am. Phys. Soc. **26**, 165 (1981); and private communication.

6. M. C. Clark, private communication.

7. C. A. Ekdahl, private communication.

8. D. J. Sullivan and E. A. Coutsias in High Power Beams '81, Proceedings of the 4th Intl. Top. Conf. on High Power Electron and Ion Beam Research and Technology, edited by H. J. Doucet and J. M. Buzzi (Ecole Polytechnique, Palasieau, France, 1981), p. 371.

9. E. A. Coutsias and D. J. Sullivan, Phys. Rev. A **27**, 1535 (1983).

10. D. J. Sullivan, Bull. Am. Phys. Soc. **25**, 948 (1980).

11. D. J. Sullivan, in Proc. of the 3rd Intl. Top. Conf. on High Power Electron and Ion Beam Research and Technology, (Institute of Nuclear Physics, Novosibirsk, USSR, 1979), p. 769.

12. W. B. Bridges and C. K. Birdsall, J. Appl. Phys. **34**, 2946 (1963).

13. M. A. Mostrom, T. J. T. Kwan and C. M. Snell, Bull. Am. Phys. Soc. **27**, 1075 (1982).

14. H. Barkhausen and K. Kurz, Phys. Zeit. **21**, 1 (1920).

15. M. E. Jones and L. E. Thode, J. Appl. Phys. **51**, 5212 (1980).

16. R. B. Miller, K. R. Prestwich, J. W. Poukey, and S. L. Shope, J. Appl. Phys. **51**, 3506 (1980).

EFFECTS OF THERMAL SPREAD ON THE SPACE CHARGE LIMIT
OF AN ELECTRON BEAM
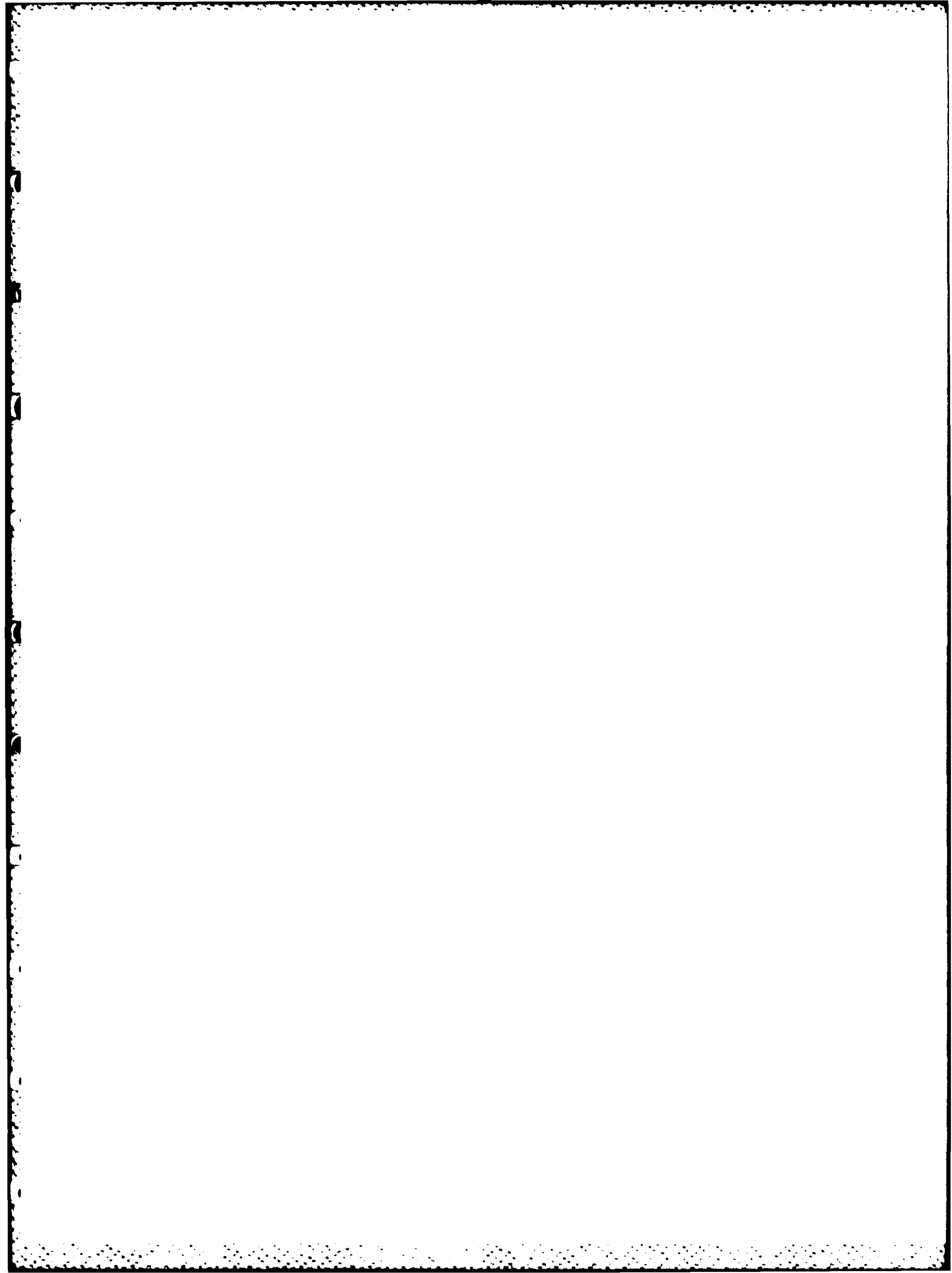
Effects of thermal spread on the space charge limit of an electron beam

By E. A. COUTSIAS

Department of Mathematics, University of New Mexico,
Albuquerque, NM 87131

An asymptotic analysis is carried out to calculate the effects of a small thermal spread in the injection energy of an electron beam on its space charge limit. It is found that the space charge limit is lowered proportionally to the beam temperature T near $T = 0$.

1. Introduction

Recent applications of intense charged particle beams in such areas as inertial confinement fusion and microwave generation (Coutsias & Sullivan 1983, and references therein) has necessitated a deepening of our understanding of the basic physics of space charge limited flows. An excellent review of our present state of knowledge can be found in Miller (1982).

In particular, many authors have carried out calculations of the space charge limit (SCL) of electron and ion beams (Voronin, Zozulya & Lebedev 1972; Read & Nation 1975; Genoni & Proctor 1980). These are concerned mostly with mono-energetic beams in various geometries. Although the importance of thermal effects is recognized, no analytical estimates of the effect of thermal spread on the beam kinetic energy at injection have appeared.

Here we present an asymptotic method to estimate the modification of the SCL due to a small thermal spread. For simplicity we limit our discussion to one-dimensional, classical motion. However, the method can be applied to any of the other situations for which SCL estimates exist and produce appropriate corrections.

2. Effect of temperature on the space charge limit

An adequate discussion of the properties of a non-relativistic electron beam in one dimension can be found in Coutsias & Sullivan (1983). Here we shall treat the beam as a one-dimensional electron gas flowing between two conducting grid planes, at fixed potential. For the density range we consider ($\simeq 10^{13}$ cm^{-3}) the usual collisionless approximation is valid, and thus the electron distribution function satisfies the Vlasov equation

$$\partial_t f + u\, \partial_x f + (e/m)\, E\, \partial_u f = 0 \tag{1}$$

where t, x, u are the time, position and velocity variables, respectively, and E is the self-consistent electric field.

The electron charge density is given by

$$n = \int_u f(x, u, t) \, du, \qquad (2)$$

and the electric field is found from

$$\partial_x E = (1/\epsilon_0) n, \qquad (3)$$

while the potential $\phi(x, t)$ is given by

$$\partial_x \phi = -E. \qquad (4)$$

The boundary conditions are given for the potential

$$\phi(0, t) = \phi_0 > 0, \quad \phi(l, t) = 0, \qquad (5)$$

and the distribution function

$$\left. \begin{array}{ll} f(0, u, t) \quad \text{specified for} \quad u > 0 \quad \text{(incoming flow at } x = 0\text{)} \\ f(l, u, t) = 0 \qquad \text{for} \quad u < 0 \quad \text{(no incoming flow at } x = l\text{)} \end{array} \right\} \qquad (6)$$

This specification is valid also in the presence of multiple streams.

We shall model the effect of finite source temperature by specifying the incoming distribution $f(0, u, t)$, $u > 0$ as

$$f(0, u, t) = n_0 \left(\frac{m}{2\pi kT} \right)^{\frac{1}{2}} \exp\left(\frac{m(u - V)^2}{2kT} \right), \qquad (7)$$

where T, assumed to be small, plays the role of an effective beam temperature.

For small enough T, we shall assume that we have a regime of steady behaviour, in analogy to the cold beam case. For steady states, particle energy is conserved and the solution to (1) is of the form (Davidson 1974)

$$f(x, u, t) = n_0 \left(\frac{m}{2\pi kT} \right)^{\frac{1}{2}} \exp\left(-\frac{m[V - (u^2 + (2e/m)(\phi(x) - \phi_0))^{\frac{1}{2}}]^2}{2kT} \right). \qquad (8)$$

Then, combining (2), (3), (4) and (8) we find that the potential satisfies the equation

$$\phi_{xx} + \frac{n_0}{\epsilon_0} \left(\frac{m}{2\pi kT} \right)^{\frac{1}{2}} \int_{u_m}^{\infty} \exp\left(-\frac{m[V - (u^2 + (2e/m)(\phi(x) - \phi_0))^{\frac{1}{2}}]^2}{2kT} \right) du = 0, \qquad (9)$$

where u_m, the velocity cut-off, is equal to

$$u_m(x) = \pm [(2e/m)(\phi_m - \phi(x))]^{\frac{1}{2}}. \qquad (10)$$

Here ϕ_m is the potential minimum, the $(+)$ sign applies to the right and the $(-)$ to the left of the position $x = \xi$ of the potential minimum as shown in Appendix A. We define

$$I(\phi; T) = \int_{u_m}^{\infty} \exp\left(-\frac{m[V - (u^2 + (2e/m)(\phi(x) - \phi_0))^{\frac{1}{2}}]^2}{2kT} \right) du. \qquad (11)$$

So (9) can be written as

$$\phi_{xx} + \frac{n_0 e}{\epsilon_0} \left(\frac{m}{2\pi kT} \right)^{\frac{1}{2}} I(\phi; T) = 0. \qquad (12)$$

By introducing the variable

$$s = (u^2 + (2e/m)(\phi(x) - \phi_0))^{\frac{1}{2}} - V \qquad (13)$$

the integral $I(\phi; T)$ in (12) can be rewritten as

$$I(\phi; T) = \int_{u=|u_m|}^{\infty} \exp\left(-\frac{ms^2}{2kT}\right) du + 2H(\xi - x) \int_{u=0}^{|u_m|} \exp\left(-\frac{ms^2}{2kT}\right) du. \qquad (14)$$

The first of the integrals in (14) represents the transmitted flow, while the second is due to particles without sufficient energy to cross the potential minimum and which are therefore reflected and return to the anode. Equation (12) with the integral term given by (14) is very hard to solve for a finite temperature T, but for small T we can approximate the integrals in (14) by Laplace's method. As is well known (Erdelyi 1956), in approximating integrals of this type with a strong maximum at an interior point, the dominant contribution comes from the neighbourhood of this point. Thus, in (14) we can approximate $I(\phi; T)$ by

$$I(\phi; T) \simeq \int_{-\infty}^{\infty} \exp\left(-\frac{ms^2}{2kT}\right) du + O\left(\exp\left(-\frac{ms_m^2}{2kT}\right)\right) \qquad (14a)$$

where $-s_m = V - ((2e/m)(\phi_m - \phi_0))^{\frac{1}{2}}$. Then provided V is large enough so that the mean energy of the beam is never of order $O(kT)$, the correction term goes to zero faster than any power of T as $T \to 0$, and therefore is negligible to the order that we carry the calculations. Nevertheless, it gives us an estimate of the domain of validity of the subsequent discussion, for which we need

$$\exp(-ms_m^2/2kT) \ll kT. \qquad (14b)$$

Therefore we write

$$I(\phi; \epsilon) \simeq \int_{-\infty}^{\infty} \exp\left(-\frac{ms^2}{2kT}\right) du = \int_{-\infty}^{\infty} \frac{(s+V)\exp(-ms^2/2kT)}{((s+V)^2 - (2\epsilon/m)(\phi(x) - \phi_0))^{\frac{1}{2}}} ds, \qquad (15)$$

and we get for the potential the approximate equation

$$\phi_{xx} + \frac{n_0}{\epsilon_0}\left(\frac{m}{2\pi kT}\right)^{\frac{1}{2}} \int_{-\infty}^{\infty} -\frac{(s+V)\exp(-ms^2/2kT)}{((s+V)^2 - (2\epsilon/m)(\phi(x) - \phi_0))^{\frac{1}{2}}} ds = 0. \qquad (16)$$

This can be integrated once to give

$$\tfrac{1}{2}\phi_x^2 + J(\phi; T) = J(\phi_m; T) \qquad (17)$$

where

$$J(\phi; T) = -\frac{n_0 m}{\epsilon_0 e}\left(\frac{m}{2\pi kT}\right)^{\frac{1}{2}} \int_{-\infty}^{\infty} (s+V)$$
$$\times \left((s+V)^2 - \left(\frac{2e}{m}\right)(\phi(x) - \phi_0)\right)^{\frac{1}{2}} \exp(-ms^2/2kT) ds. \qquad (18)$$

Integrating once more we find

$$x = \xi \pm 2^{-\frac{1}{2}} \int_{\phi_m}^{\phi} \frac{d\phi}{(J(\phi_m; T) - J(\phi; T))^{\frac{1}{2}}} \equiv \xi \pm S(\phi_m, \phi; T). \qquad (19)$$

Imposing the boundary conditions at $x = 0$ and $x = l$ we are led to the two equations determining ξ and ϕ_m:

$$0 = \xi - S(\phi_m, \phi_0; T), \quad l = \xi + S(\phi_m, 0; T). \qquad (20)$$

Eliminating ξ we find

$$l = S(\phi_m, \phi_0; T) + S(\phi_m, 0; T) \tag{21}$$

which must be analysed in order to determine, among other things, the desired steady state for the potential ϕ (and hence the distribution function f) and the SCL for small temperature $T > 0$.

To get an approximate expression for ϕ_m as $T \to 0$ we note that $J(\phi; T)$ can be approximated by Laplace's method if we expand the non-exponential part of the integrand in a Taylor series about $s = 0$ and integrate term by term. We find, after some algebra that

$$\left(-\frac{\epsilon_0 \epsilon}{n_0 m}\right) J(\phi; T) \simeq VR(\phi) + \frac{\epsilon V}{2}\left(\frac{R^2(\phi) - (e/m)(\phi - \phi_0)}{R^3}\right) + O(\epsilon^2) \tag{22}$$

where $\epsilon = (2kT/m) \ll 1$ and $R(\phi) = (V^2 - (2e/m)(\phi(x) - \phi_0))^{\frac{1}{2}}$. Using (22) we now approximate S:

$$S(\phi_m, \phi; T) = 2^{-\frac{1}{2}} \int_{\phi_m}^{\phi} \frac{d\phi}{(J(\phi_m; T) - J(\phi; T))^{\frac{1}{2}}} \simeq \left(\frac{\epsilon_0 e}{2n_0 m V}\right)^{\frac{1}{2}}$$

$$\times \int_{\phi_m}^{\phi} \frac{d\phi}{(R - R_m)^{\frac{1}{2}}}\left(1 - \frac{\epsilon}{4}\left(\frac{(r^2 - \Phi)R_m^3 - (R_m^2 - \Phi_m)R^3}{R^3 R_m^3 (R - R_m)}\right) + O(\epsilon^2)\right) \tag{23}$$

where we set $R = R(\phi)$, $R_m = R(\phi_m)$, $\Phi = (e/m)(\phi(x) - \phi_0)$, $\Phi_m = (e/m)(\phi_m - \phi_0)$ and since $d\phi = -(m/e)R\,dR$.

$$S(\phi_m, \phi; T) \simeq \left(\frac{2\epsilon_0 m}{9e n_0 V}\right)^{\frac{1}{2}} (R(\phi) - R(\phi_m))^{\frac{1}{2}}(R(\phi) + 2R(\phi_m)) \quad + \epsilon\left(\frac{\epsilon_0 m}{2e n_0 V}\right)^{\frac{1}{2}}$$

$$\times \left((R - R_m)^{\frac{1}{2}}\left(\frac{3}{4R_m} - \frac{V^2}{4R_m^3} - \frac{V^2}{8RR_m^3}\right) - \frac{3V^2}{8R_m^{\frac{3}{2}}}\sec^{-1}\frac{R^{\frac{1}{2}}}{R_m^{\frac{1}{2}}}\right) + O(\epsilon^2). \tag{24}$$

This can be substituted in (21) to find ϕ_m which in turn will allow us to determine ξ, the position of the potential minimum from (20) and, finally, we can combine all this information in (19) to get the desired relation between x and ϕ.

For simplicity we demonstrate this for the unbiased case, $\phi_0 = 0$. Letting

$$R(0) = R(\phi_0) = V, \quad s = R_m/V, \quad \hat{\epsilon} = \epsilon/V^2,$$

and introducing

$$a = 9e n_0 l^2 / 8\epsilon_0 m V^2,$$

(21) becomes

$$a^{\frac{1}{2}} \simeq (1 - s)^{\frac{1}{2}}\left((1 + 2s) + \tfrac{3}{2}\hat{\epsilon}\left(\frac{3}{4s} - \frac{1}{4s^2} - \frac{1}{8s^2} - \frac{3\sec^{-1}s^{-\frac{1}{2}}}{8s^{\frac{3}{2}}(1-s)^{\frac{1}{2}}}\right) + O(\hat{\epsilon}^2)\right). \tag{25}$$

We note that to leading order ($\epsilon = 0$), (24) reduces to the usual expression for cold beams. By including the $O(\hat{\epsilon})$ corrections we can find the first-order correction to the SCL. This is the value of a for which (24) has a double root. We find

$$a = a_0 + \hat{\epsilon}a_1 + \dots, \quad s = s_0 + \hat{\epsilon}s_1 + \dots,$$

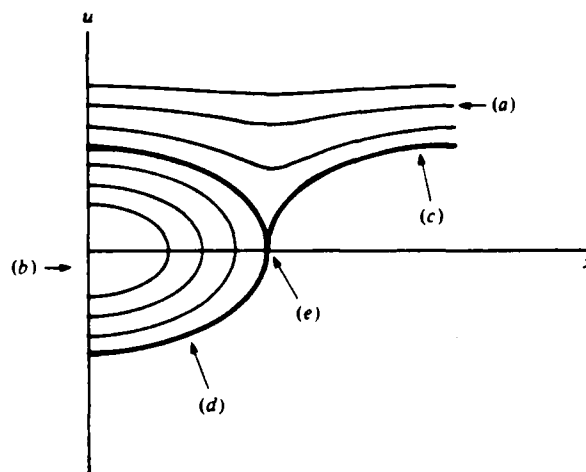and substitution yields

$$a_0 = 2, \quad s_0 = \tfrac{1}{2}.$$

FIGURE 1. Phase plane. (a) Transmitted particles, (b) reflected particles, (c) $u_m = ((2e/m)$ $(\phi_m - \phi(x)))^{\frac{1}{2}}$, (d) $u_m = -((2e/m)(\phi_m - \phi(x)))^{\frac{1}{2}}$, (e) ξ, location of potential minimum, $\phi(\xi) = \phi_m$.

from which we find a_1:

$$a_1 = -3(1 + \tfrac{3}{4}\pi) = -10\cdot07.$$

That is, the SCL is given by

$$\frac{e n_0 l^2}{\epsilon_0 m V^2} = \tfrac{16}{9} - (\tfrac{8}{3} + 2\pi)\left(\frac{2kT}{mV^2}\right) + O(T^2)$$

so that, for $T \ll 1$, the SCL is decreased in proportion to the temperature.

Appendix A

From the steady-state momentum equation

$$uu_x = (e/m)E \tag{A 1}$$

we find by integration that

$$\tfrac{1}{2}u^2 + \frac{e}{m}\rho(x) = \text{constant}. \tag{A 2}$$

At $x = 0$, $u = u_0$, $\rho = \rho_0$ and

$$\tfrac{1}{2}u^2 + \frac{e}{m}\rho(x) = \tfrac{1}{2}u_0^2 + \frac{e}{m}\rho_0. \tag{A 3}$$

Since (1) is a statement of the conservation of f along particle trajectories, we find that if u and u_0 are related by (A 3) then

$$f(x, u, t) = f(0, u_0, t) \tag{A 4}$$

and expression (8) follows.

A complication arises when we are dealing with reflected particles since u in

E. A. Coutsias

(A 3) can have either sign. Assuming that the potential achieves a unique minimum $\rho = \rho_m$ at some location $x = \xi$, we find that particles that arrive at ξ with zero velocity must start at $x = 0$ with velocity $u_m(0)$ such that

$$\tfrac{1}{2}u_m^2(0) + \frac{e}{m}\rho_0 = \tfrac{1}{2}u_m^2(x) + \frac{e}{m}\rho(x) = \frac{e}{m}\rho_m.$$

At each point $x < \xi$ particles with velocities less than u_m will be reflected before reaching $x = \xi$ while faster particles will be transmitted across the potential barrier. To the left of the potential minimum therefore, we shall have particles with velocities larger than $((2e/m)(\rho_m - \rho(x)))^{\frac{1}{2}}$ composing the flow that will be transmitted, and particles with velocities in the range

$$|u| < ((2e/m)(\rho_m - \rho(x)))^{\frac{1}{2}}$$

composing the counterstreaming flow (figure 1). To the right of the potential minimum we have only particles with velocities larger than u_m, so that the potential minimum has filtered out of the flow particles whose energies were too small to traverse it.

REFERENCES

DAVIDSON, R. C. 1974 *Theory of Non-neutral Plasmas.* Benjamin.

COUTSIAS, E. A. & SULLIVAN, D. J. 1983 *Phys. Rev. A*, **27**, 1535.

ERDELYI, A. 1956 *Asymptotic Expansions.* Dover.

GENONI, T. C. & PROCTOR, W. A. 1980 *J. Plasma Phys.* **23**, 129.

MILLER, R. B. 1982 *An Introduction to the Physics of Intense Charged Particle Beams.* Plenum.

READ, M. E. & NATION, J. A. 1975 *J. Plasma Phys.* **13**, 127.

VORONIN, V. S., ZOZULYA, YU. T. & LEBEDEV, A. N. 1972 *Soviet Phys. Tech. Phys.* **17**, 432.

END

FILMED

2-85

DTIC